P516914.PDF [Page: 3 of 96]

DEFENCE R&D DÉFENSE

A Calibration Procedure for an HFSWR Receive Array

Eric K.L. Hung

Defence R&D Canada
TECHNICAL REPORT
DREO TR 2001-103
December 2001

National Defence / Défense nationale

Canada

REPRODUCTION QUALITY NOTICE

This document is the best quality available. The copy furnished to DRDCIM contained pages that may have the following quality problems:

: Pages smaller or Larger than normal

: Pages with background colour or light coloured printing

: Pages with small type or poor printing; and or

: Pages with continuous tone material or colour photographs

Due to various output media available these conditions may or may not cause poor legibility in the hardcopy output you receive.

☒ If this block is checked, the copy furnished to DRDCIM contained pages with colour printing, that when reproduced in Black and White, may change detail of the original copy.

P516914.PDF [Page: 5 of 96]

Copy No:_____

A calibration procedure for an HFSWR receive array

Eric K.L. Hung
Surface Radar Section
Defence Research Establishment Ottawa

Defence Research Establishment Ottawa

Technical Report
DREO TR 2001-103
December 2001

© Her Majesty the Queen as represented by the Minister of National Defence, 2001

© Sa majesté la reine, représentée par le ministre de la Défense nationale, 2001

Abstract

This report contains a description and performance evaluation of the matrix calibration method developed by the author in 1995 for the receive antenna array in the high frequency surface wave radar (HFSWR) at Cape Race, Newfoundland. The evaluation compares this method with two other methods: (a) the phase-only calibration method being used and (b) an assumed gain-and-phase method that equalizes the complex element output amplitudes of signals in the boresight direction.

The results showed that the matrix calibration method had the most accurate direction estimates, the narrowest spectral peaks, the best resolution of closely space targets, and the lowest signal-to-interference-plus-noise ratio (SINR) threshold for target detection. The phase-only and gain-and-phase methods had false target tracks and direction-dependent biases in direction estimates. The phase-only method also had a line splitting problem.

Based on the difference in SINR thresholds for target detection, the matrix calibration method could increase the present maximum nighttime target detection range of the HFSWR by more than 50% in situations where the interference is highly directional and extremely strong.

Résumé

Ce rapport contient une description et une évaluation de performance de la méthode de calibration de matrice développée par l'auteur en 1995 pour le réseau d'antenne de réception du radar décamétriques à ondes de surface (RDOS) installée à Cap Race, Terre Neuve. La méthode de calibration de matrice est comparée avec deux autres méthodes : (a) la méthode de calibration par phase seule présentement utilisée dans le RDOS et (b) une méthode de phase et gain qui égalise l'élément complexe des sorties d'amplitude des signaux dans la direction de l'axe d'antenne de pointage.

Les résultats démontrent que la méthode de calibration de matrice produit les mesures de direction les plus précises, les crêtes spectrales les plus étroites, la meilleure résolution de cibles rapprochées, et le seuil de détection le plus bas de pour le rapport signal au brouillage (SINR). La méthode de phase et celle de phase et gain produisent des fausses traces de cibles et des erreurs systématiques dans les mesures de direction dépendant de la direction de la cible. La méthode de phase a aussi des problèmes de division des lignes spectrales.

D'après la différence dans le seuil de détection pour le SINR, la méthode de calibration de matrice peut augmenter la portée maximum de détection de nuit du RDOS par plus de 50% pour des situations où le brouillage est très directionnel et extrêmement fort.

This page is left blank

This page is left blank

Executive summary

The Defence Research Establishment Ottawa (DREO) and Raytheon Canada Limited have jointly built a high frequency surface wave radar (HFSWR) at Cape Race, Newfoundland, for coastal surveillance on a 24-hours/7-days basis. This radar is located behind a cliff facing the Atlantic Ocean and is designed to detect and track targets, e.g., surface ships and low-flying aircraft, below the microwave radar horizon. It can work in isolation or as part of a larger surveillance system that incorporates other sensors such as satellites, line-of-sight radars, and other HFSWRs.

The HFSWR has been operational since summer 1998. A problem that has not yet been solved is the detection of long-range targets at night, when extremely strong skywave interference signals are present. These signals originate from distance sources. They can reach the HFSWR, because the signal-absorbing D layer of the ionosphere is absent at night. During daylight hours, this radar has no difficulties detecting large ships at ranges up to 450 km from the radar. At night, the maximum range drops dramatically to less than 200 km. Many attempts to increase this range had been made. None could extend the maximum range beyond 200 km.

The skywave interference was one of several problems identified in 1994 when a prototype HFSWR was operating at Cape Race. A matrix calibration method for the receive antenna array of the radar was developed in 1995 by this author to mitigate their detrimental effects. This method effectively uses sixteen sets of complex calibration coefficients at once to compensate for the unequal gain and phase responses at the array elements, mismatches in cables and electronics between the elements and the receivers, small errors in element locations, mutual coupling among the elements, imperfect ground screens, irregular shoreline, signal diffraction at the cliff, and interaction between the array and other local objects. The reasoning was that detection of targets outside the interference direction was still possible, if the array was accurately calibrated to reduce the leakage of interference power outside the interference direction.

This report presents a description and a performance evaluation of the matrix calibration method, using a set of calibration data collected in April 2000. The evaluation compares the matrix method with two other methods: (a) the single-set phase-only calibration method being used and (b) an assumed single-set gain-and-phase method that equalizes the complex element output amplitudes of signals in the boresight direction. Some notable observations on targets within 55° of the boresight direction are listed below.

(a) The leakage of signal power outside the source direction were 0.04% and 1.29% in data sections with high and low signal-to-interference-plus-noise ratios (SINRs), respectively, in calculations with the matrix calibration method. They were between 5.20 and 11.7% in the single-set phase-only method, and between 0.21 and 5.73% in the single-set gain-and-phase method.

(b) The errors in source direction estimates were usually the smallest in the matrix method and the largest in the phase-only method.

(c) The errors in source direction estimates had a component linearly dependent on the source azimuth in the phase-only and gain-and-phase methods.

(d) The signal peaks in the directional spectra of the array snapshots were the narrowest in calculations with the matrix method. They were significantly broader in the phase-only method. Those in the gain-and-phase method were just as narrow as the peaks in the matrix method for signals in the boresight direction. They increased to about half the widths of the phase-only method as the source moved towards the ±50° directions.

(e) The power levels of false peaks were less than -40 dB of the true signal in the matrix method. They were above -30 dB and frequently over -20 dB in the phase-only method. Those in the gain-and-phase method are usually between -30 and -20 dB.

(f) The false peaks did not form false target tracks in the matrix method. They frequently formed false tracks in the phase-only and gain-and phase methods.

(h) Line splitting (two direction estimates separated by less than one beamwidth in high-resolution direction-finding, one signal source actually present) was very common in calculations with the phase-only method.

(i) The SINR threshold in detecting targets outside the region of extremely strong interference was the lowest in the matrix method. It was approximately 17 dB higher in the phase-only method and 5 to 8 dB higher in the gain-and-phase method.

Based on the approximate 17 dB difference in SINR threshold for target detection, the matrix calibration method could increase the present maximum nighttime target detection range of the HFSWR by more than 50% in situations where the interference is highly directional and extremely strong.

Hung, EKL. 2001. "A calibration procedure for an HFSWR receive array". DREO TR 2001-103. Defence Research Establishment Ottawa.

Sommaire

Le Centre de Recherche de la Défense d'Ottawa et Raytheon Canada Limited ont construit conjointement un radar décimétrique à onde de surface (RDOS) à Cap Race, Terre Neuve. Ce radar a été construit pour la surveillance côtière 24 heures par jour et 7 jours par semaine. Le RDOS est située sur une falaise en face de l'océan Atlantique et est conçu pour la détection et la poursuite des cibles se déplaçant en dessous de l'horizon radar microonde tel que des navires et des avions volant à basse altitude. Le RDOS peut opérer seule ou être intégrer dans un système de surveillance plus grand qui incorpore d'autres récepteurs tel que les satellites, les radars de lignes visuelles, et d'autres RDOS.

Le RDOS a été opérationnel depuis l'été 1998. La détection des cibles à longue portée durant la nuit, quand le brouillage ionosphérique est intense, est un problème qui n'a pas été résolu juste qu'à maintenant. Ce brouillage ionosphérique provient de sources distantes. Ces signaux lointains de brouillages peuvent atteindre le RDOS durant la nuit car la couche ionosphérique D qui absorbe les signaux décamétrique est absente durant la nuit. Durant le jour, le RDOS n'a pas de difficulté a détecter de grands navires jusqu'à 450km de portée. Durant la nuit, la portée maximum diminue dramatiquement à seulement 200km. Plusieurs essais ont été faits pour augmenter cette portée, mais aucun n'a été capable de l'augmenter au-delà de 200km.

Le brouillage ionosphérique est un des problèmes identifiés en 1994 quand un prototype de RDOS opérait à Cap Race. Une méthode de calibration de matrice pour l'antenne réceptrice du radar a été développée en 1995 par l'auteur pour réduire leurs effets négatifs. Cette méthode utilise 16 ensemble de coefficients de calibration complexe pour compenser le gain et les réponses inégal des éléments du réseau d'antenne, le facteur d'inégalité des câbles et de l'électronique entre les éléments, les petites erreurs dans la position des éléments, le couplage mutuelle entre les éléments, les imperfections de l'écran de terre, l'irrégularité de la ligne de rivage, la diffraction du signal sur la falaise, et l'interaction entre le réseau et les objets locales. Le raisonnement est que la détection des cibles a l'extérieur du brouillage est encore possible, si le réseau est précisément calibrer pour réduire la puissance de brouillage à l'extérieur de la direction de brouillage.

Ce rapport contient une description et une évaluation de performance de la méthode de calibration de matrice utilisant un ensemble de calibration collecter en avril 2000. La méthode de calibration de matrice est comparée avec deux autres méthodes : (a) la méthode de calibration par phase seule présentement utilisée dans le RDOS et (b) une méthode de phase et gain qui égalise l'élément complexe des sorties d'amplitude des signaux dans la direction de l'axe d'antenne de pointage. Quelques observations notables sur les cibles situées à moins de 55 degrés de l'axe de pointage de l'antenne sont listées ci dessous.

(a) La puissance du signal à l'extérieur de la direction de la source était de 0.04% et 1.29% dans la section des données ayant des rapports de signal à brouillage (SINR) faible et fort, respectivement, dans les calculs utilisant la méthode de calibration de

matrice. Elles étaient entre 5.2 et 11.7% dans la méthode de phase seul, et entre 0.21 et 5.73 dans la méthode de calibration de gain et phase.

(b) Les erreurs dans les mesures de direction étaient habituellement les plus petites avec la méthode de calibration de matrice et étaient les plus grandes dans la méthode de phase seule.

(c) Les erreurs dans les mesures de la direction de la source ont une composante linéaire qui dépend de l'azimut pour les méthodes de calibration de phase seule et aussi de phase et gain.

(d) Les crêtes des signaux dans le spectre directionnelles des données instantanées sont les plus étroites quand on utilise la méthode de calibration de matrice. Les crêtes sont beaucoup plus larges quand on utilise la méthode de calibration de phase seule. Les crêtes obtenues avec la méthode de phase et gain sont aussi étroites que celles obtenues avec la méthode de calibration de matrice. Cependant les crêtes élargissent jusqu'à la moitié de la largeur de celles obtenues avec la méthode de calibration de phase seule lorsque la source se déplace loin de l'axe de 'antenne vers 55 degrés.

(e) Les niveaux de puissance sont moins que -40dB comparée au signal réel avec la méthode de calibration de matrice. Ils sont au-dessus de –30dB et souvent au-dessus de –20db dans la méthode de calibration de phase seule. Ceux de la méthode de calibration de gain et phase sont habituellement entre –30 et –20dB.

(f) Les fausses crêtes n'ont pas produit de fausses traces de poursuite avec la méthode de matrice. Cependant, ils ont souvent formée des fausses traces de poursuite avec la méthode de phase seul et aussi la méthode de calibration de phase et gain.

(g) La division des lignes spectrales (deux mesures de directions séparées par moins que une largeur de faisceau d'antenne dans la radiogoniométrie haute résolution, un signal source actuellement présent) sont très commun avec la méthode de calibration de phase seule.

(h) Le seuil de SINR pour la détection de cibles à l'extérieur de la région de brouillage ionosphérique intense est le plus bas avec la méthode de calibration de matrice. Il est approximativement 17dB plus grand avec la méthode de phase seule et de 5dB a 8dB avec la méthode de phase et gain.

D'après la différence de 17dB dans le seuil de détection pour le SINR, la méthode de calibration de matrice peut augmenter la portée maximum de détection de nuit du RDOS par plus de 50% pour des situations où le brouillage est très directionnel et extrêmement fort.

Hung, EKL. 2001. "A calibration procedure for an HFSWR receive array". DREO TR 2001-103. Defence Research Establishment Ottawa.

Table of contents

Abstract i

Executive summary iii

Sommaire v

Table of contents vii

List of figures ix

List of tables xii

Acknowledgements xiii

1. Introduction 1

2. Calibration method 3
   - 2.1 Signal model 3
   - 2.2 Conditions 4
   - 2.3 Calculation of calibration matrix 5

3. Experiment and calibration matrix 7
   - 3.1 Experiment 7
   - 3.2 Data preprocessing 8
   - 3.3 Calibration matrix 10
   - 3.4 Effective calibration coefficients 11

4. Performance evaluation 20
   - 4.1 Leakage power outside signal direction 20
   - 4.2 Errors in direction estimates 22
   - 4.3 Directional power spectra of calibration data 22
   - 4.4 Direction estimates calculated with calibration data 23
   - 4.5 Target resolution 24
   - 4.6 Target detection in presence of strong interference 25
   - DFT results 26

P516914.PDF [Page: 14 of 96]

5. Conclusion 65

6. References 66

Appendix A. Calculation of signal powers and direction estimates 68

Appendix B. Calculation of Capon directional spectra 70

P516914.PDF [Page: 15 of 96]

List of figures

Figure 1: Site map of the high frequency surface wave radar at Cape Race. 15

Figure 2: A set of sixteen 64-point FFT power spectra calculated with the outputs of the array elements in one preaveraged pulse measured with source azimuth direction close to 0.0°.16

Figure 3: A 256-point Doppler power spectrum calculated with the bandpass filtered outputs of Element 8. The data were measured with source azimuth direction close to 0.0°..... 17

Figure 4: A 256-point Doppler power spectrum calculated with the 0 kHz complex amplitudes in the 64-point FFT spectra. 18

Figures 5a and 5b: Average power at array elements in the 256 preaveraged pulses used to produce one preprocessed snapshot (Figure 5a, top) and average power at array elements in the preprocessed snapshots (Figure 5b, bottom). 19

Figure 6: Leakage power calculated with **C** (black), phase-only matrix $\mathbf{C}_P$ (red), and gain-and-phase matrix $\mathbf{C}_{GP}$ (blue). 29

Figures 7a, 7b and 7c: Errors in source direction estimates from snapshots with $-75° \le \theta_m \le 55°$, using calibration matrices **C** (Figure 7a, top), $\mathbf{C}_P$ (Figure 7b, middle), and $\mathbf{C}_{GP}$ (Figure 7c, bottom). 30

Figure 8a: Directional spectra of array snapshots in preprocessed calibration data file. Matrix **C** was used to calibrate the snapshots. 31

Figures 8b: Directional spectra of array snapshots in preprocessed calibration data file. Phase-only $\mathbf{C}_P$ was used to calibrate the snapshots. 32

Figure 8c: Directional spectra of array snapshots in preprocessed calibration data file. Gain-and-phase matrix $\mathbf{C}_{GP}$ was used to calibrate the snapshots. 33

Figure 9a: Directional spectra of six array snapshots with source azimuth $\theta_m \approx 40°$. Matrix **C** was used to calibrate the snapshots. 34

Figure 9b: Directional spectra of six array snapshots with source azimuth $\theta_m \approx 40°$. Phase-only matrix $\mathbf{C}_P$ was used to calibrate the snapshots. 35

Figure 9c: Directional spectra of six array snapshots with source azimuth $\theta_m \approx 40°$. Gain-and-phase matrix $\mathbf{C}_{GP}$ was used to calibrate the snapshots. 36

Figure 10a: Candidate direction estimates calculated with the preprocessed array snapshots. Matrix **C** was used to calibrate the snapshots. 37

Figure 10b: Candidate direction estimates calculated with the preprocessed array snapshots. Phase-only matrix $\mathbf{C}_P$ was used to calibrate the snapshots..... 38

Figure 10c: Candidate direction estimates calculated with the preprocessed array snapshots. Gain-and-phase matrix $\mathbf{C}_{GP}$ was used to calibrate the snapshots..... 39

Figure 11a: Directional spectra of two equal-strength intersecting targets. Matrix $\mathbf{C}$ was used to calibrate the snapshots. 40

Figure 11b: Directional spectra of two equal-strength intersecting targets. Phase-only matrix $\mathbf{C}_P$ was used to calibrate the snapshots. 41

Figure 11c: Directional spectra of two equal-strength intersecting targets. Gain-and-phase matrix $\mathbf{C}_{GP}$ was used to calibrate the snapshots..... 42

Figure 12a: Some directional spectra of synthetic snapshots with azimuth $\theta_m \approx -30°$. Matrix $\mathbf{C}$ was used to calibrate the snapshots. 43

Figure 12b: Some directional spectra of synthetic snapshots with azimuth $\theta_m \approx -30°$. Phase-only matrix $\mathbf{C}_P$ was used to calibrate the snapshots..... 44

Figure 12c: Some directional spectra of synthetic snapshots with azimuth $\theta_m \approx -30°$. Gain-and-phase matrix $\mathbf{C}_{GP}$ was used to calibrate the snapshots. 45

Figure 13a: Candidate direction estimates calculated with the synthetic snapshots used to produce Figure 11a. Matrix $\mathbf{C}$ was used to calibrate the snapshots..... 46

Figure 13b: Candidate direction estimates calculated with the synthetic snapshots used to produce Figure 11b. Phase-only matrix $\mathbf{C}_P$ was used to calibrate the snapshots..... 47

Figure 13c: Candidate direction estimates calculated with the synthetic snapshots used to produce Figure 11c. Gain-and-phase matrix $\mathbf{C}_{GP}$ was used to calibrate the snapshots..... 48

Figure 14a: Directional spectra of a target in strong interference. Matrix $\mathbf{C}$ was used to calibrate the snapshots. 49

Figure 14b: Directional spectra of a target in strong interference. Phase-only matrix $\mathbf{C}_P$ was used to calibrate the snapshots. 50

Figure 14c: Directional spectra of a target in strong interference. Gain-and-phase matrix $\mathbf{C}_{GP}$ was used to calibrate the snapshots. 51

Figure 15a: Some directional spectra of synthetic snapshots with SINR≈-40 dB. Matrix $\mathbf{C}$ was used to calibrate the snapshots. 52

Figure 15b: Some directional spectra of synthetic snapshots with SINR≈-23 dB. Phase-only matrix $\mathbf{C}_P$ was used to calibrate the snapshots..... 53

P516914.PDF [Page: 17 of 96]

Figure 15c: Some directional spectra of synthetic snapshots with SINR=-30 dB. Gain-and-phase matrix $\mathbf{C}_{GP}$ was used to calibrate the snapshots. 54

Figure 16a: Candidate direction estimates calculated with the synthetic snapshots used to produce Figure 14a. Matrix $\mathbf{C}$ was used to calibrate the snapshots. 55

Figure 16b: Candidate direction estimates calculated with the synthetic snapshots used to produce Figure 14b. Phase-only matrix $\mathbf{C}_P$ was used to calibrate the snapshots. 56

Figure 16c: Candidate direction estimates calculated with the synthetic snapshots used to produce Figure 14c. Gain-and-phase matrix $\mathbf{C}_{GP}$ was used to calibrate the snapshots. 57

Figure 17a: DFT directional spectra of array snapshots used to calculate the Capon spectra in Figure 14a. The snapshots have a target in strong interference. Matrix $\mathbf{C}$ was used to calibrate the snapshots. 58

Figure 17b: DFT directional spectra of array snapshots used to calculate the Capon spectra in Figure 14b. The snapshots have a target in strong interference. Phase-only matrix $\mathbf{C}_P$ was used to calibrate the snapshots. 59

Figure 17c: DFT directional spectra of array snapshots used to calculate the Capon spectra in Figure 14c. The snapshots have a target in strong interference. Gain-and-phase matrix $\mathbf{C}_{GP}$ was used to calibrate the snapshots. 60

Figure 18: DFT directional spectra calculated with a SINR=-50 dB snapshot and calibration matrices $\mathbf{C}$ (black), $\mathbf{C}_P$ (red) and $\mathbf{C}_{GP}$ (blue). 61

Figure 19a: DFT candidate direction estimates calculated with matrix $\mathbf{C}$ and the synthetic snapshots. 62

Figure 19b: DFT candidate direction estimates calculated with phase-only matrix $\mathbf{C}_P$ and the synthetic snapshots. 63

Figure 19c: DFT candidate direction estimates calculated with gain-and-phase matrix $\mathbf{C}_{GP}$ and the synthetic snapshots. 64

P516914.PDF [Page: 18 of 96]

List of tables

Table 1: Bias power and signal power in the range FFT spectra of array elements in a preaveraged pulse with source azimuth close to the 0.0 ° boresight direction. The source frequency was 3.225 MHz. 12

Table 2: Magnitudes of some coefficients $\{C_{pq}\}$ at the top left corner of calibration matrix **C**.13

Table 3: Magnitudes and phases of some calibration coefficients $\{\gamma_1, \gamma_2, ..., \gamma_N\}$. Columns identified with θ_m=0 ° and -60 ° were calculated with Eq. (17). Those identified with P are used in phase-only calibration. 14

P516914.PDF [Page: 19 of 96]

Acknowledgements

The development of a calibration method for the receive antenna array at Cape Race, Newfoundland, was an assignment given me by Dr. Tim Coyne.

1. Introduction

The Defence Research Establishment Ottawa (DREO) and Raytheon Canada Limited have jointly developed a high frequency surface wave radar (HFSWR) at Cape Race, Newfoundland, for coastal surveillance on a 24-hours/7-days basis. This radar is located behind a cliff facing the Atlantic Ocean. It has a uniform, linear receive array with sixteen monopole doublets spaced at a distance of 33.33 meters. The radar is designed to detect and track targets, e.g., surface ships and low-flying aircraft, below the microwave radar horizon. It can work in isolation or as part of a larger surveillance system that incorporates other sensors, including satellites, line-of-sight radars, and other HFSWRs.

Detection of long-range targets at night requires detection of weak target reflectors in the presence of strong skywave interference. The signals in this interference originate from distant sources. They can travel thousands of kilometres to reach the HFSWR at night, because the signal-absorbing D layer of the ionosphere is only present during the day. To separate the target from interference, it is necessary to use high-resolution direction-finding methods such as the Capon minimum variance method [1-3] and the least squares autoregressive method (LSAR) [4,5], or interference suppression methods such as the sample matrix inverse method [6,7] and the adaptive sidelobe cancellation method [8], or both. These methods require accurately calibrated antenna arrays [9-14].

The skywave interference, together with a few others, was identified by Dr. Tim Coyne, in 1994. He concluded that a proper calibration of the receive antenna array was essential to mitigate their detrimental effects. The reasoning was that detection of targets outside the interference direction is still possible, if the interference is highly directional and if the array is accurately calibrated to reduce the leakage of interference power outside the interference direction. A matrix calibration method for the HFSWR was developed by this author in 1995. It effectively used sixteen sets of complex coefficients at once to compensate for the unequal gain and phase responses at the array elements, mismatches in cables and electronics between the elements and the receivers, small errors in element locations, mutual coupling among the elements, imperfect ground screens, irregular shoreline, signal diffraction at the cliff, and interaction between the array and other local objects. Because the HFSWR was not operational at the time, the method was evaluated with data from four other sources. All results indicated significant improvements in target detection after calibration [15-18].

The HFSWR at Cape Race has been fully operational since summer 1998. However, it is still being calibrated with a single-set phase-only method that only addresses the unequal phase responses at the array elements. During daylight hours, this radar has no difficulties detecting large ships up to 450 km from the radar. At night, the maximum range drops dramatically to less than 200 km. Many attempts to increase this range had been made. All used the phase-only calibration method. In agreement with what Dr. Coyne had concluded, none could extend the maximum range beyond 200 km.

This report presents a description and a performance evaluation of the matrix calibration method, using a set of calibration data collected in April 2000. The evaluation compares the matrix method with two other methods: (a) the single-set phase-only calibration method being used and (b) an assumed single-set gain-and-phase method that equalizes the complex element output amplitudes of signals in the boresight direction. In the results, the matrix calibration method has the most accurate direction estimates, the narrowest spectral peaks, the best resolution of closely space targets, and the lowest signal-to-interference-plus-noise ratio (SINR) threshold for target detection; the phase-only and gain-and-phase methods show false target tracks and direction-dependent biases in direction estimates; and the phase-only method also has a line splitting problem.

Based on the difference in SINR thresholds for target detection, the matrix calibration method could increase the present maximum nighttime target detection range of the HFSWR by more than 50% in situations where the interference is highly directional and extremely strong.

In the following, Section 2 describes the matrix calibration method developed in 1995. Section 3 discusses the calibration data and the calibration matrix. Section 4 presents the results of performance evaluations and Section 5 contains the conclusions. There are two appendices. Appendix A describes the computation of signal direction estimates with the LSAR method and Appendix B describes the computation of directional spectra with the Capon method.

2. Calibration method

A brief description of the calibration method developed in 1995 is presented here. It includes the signal model used, the conditions that must be satisfied and the computation of the calibration matrix.

2.1 Signal model

The receive antenna array has N elements. A pilot source is present and the source azimuth direction is θ_m. An ideal snapshot of the outputs of the array elements is given by

$$\mathbf{x}_m = \alpha_m \mathbf{a}_m , \tag{1}$$

where α_m is the complex signal amplitude and $\mathbf{a}_m$ is the array steering vector for the source direction. This expression assumes a perfectly calibrated array, a pure tone signal, no interaction among the array elements, no noise, and no interference. In the convention used, angle θ_m is measured clockwise from the array boresight direction.

The corresponding measured array snapshot is given by $\mathbf{y}_m$, with

$$\mathbf{y}_m = \mathbf{B}\mathbf{x}_m + \mathbf{e}_m . \tag{2}$$

Matrix **B** is N×N. It depends on the gain and phase responses at the array elements, mismatches in cables and electronics between the elements and the receivers, small errors in element locations, mutual coupling among the elements, imperfect ground screens, irregular shoreline, signal diffraction at the cliff, and interaction between the array and other local objects. Vector $\mathbf{e}_m$ denotes the sum of interference and noise.

Let $\{\mathbf{y}_1,\mathbf{y}_2,...,\mathbf{y}_M\}$ be a set of M array snapshots measured with source directions $\{\theta_1,\theta_2,...,\theta_M\}$, respectively. The calibration matrix calculated with this set is identified here as the N×N matrix **C** that, together with the estimates of $\{\mathbf{x}_1,\mathbf{x}_2,...,\mathbf{x}_M\}$, minimises the objective function

$$S = \frac{\sum_{m=1}^{M} \| \mathbf{C}\mathbf{y}_m - \hat{\mathbf{x}}_m \|^2}{\sum_{m=1}^{M} \| \mathbf{C}\mathbf{y}_m \|^2} , \tag{3}$$

subject to the uniqueness condition

$$C_{11} = 1.0 . \tag{4}$$

Vector $\hat{\mathbf{x}}_m$ is an estimate of $\mathbf{x}_m$ and will be calculated as the projection of $\mathbf{C}\mathbf{y}_m$ on $\mathbf{a}_m$. The $\hat{}$ denotes the estimate and C_{pq} denotes the pq-th coefficient of $\mathbf{C}$.

In later discussions, the superscripts ^{T} and ^{H} denote the transpose and conjugate-transpose, respectively; the set $\{y_{1m}, y_{2m}, \ldots, y_{Nm}\}$, for example, denotes the N components of $\mathbf{y}_m$; and $\mathbf{y}^c_m$ defined as

$$\mathbf{y}^c_m = \mathbf{C}\mathbf{y}_m \,, \tag{5}$$

denotes the calibrated snapshot calculated with $\mathbf{y}_m$.

It may be noted that $\mathbf{C}$ has the singular value decomposition

$$\mathbf{C} = \mathbf{U}\Sigma\mathbf{V}^H \,, \tag{6}$$

where $\mathbf{U}=(\mathbf{u}_1,\mathbf{u}_2,\ldots,\mathbf{u}_N)$ and $\mathbf{V}=(\mathbf{v}_1,\mathbf{v}_2,\ldots,\mathbf{v}_N)$ are matrices with orthonormal column vectors, and Σ is a diagonal matrix with singular values $\{\sigma^2_1,\sigma^2_2,\ldots,\sigma^2_N\}$. Substitution into (5) gives,

$$\mathbf{y}^c_m = \sum_{n=1}^{N} \sigma^2_n (\mathbf{v}^H_n \mathbf{y}_m)\mathbf{u}_n \,. \tag{7}$$

This expression shows that $\mathbf{C}$ effectively calculates the projection of $\mathbf{y}_m$ on each $\mathbf{v}_n$, i.e., the projection $(\mathbf{v}^H_n\mathbf{y}_m)\mathbf{v}_n$, and then replaces this projection by $(\mathbf{v}^H_n\mathbf{y}_m)\mathbf{u}_n$. Therefore, using Eq. (5) to calculate $\mathbf{y}^c_m$ is equivalent to using N sets of calibration coefficients at once to calibrate the array snapshot $\mathbf{y}_m$. Each set has N complex amplitudes.

The computation of $\mathbf{C}$ is a pure mathematical procedure. The function S depends on the signal amplitude estimates $\hat{\alpha}_1$ to $\hat{\alpha}_M$ through $\hat{\mathbf{x}}_1$ to $\hat{\mathbf{x}}_M$, respectively. In the special case of zero noise and interference, the $\mathbf{e}_m$ in each $\mathbf{y}_m$ is a null vector, $\mathbf{CB}=\beta\mathbf{I}_N$, $\mathbf{C}\mathbf{y}_m=\hat{\mathbf{x}}_m$, $\hat{\mathbf{x}}_m=\beta\mathbf{x}_m$, and $S=0$. The β is a complex scalar and $\mathbf{I}_N$ is an N×N identify matrix.

2.2 Conditions

The following conditions are assumed to be satisfied.

1. The array elements are narrowband;
2. The process that converts an ideal snapshot to a measured snapshot can be approximated by a matrix;
3. The calibration data are generated by moving a pilot source over the range of azimuth directions covered by the HFSWR;
4. The number of array snapshots in the calibration data is sufficiently large; and
5. A preliminary calibration has been carried out, so that one can obtain rough estimates of the complex signal amplitudes from the array snapshots.

Conditions 3 and 4 are needed for tolerance to unknown interference, including diffuse and specula multipath. Together, they attempt to destroy the correlation between the

pilot signal and any interference present in the environment by effectively randomising their phase difference in the data. They also cause each fixed-direction interference source to behave like spatially distributed interference by forcing the angular separation between it and the pilot signal to spread over a wide range of values. The number of snapshots required in Condition 4 is the number required for $\mathbf{C}$ to reach the asymptotic limit as this number increases.

2.3 Calculation of calibration matrix

The calculation of $\mathbf{C}$ is based on the following observations.

A. If $\mathbf{C}_{i-1}$ is an estimate of $\mathbf{C}$ and

$$\mathbf{z}_m = \mathbf{C}_{i-1}\mathbf{y}_m , \tag{8}$$

a least square estimate of the signal amplitude is

$$\hat{\alpha}_m = \frac{\mathbf{a}_m^H \mathbf{z}_m}{|\mathbf{a}_m|^2} , \tag{9}$$

and an estimate of $\mathbf{x}_m$ is

$$\hat{\mathbf{x}}_m = \hat{\alpha}_m \mathbf{a}_m . \tag{10}$$

B. Given the N×M matrices $\hat{\mathbf{X}}$ and $\mathbf{Y}$, where $\hat{\mathbf{X}}=(\hat{\mathbf{x}}_1,\hat{\mathbf{x}}_2,\ldots,\hat{\mathbf{x}}_M)$ and $\mathbf{Y}=(\mathbf{y}_1,\mathbf{y}_2,\ldots,\mathbf{y}_M)$, one can get a new estimate of $\mathbf{C}$ by solving the equation

$$\mathbf{C}_i\mathbf{Y} = \hat{\mathbf{X}} \tag{11}$$

as

$$\mathbf{C}_i = (\hat{\mathbf{X}}\hat{\mathbf{X}}^H)(\mathbf{Y}\hat{\mathbf{X}}^H)^{-1} , \tag{12}$$

and imposing the uniqueness condition (4) on $\mathbf{C}_i$. The inverse $(\mathbf{Y}\hat{\mathbf{X}}^H)^{-1}$ exists, because of Conditions 3 and 4.

C. Given snapshot $\mathbf{y}_m$ and the array steering vector $\mathbf{a}_m$ for source direction θ_m, the initialisation

$$\mathbf{C}_0 = \mathrm{diag}\{a_{m1}/y_{m1}, a_{m2}/y_{m2}, \ldots, a_{mN}/y_{mN}\} , \tag{13}$$

where diag{...} denotes a diagonal matrix, is equivalent to a crude calibration that equalises the element output gains and phases for signals with source direction θ_m. The set $\{a_{m1},a_{m2},\ldots,a_{mN}\}$ denotes the components of $\mathbf{a}_m$.

D. Let

$$\mathbf{D}_i = \mathbf{C}_i - \mathbf{C}_{i-1} \tag{14}$$

and

$$\Delta_i = \max\{|D_{pq}|: p,q=1,2,...,N\} . \tag{15}$$

One can terminate the iteration if (a) $\Delta_i<\varepsilon$, where ε is a small value, or (b) $i \geq i_{max}$, where i_{max} is the maximum number of iterations specified.

There are six steps in the procedure. The S_{i-1} in Step 3 is the value of S in the (i-1)th iteration.

Step 1.

(a) Specify ε.
(b) Specify i_{max}.
(c) Let i=1.
(d) Calculate $\mathbf{C}_0$ with Eq. (13) and the snapshot $\mathbf{y}_m$ with θ_m closest to 0°.

Step 2.

Calculate $\{\mathbf{z}_1,\mathbf{z}_2, ...,\mathbf{z}_M\}$ with Eq. (8).
Calculate $\{\hat{\mathbf{x}}_1,\hat{\mathbf{x}}_2, ...,\hat{\mathbf{x}}_M\}$ with Eqs. (9) and (10).

Step 3.

Calculate S_{i-1} with Eq. (3), $\{\hat{\mathbf{x}}_1,\hat{\mathbf{x}}_2, ...,\hat{\mathbf{x}}_M\}$, and $\{\mathbf{z}_1,\mathbf{z}_2,...,\mathbf{z}_M\}$.
Calculate $\mathbf{C}_i$ with Eq. (12).

Step 4.

Impose the uniqueness condition given by Eq. (4) on $\mathbf{C}_i$, i.e., the condition $(C_i)_{11}=1$.

Step 5.

Calculate Δ_i with Eqs. (14) and (15).

Step 6.

If $\Delta_i<\varepsilon$ or $i>i_{max}$,
  Terminate the iterations and identify $\mathbf{C}_i$ as $\mathbf{C}$.
Else,
  Replace i by i+1 and return to Step 2.

In Step 3, vector $\mathbf{z}_m$ is the product $\mathbf{C}_{i-1}\mathbf{y}_m$ needed to calculate S_{i-1}. The calculation of S_{i-1} can be omitted if the sole objective is to check if S_i converges. From Eq. (3), S_i converges if $\mathbf{C}_i$ converges.

3. Experiment and calibration matrix

This section discusses the calibration experiment, data preprocessing, the calibration matrix, and effective calibration coefficients for given source directions.

The calibration matrix calculated is only useful for calibrating array snapshots in which all signal and interference directions are more than one beamwidth from the ends of the azimuth range -80° to 58.7°, i.e., for signals and interference direction inside the range -54.0° to 42.7°.

3.1 Experiment

The receive antenna array in the HFSWR at Cape Race is located behind a 23 m high cliff facing the Atlantic Ocean. It has a uniform linear receive antenna array with sixteen monopole doublet elements, i.e., N=16, spaced at a distance of 33.33 m. Figure 1 is a map of the radar site. It shows the location of the antenna array, a hut that houses the radar receivers and other hardware, a lighthouse northeast of the array, and the shoreline near the lighthouse. The coastline is irregular. The land behind the cliff was boggy and had many streams and ponds.

A pilot source on board a 44 foot fishing boat was used to generated the calibration signals at the receive array. Originally, the boat was to sail from the θ=90° endfire direction of the antenna array to the θ=-90° endfire direction at a range of 28 km from the array. Due to poor weather conditions, a section of the track southwest of Cape Race was omitted and the boat actually sailed from θ=58.7° to θ=-90°.

The pilot source consisted of an ICOM IC-735 HF transceiver free running at 3.225 MHz and transmitting at a nominal power level of 50 watts. This transceiver was powered by an ICOM power supply, which in turn was powered by the boat's 110-volt generator. It fed a BIRD power coupler and meter, to provide a measure of the forward/reflected power, and then an antenna matching unit, model MFJ 901B, from MFJ Inc. The unit was connected to a 22 foot HF whip antenna mounted on the boat's rigging. The lower end of the whip was approximately 25 feet above the waterline and the grounds of all components were attached to the boat's internal ground system.

At the antenna site, the output of each array element was connected by cable to a receiver and heterodyned to 25 kHz. Quadrature sampled snapshots of the array element outputs were taken in sets, identified as pulses, of 64 snapshots per pulse and at a rate of 62.5 pulses per second. Groups of eight pulses were then summed to produce 7.8125 preaveraged pulses per second. The 64 snapshots in each pulse were sampled at 10 microsecond intervals, or 100 kHz.

Data collection started at approximately 10:00 Newfoundland standard time and ended at 16:00. There were instances when the boat was asked to "heave to" and standby in position, so that downloading of collected data could be carried out at the hut. A DGPS (differential global positioning system) provided the time and boat position. These values

were logged by training a video camera on the DGPS display. As a precaution, the values were also hand logged every 5 minutes.

3.2 Data preprocessing

The calibration data collected had 186077 preaveraged pulses with 64 array snapshots per pulse, 16 complex amplitudes per snapshot, and 8 bytes per complex amplitude. Preprocessing was necessary, because

(a) The pulses were unevenly spaced in source azimuth;
(b) Each receiver had a zero frequency bias amplitude that depended on the receiver;
(c) There were many strong interfering spikes in the data; and
(d) The file had over 1.5 gigabytes of data and had to be reduced to a manageable size.

The error amplitudes in (b) originated from a flaw in receiver design and the spikes in (c) were generated by an ionosonde that was programmed to turn on for several minutes just before every GMT hour. The ionosonde was turned off at the controls in the hut during the calibration experiment. Unknown to the operator, it was still sounding the ionosphere at hourly intervals.

The data preprocessing procedure was as follows.

Step 1. Bandpass filtering
The outputs of each element in each preaveraged pulse were transformed with a 64-point fast Fourier transform (FFT) to produce a range FFT spectrum with 64 complex amplitudes. The amplitude in the 25 kHz signal bin was extracted from each element to produce a bandpass filtered snapshot.

Step 2. Doppler filtering
The intermediate file constructed with the bandpass filtered snapshots was divided into overlapping groups with a window 256 snapshots wide. The window moved down the file in steps of 32 snapshots. Each group of 256 snapshots was then converted to a Doppler filtered snapshot with a 256-point FFT.

Step 3. Removal of snapshots with large errors in source direction estimates
The Doppler filtered snapshots were calibrated with the phase-only calibration coefficients and the source direction estimate $\hat{\theta}$ in each calibrated snapshot was then calculated with the LSAR method [4,5]. All snapshots with $|\hat{\theta}_m-\theta_m|>6°$ were deleted.

Step 4. Thinning
The snapshots at the output of Step 3 were selectively deleted to make the remaining snapshots approximately equally spaced in azimuth.

The preprocessed calibration data file was denoted by $\{y_1,y_2,...,y_M\}$. It had 3470 snapshots, i.e., M=3470, spaced approximately 0.032° apart in the range $-80.0°\le\theta_m\le58.70°$. For reasons to be given later, all snapshots with $\theta_m<-80.0°$ were deleted. The computation of source direction estimate is given in Appendix A.

Step 1 was designed to remove the zero frequency bias at the receiver outputs and to increase the SINR at the array elements. The 25 kHz signal bin was bin 17 in the 64-point FFT, because the array snapshots in each pulse were sampled at 100 kHz. In Step 2, the 256 complex bandpass filtered amplitudes of each element in the group were converted to a Doppler spectrum with a 256-point FFT. Next, the Doppler bin with the largest power in the spectrum of the first element was identified as the signal bin in the Doppler spectra of all elements. Then, the complex amplitude in this bin was extracted from the spectrum of each element and used to construct a Doppler filtered snapshot. Step 3 was designed to remove Doppler filtered snapshots with unusually low SINRs. Before this step, there were 265 snapshots with $\theta_m<-80.0°$. After this step, only 61 remained. Because over 75% were removed, the remaining snapshots had questionable reliabilities and were removed as well. No snapshots with $-75.0°\le\theta_m\le 58.70°$ were removed and very few with $-80.0°\le\theta_m\le-75.0°$ had $|\hat{\theta}_m-\theta_m|>6°$. Step 4 was necessary, because the array snapshots were very unevenly spaced in azimuth.

The reason for the large number of snapshots with $|\hat{\theta}_m-\theta_m|>6°$ for $\theta_m<-80.0°$ could be the large land mass northeast of the receive antenna array. It could also be strong mutual coupling among the array elements for these source directions. Indications of mutual coupling can be found in Figures 7b and 7c in the performance evaluation to be presented later.

Figure 2 shows a typical set of N, where N=16, 64-point FFT power spectra calculated with the outputs of the array elements in one preaveraged pulse. To avoid unnecessary complications from the ionosonde spikes, the nominal source azimuth direction was chosen to be near 0.0°, so that it was more than 6.0° from the nearest spike. There are two peaks in the spectrum of each element. The peak at 25 kHz is the signal peak and the one at 0 kHz peak is the bias at the receiver. Table 1 shows the bias and signal powers at the elements. These powers are between 1245 and 4102 units at the 25 kHz signal bins and between 0.17 and 19.76 units at the 0 kHz bin. The conversion factor from power units to signal field strengths at the array elements was unavailable.

Figure 3 shows a typical 256-point Doppler power spectrum calculated in Step 2 with the complex signal amplitudes in the 25 kHz signal bin of the 64-point FFT spectra in Step 1. In this example, the signal amplitudes were calculated with the outputs of Element 8 and the nominal source direction was also near 0.0°. The spectrum has a band with many peaks that are 15 dB or more above the noise background. The bandwidth is larger than 1.0 Hz. A study of the data showed that the shape of the band changed with time and that the band position drifted slowly in frequency. Figure 4 shows the 256-point Doppler power spectrum obtained when the complex bias amplitudes in the 0 kHz bin were used instead. It has a strong peak at 0.0 Hz.

The bandwidth of more than 1.0 Hz in Figure 3 was unexpectedly large, because a monotone source was specified for the experiment. The drift in band position was expected, because the pilot source on board the fishing boat was free running and, therefore, not synchronized with the oscillator in the receivers.

Figure 5a shows the average power at the array elements in the 256 preaveraged pulses used in Steps 1 and 2 to generate one preprocessed snapshot. There are strong spikes at θ_m=48.2°, 27.9°, 9.4°, -18.9° and -48.8°. From the records on time and boat position, these are interference spikes generated by the ionosonde, because they are one hour apart. The time of the

rightmost spike is GMT 13:59:46 (NST 10:29:46) and the time of the leftmost spike is GMT 17:59:46 (NST 14:29:46). The peaks are not equally space in direction, because the boat did not move at a constant angular speed along the track. Figure 5b shows the average power at the elements in the preprocessed snapshots. The preprocessing in Steps 1 and 2 had removed the spikes. It had also reduced the average power outside the spike regions by approximately 10 units.

3.3 Calibration matrix

The array snapshots in the preprocessed calibration data file were used to calculate **C**, using the procedure at the end of Section 2.3. In Step 1, the assignments were ε=0.00001 and i_{max}=50. In Step2, the array steering vector in Eq. (9) was calculated as

$$\mathbf{a}_m = (1, \exp[j2\pi d \sin\theta_m], \ldots, \exp[j2\pi d(N-1)\sin\theta_m])^T , \qquad (16)$$

where d=0.35552=(33.33/93.75) was the element spacing in wavelengths. In this expression, the first array element was the element farthest to the north. In Step 3, the matrix product $\mathbf{Y}\hat{\mathbf{X}}^H$ in Eq. (12) was highly illconditioned, because there were no snapshots with θ_m outside the range -80.00° to 58.70°. Consequently, the inverse $(\mathbf{Y}\hat{\mathbf{X}}^H)^{-1}$ was replaced by the Moore-Penrose pseudo-inverse calculated with the singular value decomposition method. Only the thirteen strongest eigenvectors were retained, because this number produced the best results in the evaluation of the calibration method. In the intermediate results, the Δ_i in Eq. (15) dropped quickly from 1.20016 at i=1 to 0.02197 at i=2. It then decreased gradually to 0.00056 at i=50. The corresponding value of S_{i-1} dropped from 0.95132 at i=1 to 0.00712 at i=2 and to 0.00677 at i=7. It then increased very slowly to 0.00689 at i=29 before decreasing again to 0.00682 at i=50. Table 2 shows the magnitudes of the coefficients $\{C_{pq}\}$ in the upper left 8×7 corner of **C**. Evidently, **C** was not symmetric and the magnitudes in the main diagonal were different. A check on the validity of Condition 4 in Section 2.2 could not be made, because the rank(**C**)=13<N.

Matrix **C** was effectively the asymptotic limit of $\mathbf{C}_i$ for extremely large i_{max}. This property was verified by calculating a second **C**, denoted by **C'**, using ε=0.00000 and i_{max}=200. Matrix **C'** looked identical to **C** when the first three decimal places of the matrix coefficients were compared. It also produced near identical results in calculations. Therefore, for all practical purposes, **C'** and **C** were the same and **C** had effectively converged to the asymptotic limit. A rigorous proof of convergence is beyond the scope of this report.

Matrix **C** was not unique. The **C**'s calculated with different $\mathbf{C}_0$'s were not expected to produce the same results from snapshots with source directions less than one beamwidth from the ends of the data azimuth range -80.00° to 58.70°. However, all were expected to produce essentially the same results if the directions were more than one beamwidth from the ends. These properties were verified by calculating a **C'** with a $\mathbf{C}_0$ derived from the phase-only calibration coefficients used to calibrate the HFSWR. In agreement with the above remarks, matrices **C'** and **C** looked different but produced near identical directional spectra from snapshots with θ_m more than one beamwidth from the ends. The $\mathbf{C}_0$ in the calculation of **C'** was the phase-only calibration matrix $\mathbf{C}_P$ in the performance evaluation in Section 4.

Matrix **C** was not unique, because $\mathbf{Y}\hat{\mathbf{X}}^H$ was highly illconditioned and the weak eigenvectors of $\mathbf{Y}\hat{\mathbf{X}}^H$ depended on $\mathbf{C}_0$ as well as the $\mathbf{y}_m$'s with θ_m's less than one beamwidth from the ends. These weak eigenvectors determined the performance of **C** for snapshots with source directions up to one beamwidth inside the data azimuth range or totally outside it. All **C**'s were expected to produce essentially the same results for source directions more than one beamwidth from the ends, because the calibration data determined the strong eigenvectors of $\mathbf{Y}\hat{\mathbf{X}}^H$. These eigenvectors in turn determined the performance of **C** for snapshots with these source directions.

Matrix **C** was only useful for calibrating array snapshots in which all signal and interference directions were more than one beamwidth from the ends of the azimuth range -80° to 58.7°. Because azimuth direction measured in beam widths from boresight was given by

$$\theta_B = Nd\sin\theta\,, \tag{17}$$

C was only useful for calibration array snapshots with $-54.0° < \theta_m < 42.7°$.

3.4 Effective calibration coefficients

The calibrated snapshot $\mathbf{y}^c_m$ and the uncalibrated snapshot $\mathbf{y}_m$ are related by Eq. (5), i.e., $\mathbf{y}^c_m = \mathbf{C}\mathbf{y}_m$. It follows from this relation that the effective calibration coefficients for the components of $\mathbf{y}_m$ are given by

$$\gamma_n = \frac{y^c_{nm}}{y_{nm}}\,, \qquad n=1,2,\ldots,N\,, \tag{18}$$

where $\{y^c_{1m}, y^c_{2m}, \ldots, y^c_{Nm}\}$ and $\{y_{1m}, y_{2m}, \ldots, y_{Nm}\}$ are the components of $\mathbf{y}^c_m$ and $\mathbf{y}_m$, respectively. These coefficients are used to multiply the outputs of the array elements. They depend on θ_m through $\mathbf{y}_m$. Table 3 contains the magnitudes and phases of effective calibration coefficients $\{\gamma_1, \gamma_2, \ldots, \gamma_N\}$ for $\theta_m = 0°$ and $\theta_m = -60°$. In the same table are the phase-only coefficients used to calibrate the HFSWR. For the sake of convenience in comparison, all three sets of coefficients have been normalised to give $\gamma_1 = 1.0$, so that $\text{abs}(\gamma_1) = 1$ and $\text{angle}(\gamma_1) = 0$. There are several notable observations. Firstly, the coefficients calculated with Eq. (18) are highly dependent on θ_m. In the special case of the eighth array element, i.e. $n=8$, for example, the magnitude is 0.74 for $\theta_m = 0°$ and 0.57 for $\theta_m = -60°$. Secondly, for a given θ_m, the magnitudes and phases of the coefficients depend on the array elements. Thirdly, the magnitudes and phases of the phase-only coefficients are different from those calculated with Eq. (18).

Element	Bias Power (0 kHz)	Signal Power (25 kHz)
1	2.17	1245
2	1.98	1257
3	0.98	2668
4	1.24	2668
5	0.17	2785
6	2.78	1942
7	5.55	3011
8	19.76	2469
9	0.63	4102
10	3.35	2503
11	1.04	3456
12	0.47	2985
13	3.80	2349
14	2.74	3010
15	4.48	1991
16	1.53	1487

Table 1: Bias power and signal power in the range FFT spectra of array elements in a preaveraged pulse with source azimuth close to the 0.0° boresight direction. The source frequency was 3 225 MHz

p	q=1	q=2	3	4	5	6	7
1	1.000	0.057	0.099	0.068	0.084	0.009	0.028
2	0.073	0.833	0.133	0.140	0.181	0.052	0.046
3	0.074	0.104	0.601	0.154	0.090	0.127	0.032
4	0.017	0.102	0.120	0.500	0.179	0.109	0.039
5	0.055	0.073	0.136	0.150	0.504	0.180	0.114
6	0.033	0.071	0.092	0.111	0.158	0.513	0.138
7	0.021	0.038	0.022	0.050	0.074	0.091	0.474
8	0.055	0.068	0.072	0.012	0.063	0.167	0.181

Table 2: Magnitudes of some coefficients (C_{pq}) at the top left corner of calibration matrix **C**

n	Magnitude			Phase		
	θ_m=0°	θ_m=-60°	P	θ_m=0°	θ_m=-60°	P
1	1.00	1.00	1.00	0	0	0
2	1.11	0.89	1.00	-161	-162	-146
3	0.86	0.49	1.00	44	41	52
4	0.71	0.51	1.00	-92	-114	-100
5	0.71	0.57	1.00	79	66	99
6	0.85	0.60	1.00	-63	-64	-48
7	0.66	0.42	1.00	134	131	151
8	0.74	0.57	1.00	-15	-30	-12
9	0.58	0.45	1.00	170	159	-162
10	0.72	0.51	1.00	-29	-35	-5
11	0.64	0.44	1.00	122	119	134
12	0.68	0.43	1.00	-99	-101	-91
13	0.71	0.50	1.00	100	90	107
14	0.68	0.46	1.00	-108	-114	-104
15	0.90	0.56	1.00	29	23	27
16	0.90	0.52	1.00	151	145	151

Table 3: Magnitudes and phases of some calibration coefficients $\{\gamma_1, \gamma_2, \ldots, \gamma_N\}$. Columns identified with θ_m=0° and -60° were calculated with Eq. (17). Those identified with P are used in phase-only calibration.

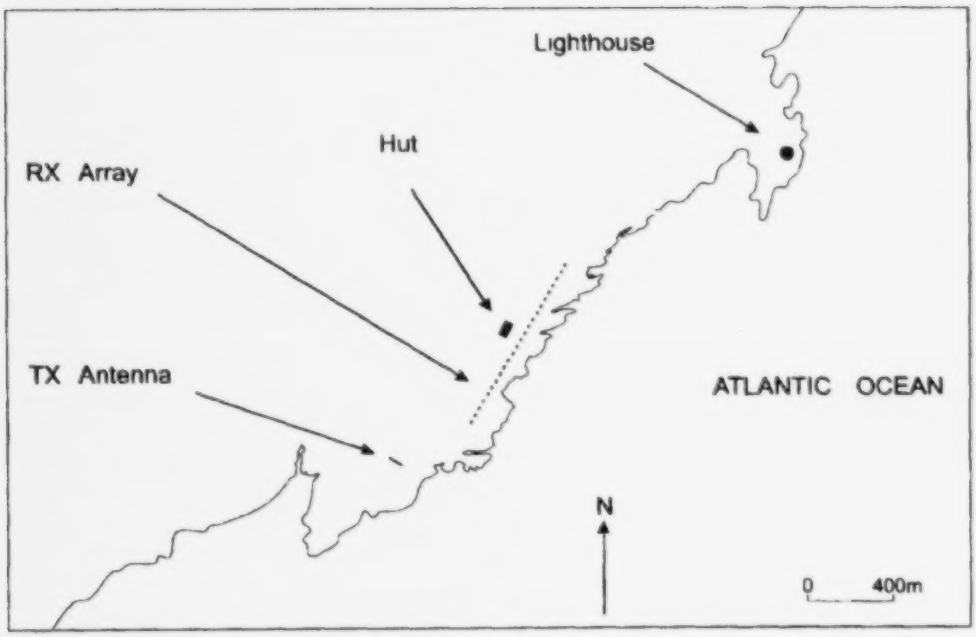

Figure 1: Site map of the high frequency surface wave radar at Cape Race

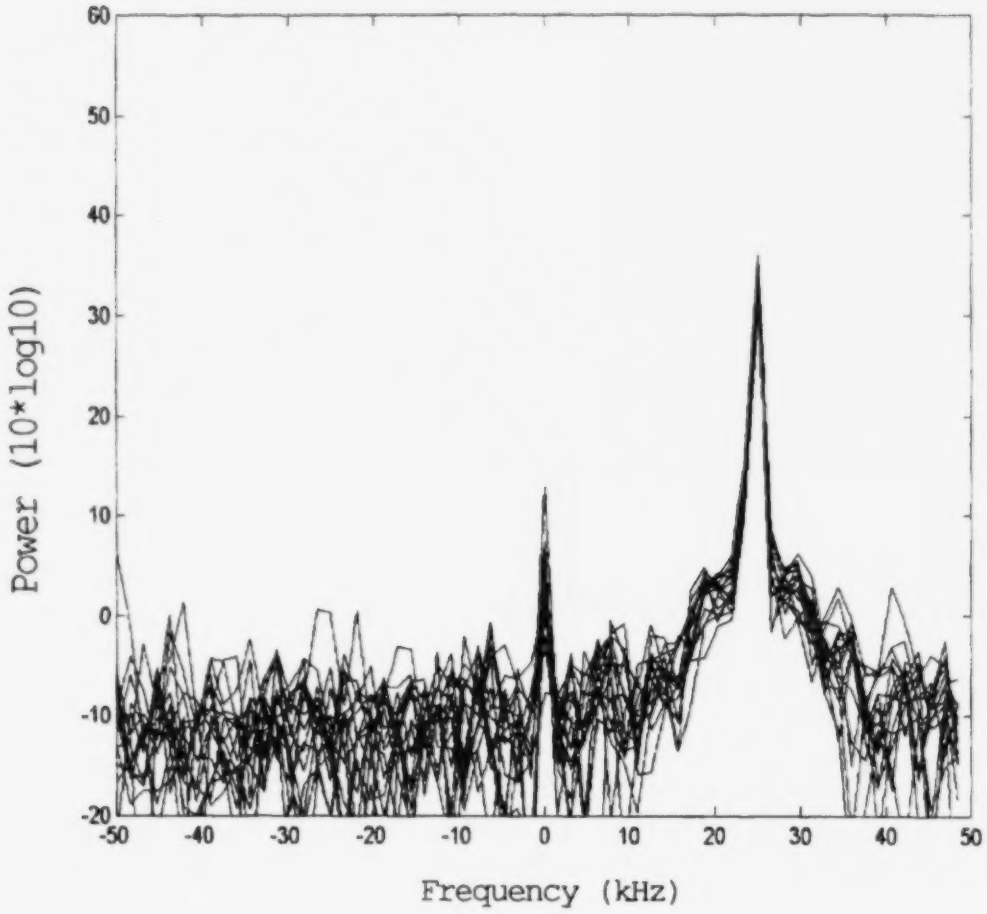

Figure 2: A set of sixteen 64-point FFT power spectra calculated with the outputs of the array elements in one preaveraged pulse measured with source azimuth direction close to 0.0°.

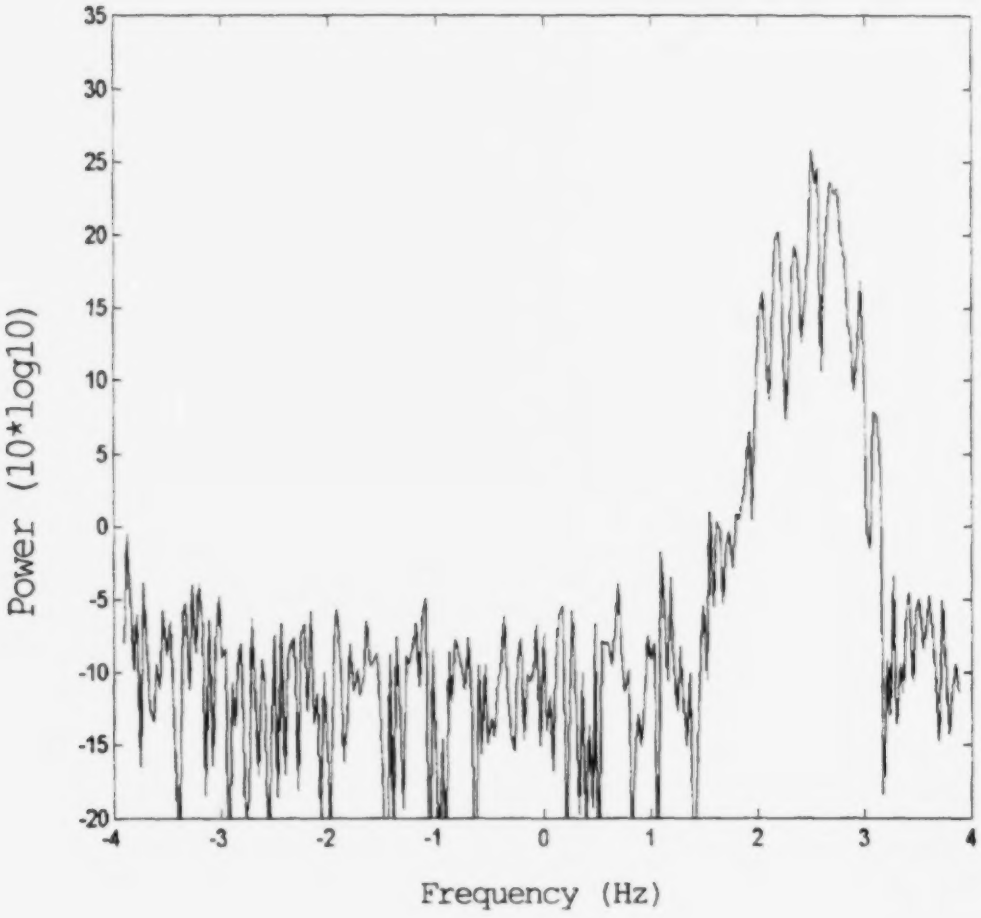

Figure 3: A 256-point Doppler power spectrum calculated with the bandpass filtered outputs of Element 8. The data were measured with source azimuth direction close to 0.0°.

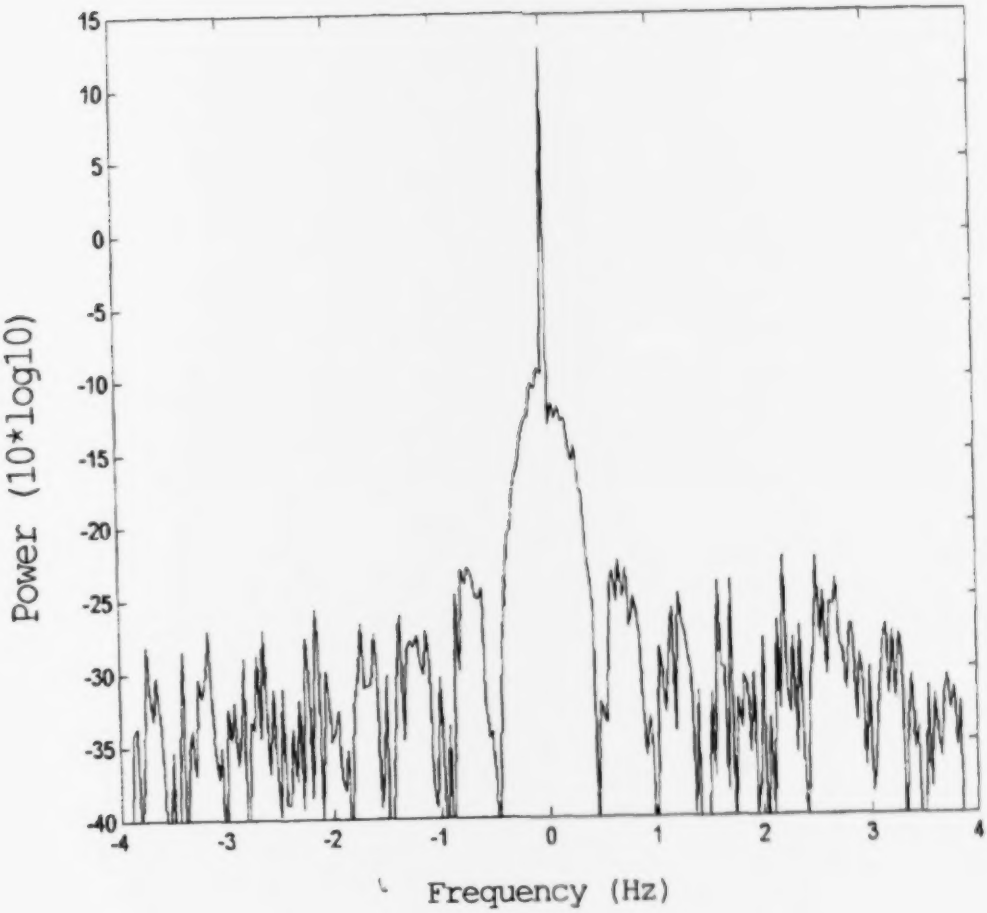

Figure 4: A 256-point Doppler power spectrum calculated with the 0 kHz complex amplitudes in the 64-point FFT spectra.

Figure 5a

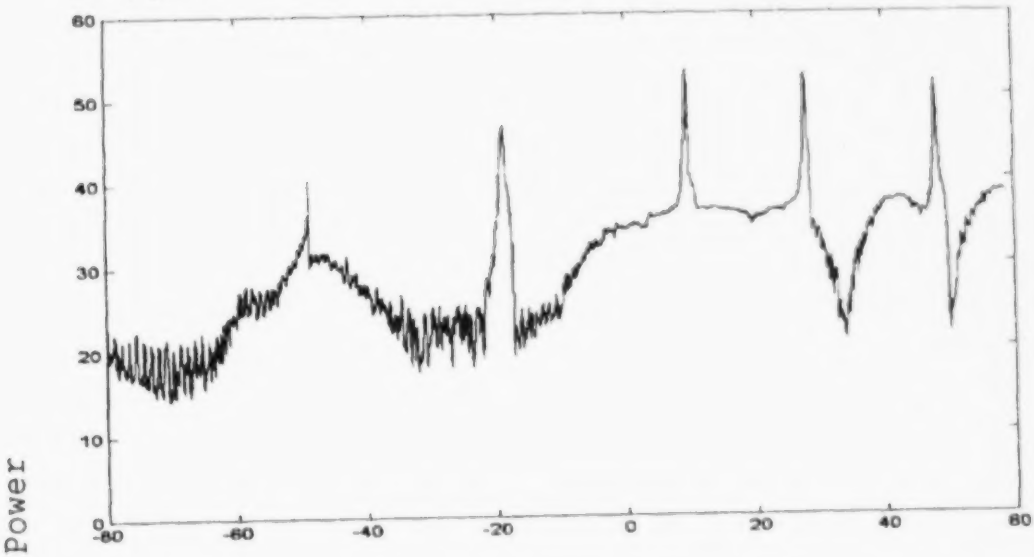

Figure 5b

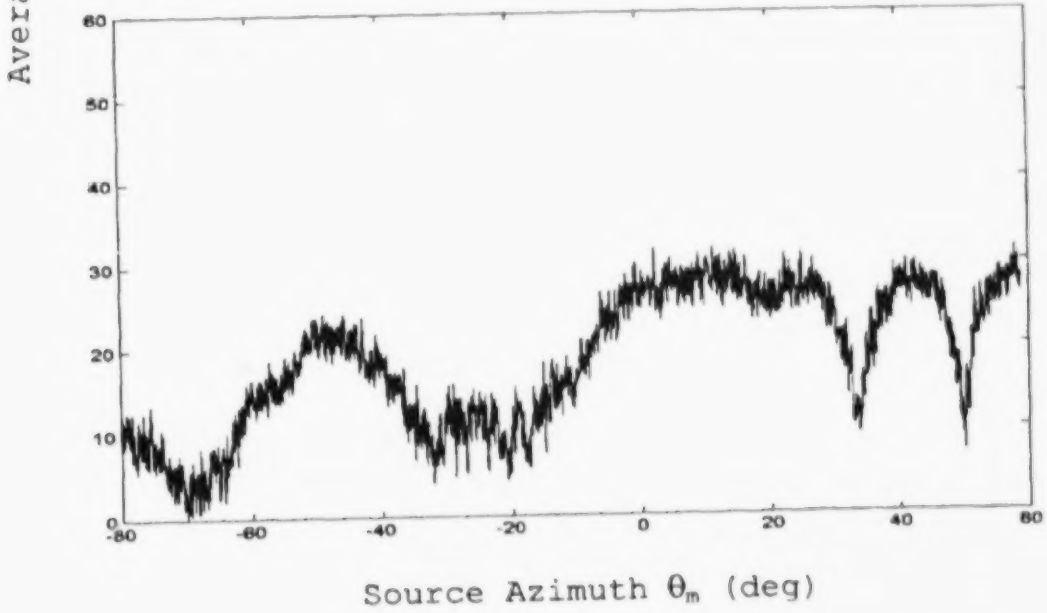

Figures 5a and 5b: Average power at array elements in the 256 preaveraged pulses used to produce one preprocessed snapshot (Figure 5a, top) and average power at array elements in the preprocessed snapshots (Figure 5b, bottom)

4. Performance evaluation

Matrix **C** and two other matrices, denoted by $\mathbf{C}_P$ and $\mathbf{C}_{GP}$, were used in Eq. (5) to calibrate the preprocessed snapshots $\{\mathbf{y}_1,\mathbf{y}_2,...,\mathbf{y}_M\}$. The calibrated snapshots were then used to study the leakage of signal power outside the signal direction, errors in source direction estimates, directional power spectra, signal direction estimates, target resolution, and target detection in the presence of strong interference. $\mathbf{C}_P$ and $\mathbf{C}_{GP}$ were diagonal matrices calculated with the coefficients identified with P and θ_m=0°, respectively, in Table 3, e.g.,

$$\mathbf{C}_P = \text{diag}\{\gamma_1,\gamma_2,...,\gamma_N\} \; . \tag{19}$$

Using $\mathbf{C}_P$ is equivalent to using the single-set phase-only calibration method being used to calibrate the HFSWR and using $\mathbf{C}_{GP}$ is equivalent to using the assumed single-set gain-and-phase method that equalizes the complex element output amplitudes of signals in the boresight direction.

Due to limitations in the calibration data, special emphases were given to results in the azimuth range -75° to 55°. Whenever there was a choice of signal source directions, these directions were restricted to the range -54.0° to 42.7°, because **C** was most effective for signals in this range.

4.1 Leakage power outside signal direction

From Eqs. (1), (2) and (5), one gets

$$\begin{aligned} \mathbf{y}'_m &= \mathbf{C}\mathbf{y}_m \\ &= \mathbf{C}(\alpha_m\mathbf{B}\mathbf{a}_m + \mathbf{e}_m) \\ &= \beta_m(\mathbf{a}_m+\mathbf{b}_m) + \mathbf{e}'_m \; , \end{aligned} \tag{20}$$

where $\beta_m(\mathbf{a}_m+\mathbf{b}_m)$ and $\mathbf{e}'_m$ represent the products $\alpha_m\mathbf{C}\mathbf{B}\mathbf{a}_m$ and $\mathbf{C}\mathbf{e}_m$, respectively. In this expression, β_m is a complex scalar representing the calibrated signal amplitude at the array elements, and $\mathbf{b}_m$ is a vector generated by calibration error. By definition, $\mathbf{b}_m$ is orthogonal to $\mathbf{a}_m$, i.e., $\mathbf{a}_m^H\mathbf{b}_m=\mathbf{b}_m^H\mathbf{a}_m=0$.

In Eq. (20), the component of $\mathbf{e}'_m$ parallel to the signal direction is given by

$$\mathbf{e}'_{m//} = \frac{(\mathbf{a}_m^H\mathbf{e}'_m)\mathbf{a}_m}{\|\mathbf{a}_m\|^2} \; , \tag{21}$$

the component of $\mathbf{e}'_m$ orthogonal to the signal direction is

$$\mathbf{e}'_{m\perp} = \mathbf{e}'_m - \mathbf{e}'_{m//} , \tag{22}$$

the component of $\mathbf{y}^c_m$ orthogonal to the signal direction is

$$\mathbf{y}^c_{m\perp} = \beta_m \mathbf{b}_m + \mathbf{e}'_{m\perp} , \tag{23}$$

and the fraction of total power in $\mathbf{y}^c_m$ outside the signal direction and averaged over all array elements is

$$L(\theta) = \frac{|\mathbf{y}^c_{m\perp}|^2}{|\mathbf{y}^c_m|^2} . \tag{24}$$

The signal term in the calibrated snapshot $\mathbf{y}^c_m$ is $\beta_m(\mathbf{a}_m+\mathbf{b}_m)$ and the term generated by calibration error is $\beta_m\mathbf{b}_m$. When the SINR and the error $\beta_m\mathbf{b}_m$ are both so large that $|\beta_m(\mathbf{a}_m+\mathbf{b}_m)| >> |\mathbf{e}'_m|$ and $|\beta_m\mathbf{b}_m| >> |\mathbf{e}'_{m\perp}|$, one gets $\mathbf{y}^c_m \approx \beta_m(\mathbf{a}_m+\mathbf{b}_m)$, $\mathbf{y}^c_{m\perp} \approx \beta_m\mathbf{b}_m$ and

$$\lim_{\mathrm{SINR},\,|\beta_m|\to\infty} L(\theta) = \frac{|\mathbf{b}_m|^2}{|\mathbf{a}_m+\mathbf{b}_m|^2} . \tag{25}$$

This limit is smaller if the antenna array is more accurately calibrated, because a more accurate calibration method produces a smaller $|\mathbf{b}_m|^2$. It usually has a weak dependence on the source direction, because $\mathbf{b}_m$ depends on the source direction through the $\alpha_m\mathbf{CBa}_m$ term in Eq. (20).

The curve C in Figure 6 shows the values of $L(\theta)$ calculated with $\mathbf{C}$ and every tenth snapshot in the preprocessed calibration data file. It has spikes close to θ_m=48.2°, 27.9°, 9.4°, and -18.9°. These spike directions are also the directions of the first four ionosonde spikes in Figure 5a. Outside the spike regions, the values are between -34.0 and -18.9 dB, corresponding to 0.04 and 1.29%, respectively, of total power. There are no signs of $|\beta_m\mathbf{b}_m| >> |\mathbf{e}'_{m\perp}|$ because the largest and smallest values of $L(\theta)$ differ by more than 15 dB. Besides, from Figure 5b, the regions of lower and larger values of $L(\theta)$ also correspond to the regions of larger and lower average powers, respectively, at the array elements. Curve C_P was calculated with $\mathbf{C}_P$. Here, the values of $L(\theta)$ vary between -12.9 dB (5.20%) and -9.3 dB (11.7%), thus giving a difference of only 3.6 dB between the two limits. This small difference of 3.6 dB is a clear indication of $|\beta_m\mathbf{b}_m| >> |\mathbf{e}'_{m\perp}|$. Curve C_{GP} was calculated with $\mathbf{C}_{GP}$. The values of $L(\theta)$ are between -26.8 dB (0.21%) and -12.4 dB (5.73%). With the exception of a small region close to θ_m=0°, they are larger than those calculated with $\mathbf{C}$ by more than 5 dB.

The leakage azimuth spectrum of a pilot source is also the leakage spectrum of the signals in nighttime interference. These interfering signals are usually over 30 dB stronger than the long-range target signals the HFSWR is designed to detect. Figure 6 indicates serious target detection problems when $\mathbf{C}_P$ is used to calibrate the array snapshots. Suppose a target signal is -30 dB relative to the interference; the leakage from the interference is equal to the lower value of 5.2%; and this leakage is uniformly distributed over all directions. Here, the average leakage power is 52 times the target power at the array elements. Coherent integration

can increase the SINR by a factor 16, which is the number of elements in the receive array. Even with this integration gain, the average leakage power in the target direction is 3.25 (=52/16) times the target power. Therefore, the probability of detecting the target is very low. Usually, the leakage produces one or more false target peaks at unpredictable azimuth directions. The probability of detecting the true target in the presence of these false targets is even lower.

4.2 Errors in direction estimates

The LSAR method was used to calculate a set of five candidate signal direction estimates from every tenth array snapshot with $-75° \le \theta_m \le 55°$. The estimate with the largest power was identified as the source direction estimate in the snapshot. Given an estimate $\hat{\theta}_m$, the error in this estimate was calculated as

$$\mathrm{Err}(\hat{\theta}_m) = \hat{\theta}_m - \theta_m . \tag{26}$$

The calculation of candidate signal direction estimates and the powers associated with the estimates is given in Appendix A.

Figure 7a shows the errors obtained when **C** was used to calibrate the snapshots. The errors are plotted in dot mode. A horizontal line has been added to study their deviations from zero. In the range $-60° < \theta_m < 55°$, most errors have magnitudes less than 0.2°. Figures 7b, calculated with $\mathbf{C}_P$, generally has errors with much larger magnitudes. These errors have a component linearly dependent on the source azimuth. They also increase rapidly in magnitude as θ_m falls below -70°. Figure 7c, calculated with $\mathbf{C}_{GP}$, has errors that are generally between those in Figures 7a and 7b in magnitudes. Like those in Figure 7b, the errors have a linear component and the error magnitude increase rapidly as θ_m falls below -70°.

The linear components of errors in Figures 7b and 7c are consistent with the presence of weak mutual coupling among the array elements for source directions between -60° and 55°. The rapid increase for $\theta_m < -70°$ could be caused by a rapid increase in coupling.

4.3 Directional power spectra of calibration data

The Capon minimum variance method [1-3] was used to calculate the directional power spectra of every tenth snapshot with $-75° \le \theta_m \le 55°$. These spectra were defined as

$$P(\theta) = \frac{\text{Power arriving at array elements from spectral direction } \theta}{\text{Total power at array elements}} . \tag{27}$$

A brief description of the calculation of Capon directional spectra is given in Appendix B.

Figure 8a shows the dependence of $P(\theta)$ on source azimuth θ_m when **C** was used to calibrate the preprocessed snapshots. It has a strong source track from the lower left corner, where $\theta = \theta_m = -75°$, to the upper right, where $\theta = \theta_m = 55°$. For each θ_m, there is at least one

spectral azimuth region with $P(\theta)<-40$ dB. The figure also indicates generally larger values of $P(\theta)$ for $\theta<-50°$ and $\theta>50°$. Figure 8b is calculated with $\mathbf{C}_P$. The source track is significantly broader; the values of $P(\theta)$ outside the main beam are significantly higher; and there are large interference patches up to the -17 dB level all over the place. Figure 8c is calculated with $\mathbf{C}_{GP}$. The source track is narrowest in the $\theta_m \approx 0°$ azimuth region. Outside this region, the width increases as the deviation of θ_m from 0° increases. At $\theta_m = \pm 55°$, the widths are approximately half of those calculated with $\mathbf{C}_P$. The figure also has interference patches up to the -17 dB level. Compared with Figure 8b, the patches are fewer in number and are farther away from the source azimuth.

Figures 9a to 9c each contain the spectra of six snapshots with $\theta_m \approx 40°$ in Figures 8a to 8c, respectively. In Figure 9a, $P(\theta)$ falls rapidly to approximately -36 dB as the deviation of θ from θ_m increases to about 10°. Left of the signal peak, $P(\theta)$ continues to fall and is below -40 dB in the region $-50° \leq \theta < 25°$. For $\theta < -50°$, $P(\theta)$ is generally larger than -40 dB and some values are close to -36 dB. In Figure 9b, the signal peaks are significantly broader than those in Figure 9a and the values of $P(\theta)$ outside the signal region are up to 20 dB higher. There are also false peaks in the region $\theta \approx -7°$. This region is inside an interference patch in Figure 8b. In Figure 9c, the widths of the signal peaks and the values of $P(\theta)$ outside the signal region are between those in Figures 9a and 9b. There are false peaks in the region $\theta \approx 2°$.

The slightly higher background for $\theta \leq -50°$ in Figures 8a and 9a probably originated from diffuse signal scattering at the cliff, which is northeast of the receive array in Figure 1.

The directional spectrum of a pilot source at azimuth θ_m is also the directional spectrum of a strong skywave interference at interference azimuth θ_I, with $\theta_I = \theta_m$. Patches of interference up to the -17 dB level in Figure 8b are signs of total disaster in target detection at night when $\mathbf{C}_P$ is used. These patches generate false targets and bury the long-range targets at once.

4.4 Direction estimates calculated with calibration data

The LSAR method was used to calculate five candidate signal direction estimates from every tenth preprocessed snapshot. The four with the strongest powers were then plotted in dot mode and the fifth was discarded to avoid overcrowding. Figures 10a, 10b and 10c show the results obtained by calibrating the snapshots with $\mathbf{C}$, $\mathbf{C}_P$ and $\mathbf{C}_{GP}$, respectively. Figure 10a gives the correct source track, which is a straight-line joining the lower left corner, where $\theta = \theta_m = -75°$, with the upper right, where $\theta = \theta_m = 55°$. Figures 10b and 10c give source tracks that are slightly tilted. The tracks are also slightly bent at the lower left corner. Both figures have false tracks. Compared with Figure 10b, the false tracks in Figure 10c are fewer in number and are farther away from the source track.

The shapes of source tracks in Figures 10b and 10c agree with the errors in source direction estimates in Figure 7b and 7c. The false tracks are inside the interference patches in Figure 8b and 8c. The figures do not contain the same number of dots, because some direction estimates are non-physical and some are outside the range in the figures.

P516914.PDF [Page: 44 of 96]

4.5 Target resolution

Target resolution was studied with a synthetic data file containing a moving target and a fixed target with the same strength. The snapshots in the file were denoted by the set $\{z_1, z_2, \ldots, z_M\}$ and were generated as

$$z_m = \exp[\phi_m]\tilde{y}_m + \exp[\phi_{mF}]\tilde{y}_F , \qquad m=1,2,\ldots,M , \qquad (28)$$

where

$$\tilde{y}_m = \frac{y_m}{|y_m|} \qquad (29)$$

was preprocessed snapshot y_m normalised to unit magnitude, $\tilde{y}_F$ was the $\tilde{y}_m$ with source direction $\theta_m=\theta_F$, θ_F was the direction of the fixed target, and ϕ_m and ϕ_{mF} were random phases.

A set of 526 synthetic snapshots was generated with $\theta_F \approx 30°$ and snapshots with θ_m between -50° and -10°. Figures 11a, 11b and 11c contain the Capon directional spectra obtained by using $\mathbf{C}$, $\mathbf{C}_P$ and $\mathbf{C}_{GP}$, respectively, to calibrate the synthetic snapshots. The two target tracks are the narrowest in Figure 11a and the broadest in Figure 11c. These tracks are resolved in Figure 11a if $|\theta_m-\theta_F| \geq 5°$. In contrast, they are not resolved in Figures 11b and 11c unless $|\theta_m-\theta_F| > 10°$. There is a false target track between $\theta=-5°$ and $\theta=15°$ in Figure 11c.

Some Capon directional spectra with $\theta_m \approx \theta_F$ are extracted from Figures 11a to 11c and plotted in Figures 12a to 12c, respectively. Each spectrum has a strong peak close to θ_F. The peaks in Figure 12a are the narrowest and those in Figure 12b are the broadest. Figure 12c has false peaks with $P(\theta) > -23$ dB in the region $\theta \approx 10°$. These false peaks are inside the false track in Figure 11c.

Figures 13a to 13c show the two strongest candidate signal direction estimates calculated with the calibrated snapshots and the LSAR method. In agreement with the results in Figure 11a and 11c, the targets are resolved in Figure 13a and 13c if $|\theta_m-\theta_F| \geq 5°$ and $|\theta_m-\theta_F| > 10°$, respectively. However, in total disagreement with the results in Figure 11b, the targets in Figure 13b are resolved for all values of θ_m, including the special case of $\theta_m=\theta_F$. There is a false target in Figure 13c.

The contradicting results on target resolution in Figure 11b and 13b indicate that something catastrophic had happened. The LSAR method attempts to fit an array snapshot with sinusoids, with each sinusoid associated with a different signal direction. When a snapshot has a directional spectrum with a broad and strong peak, the method may fit the snapshot with more than one sinusoids close in directions. Line splitting occurs when it generates two direction estimates less than one one-way array beamwidth apart and only one signal source is actually present. One one-way array beamwidth in array steering direction θ, with $\theta=\theta_F$, is approximately 10.3° ($\approx 50.8° / Nd\cos\theta$) for $\theta_F=30°$.

Broadening of a strong signal peak occurs if there are errors in antenna calibration. In the case of a poorly calibrated antenna array, the peak could be so broad that the LSAR

method generates more than one direction estimates close to the true source direction. Line splitting had occurred when $\mathbf{C}_P$ was used to calibrate the array snapshots and the LSAR method then used to calculate signal direction estimates. The case of $\theta_m=\theta_T$ corresponded to a single strong signal source present. One should not have obtained two estimates close to θ_T.

Whenever there is a possibility of line splitting, the existence of two estimates close in direction does not automatically imply the existence of two targets close in direction. All claims of targets close in directions must therefore be verified with information from other sources, e.g., prior knowledge of two targets present.

Other examples of line splitting can be found in Figure 10b in regions with source azimuth θ_m≈-35°, -5° and 42°.

4.6 Target detection in presence of strong interference

Target detection in the presence of strong interference was studied with a synthetic file containing K=401 snapshots, a target at azimuth direction θ_T=-30°, and J=6 interference signals with interference directions close to 40°. The snapshots were generated as

$$\mathbf{z}_k = \rho_k \exp[\phi_k]\tilde{\mathbf{y}}_T + \exp[\phi_{k1}]\tilde{\mathbf{y}}_{I1} + \exp[\phi_{k2}]\tilde{\mathbf{y}}_{I2} + \ldots + \exp[\phi_{kJ}]\tilde{\mathbf{y}}_{IJ}\,, \qquad k=1,2,\ldots,K\,, \qquad (30)$$

Parameter ρ_k was a real scalar related to the target SINR in $\mathbf{z}_k$ by

$$\mathrm{SINR} = \frac{\rho_k^2}{J}\,. \qquad (31)$$

The set $\{\phi_k,\phi_{k1},\phi_{k2},\ldots,\phi_{kJ}\}$ were random phases, $\tilde{\mathbf{y}}_T$ was the normalised array snapshot $\tilde{\mathbf{y}}_m$ with $\theta_m=\theta_T$, and the set $\{\tilde{\mathbf{y}}_{I1},\tilde{\mathbf{y}}_{I2},\ldots,\tilde{\mathbf{y}}_{IJ}\}$ was a set of normalised snapshots with source directions close to 40°. The directional spectra of these J interference snapshots are given in Figures 9a to 9c.

Two sets of results are presented. The first set is calculated with the LSAR method and the second is calculated with the discrete Fourier transform (DFT) method. The results of the DFT method are included, because this method is being used in target detection with the HFSWR at night.

Figure 14a shows the Capon directional spectra obtained by using $\mathbf{C}$ to calibrate the synthetic snapshots. The tracks at θ=-30° and 40° are generated by the target and interference, respectively. The power, width and azimuth fluctuations in these tracks reflect the use of random phases on the right hand side of Eq. (30). As SINR increases from -50 dB, faint target peaks begin to appear at SINR=-42 dB. The peaks become clearly visible for SINR>-35 dB. Figure 14b shows the spectra calculated with $\mathbf{C}_P$. The target and interference peaks are wider. With very few exceptions, the target peak is not visible unless SINR>-23 dB. There are false target tracks at θ=-55° and -5°. Figure 14c was calculated with $\mathbf{C}_{GP}$. Here, the peak widths are

between those calculated with $\mathbf{C}$ and $\mathbf{C}_P$; the target peaks are faint at SINR=-36 dB and are clearly visible for SINR>-30 dB; and there are signs of a false track at $\theta \approx 5°$.

Figures 15a, 15b and 15c each contains ten Capon directional spectra in Figures 14a, 14b and 14c, respectively. The SINR's were ≈-40, -23 and -33 dB, respectively, and were chosen to make 50% of the spectra in each figure possess a peak close to the target direction. Besides the five target peaks, Figure 15a has four broad peaks with $P(\theta)<-32$ dB at $\theta \approx -60°$. It also has a spectrum with a significantly stronger signal peak and a very distorted interference peak. Figure 15b has a false peak with $P(\theta) \approx -19$ dB at $\theta \approx -8$ in nine of the ten spectra. There are signs of broad peaks at $\theta \approx -60°$. All values of $P(\theta)$ for $\theta < -50°$ exceed -22 dB. Figure 15c has a false peak with $P(\theta) \approx -24$ dB at $\theta \approx 5°$ in every spectrum. The spectra are essentially flat for $\theta < -50°$.

The peaks at $\theta \approx -60°$ in Figure 15a were probably generated by diffuse scattering of signals at the cliff northeast of the receive antenna array. These scattered signals were too weak to produce peaks in Figures 15b and 15c. The spectrum with a distorted interference peak was generated by a $\mathbf{z}_k$, in which the J interference signals on the right hand side of Eq. (30) summed destructively. This destructive summation was also the reason for a significantly stronger signal peak in the spectrum, because the denominator on the right hand side of Eq. (27) was smaller.

Figures 16a to 16c contain the LSAR output candidate direction estimates calculated with the same snapshots used in Figures 14a to 14c, respectively. To avoid overcrowding in the figures, the weakest of the five candidate signal direction estimates was deleted from every snapshot. As SINR increases from -50 dB, Figure 16a, calculated with $\mathbf{C}$, has signs of a target track at SINR=-35 dB and a clearly visible track for SINR>-33 dB. Figure 16b, calculated with $\mathbf{C}_P$, has signs of a target track at SINR=-18 dB and a clearly visible track for SINR>-15 dB. It has false tracks at $\theta \approx -55°$, -7° and 0°. Figure 16c, calculated with $\mathbf{C}_{GP}$, has signs of a target track at SINR=-30 dB and a clearly visible track for SINR>-27 dB. It has a false track at $\theta \approx 0°$.

The above results show that the use of $\mathbf{C}$ instead of the phase-only $\mathbf{C}_P$ could reduce the SINR target detection threshold by approximately 17 dB, when an extremely strong interference is present. Based on this reduction, the use of $\mathbf{C}$ could increase the maximum nighttime target detection range of the HFSWR by over 50%. The results also show that the use of $\mathbf{C}$ instead of the gain-and-phase $\mathbf{C}_{GP}$ could reduce the SINR target detection threshold by 5 to 8 dB. This reduction agrees with the results in [15-18], where the reductions are between 4 and 8 dB.

DFT results

The DFT estimates of signal directions and powers in a calibrated array snapshot $\mathbf{y}^c_m$ were calculated with the following procedure.

Step 1.

Calculate a new snapshot $\tilde{\mathbf{y}}^c_m$ as

$$\tilde{\mathbf{y}}_m^c = \frac{\mathbf{y}_m\sqrt{N}}{|\mathbf{y}_m|}. \tag{32}$$

Step 2.

Specify spectral azimuth direction θ.
Calculate the array steering vector $\mathbf{a}$ for this direction with Eq. (16), using $\theta_m=\theta$.

Step 3.

Calculate the complex DFT amplitude as

$$\mathbf{z} = \frac{\mathbf{a}^H\tilde{\mathbf{y}}_m^c}{N}. \tag{33}$$

Step 4.

Calculate the spectral power as

$$P(\theta) = |\mathbf{z}|^2. \tag{34}$$

Step 5.

Repeat Steps 2 to 4 with many azimuth directions equally spaced in the range -90° to 90° to produce a DFT spectrum.
Identify the peak positions in the spectrum as candidate signal direction estimates.
Identify the peak powers as signal power estimates.

In Step 1 the average power at the array elements in $\tilde{\mathbf{y}}_m^c$ is unity, because $|\tilde{\mathbf{y}}_m^c|^2=N$ and N is the number of array elements. In Step 2, the division by N ensures that $\mathbf{z}$ is equal to the complex signal amplitude in $\tilde{\mathbf{y}}_m^c$, if only one signal source is present and θ is also the source direction.

Figures 17a, 17b and 17c show the DFT spectra calculated with the synthetic snapshots and calibration matrices $\mathbf{C}$, $\mathbf{C}_P$ and $\mathbf{C}_{GP}$, respectively. The target and interference peaks are significantly broader than those in Figures 14a to 14c. There are many false peaks and the target peak, located at $\theta=\theta_T=-30°$, is weaker than the nearest false peak unless SINR>-25 dB. The major differences among the figures are the locations and the power levels of the false peaks.

Figure 18 shows the DFT spectra calculated with the SINR=-50 dB synthetic snapshot. The spectrum calculated with $\mathbf{C}$ (black) has eight sidelobes in the range -75° to 55°. It looks like the ideal DFT spectrum of a pure signal with source direction close to 40°. The spectrum calculated with $\mathbf{C}_{GP}$ (blue) has sidelobes in approximately the same positions. However, the peak powers differ noticeably from those of the ideal spectrum. The spectrum calculated with $\mathbf{C}_P$ (red) only has six sidelobes in the range -75° to 55°. The sidelobe positions and powers differ noticeably from those of an ideal DFT spectrum.

Figures 19a to 19c contain the four strongest signal direction estimates in each DFT spectrum in Figures 17a to 17c, respectively. These figures do not have a firmly established target at θ=-30° unless SINR>-25 dB. There are at least two false targets present. The major

differences among the figures are the scattering of the target direction estimates and the locations of the false targets.

The above results show that it is difficult use the DFT to detect a target more than 25 dB below a strong and highly direction interference and that this difficulty cannot be mitigated with an accurate receive antenna calibration. The results are not unexpected, because the aperture of the HFSWR is less than 6 wavelengths at 3.2 MHz, the DFT has eight sidelobes in the range -75° to 55°, and the peak value of the weakest sidelobe is -24.0 dB below the main peak.

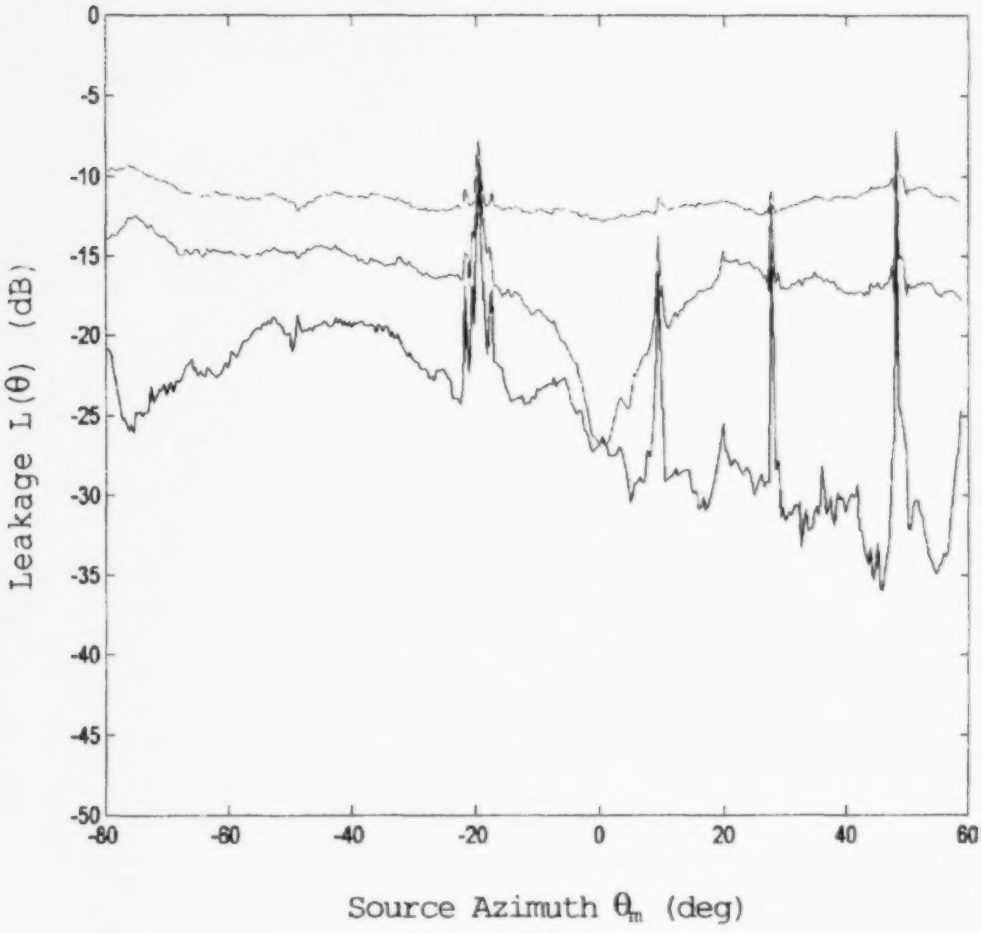

Figure 6: Leakage power calculated with **C** (black), phase-only matrix $\mathbf{C}_P$ (red), and gain-and-phase matrix $\mathbf{C}_{GP}$ (blue).

Figure 7a

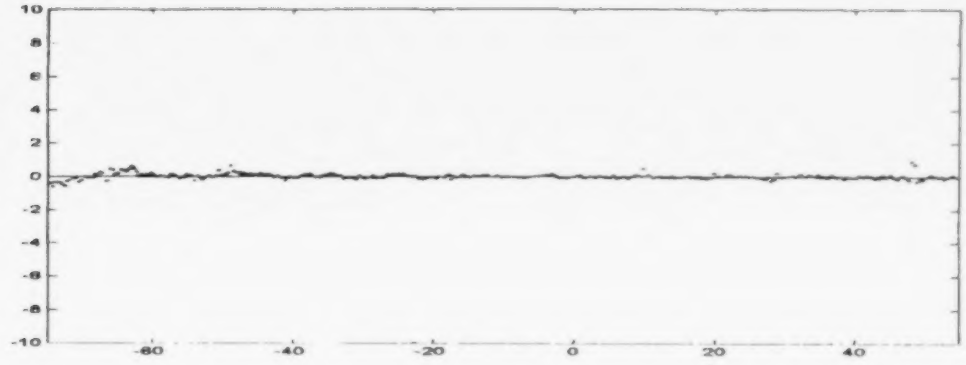

Figure 7b

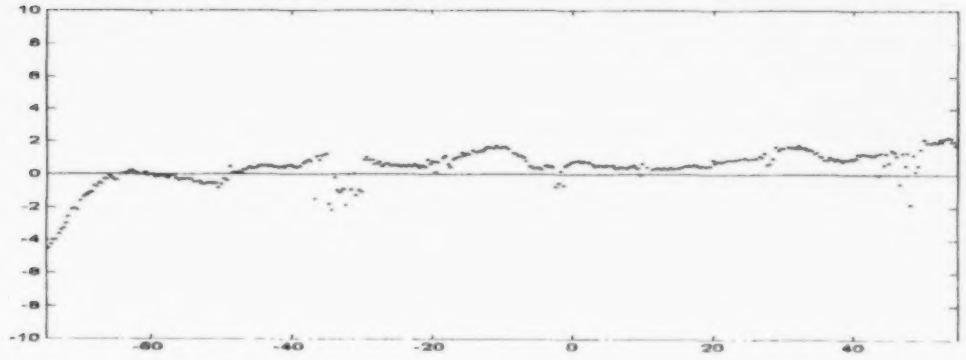

Figure 7c

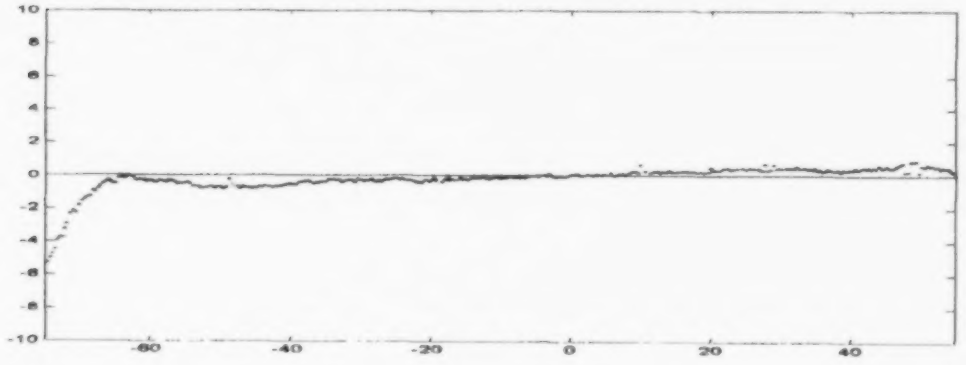

Figures 7a, 7b and 7c: Errors in source direction estimates from snapshots with $-75° \le \theta_m \le 55°$, using calibration matrices **C** (Figure 7a, top), $\mathbf{C}_P$ (Figure 7b, middle), and $\mathbf{C}_{GP}$ (Figure 7c, bottom)

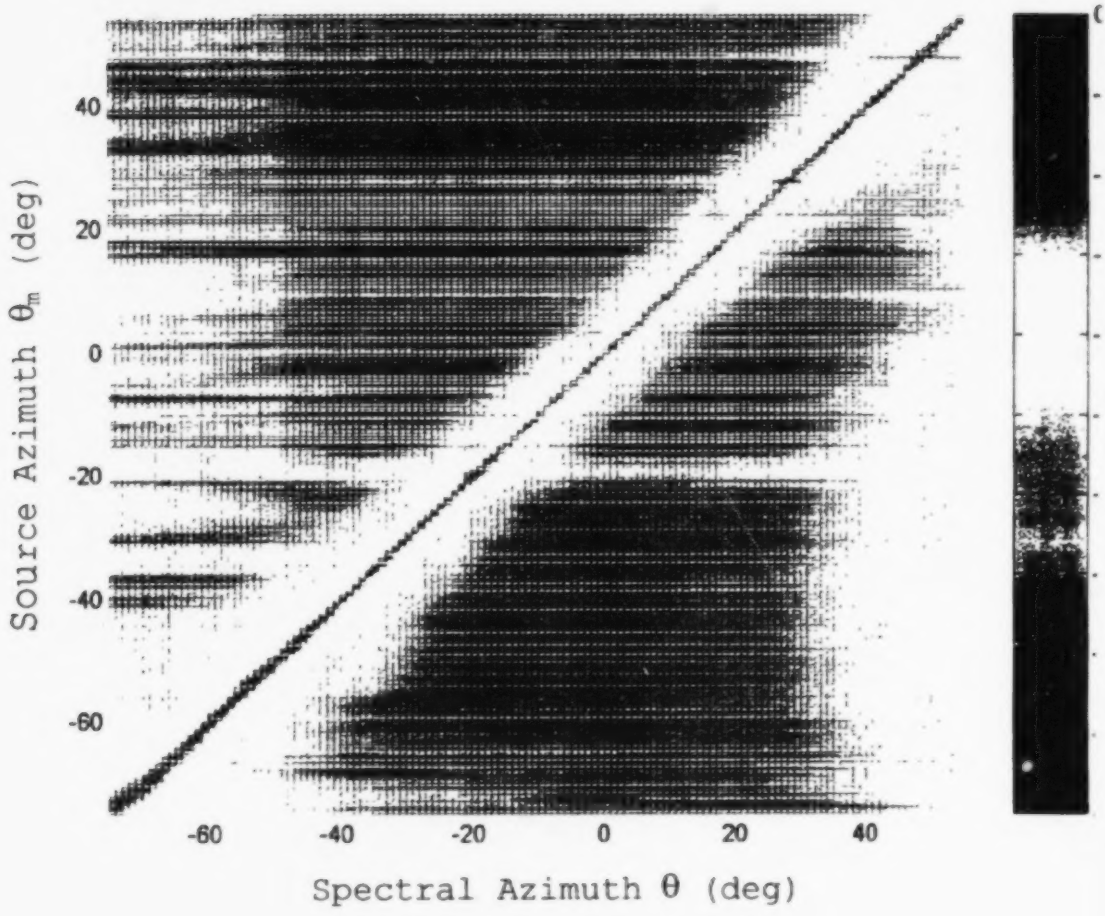

Figure 8a: Directional spectra of array snapshots in preprocessed calibration data file. Matrix C was used to calibrate the snapshots.

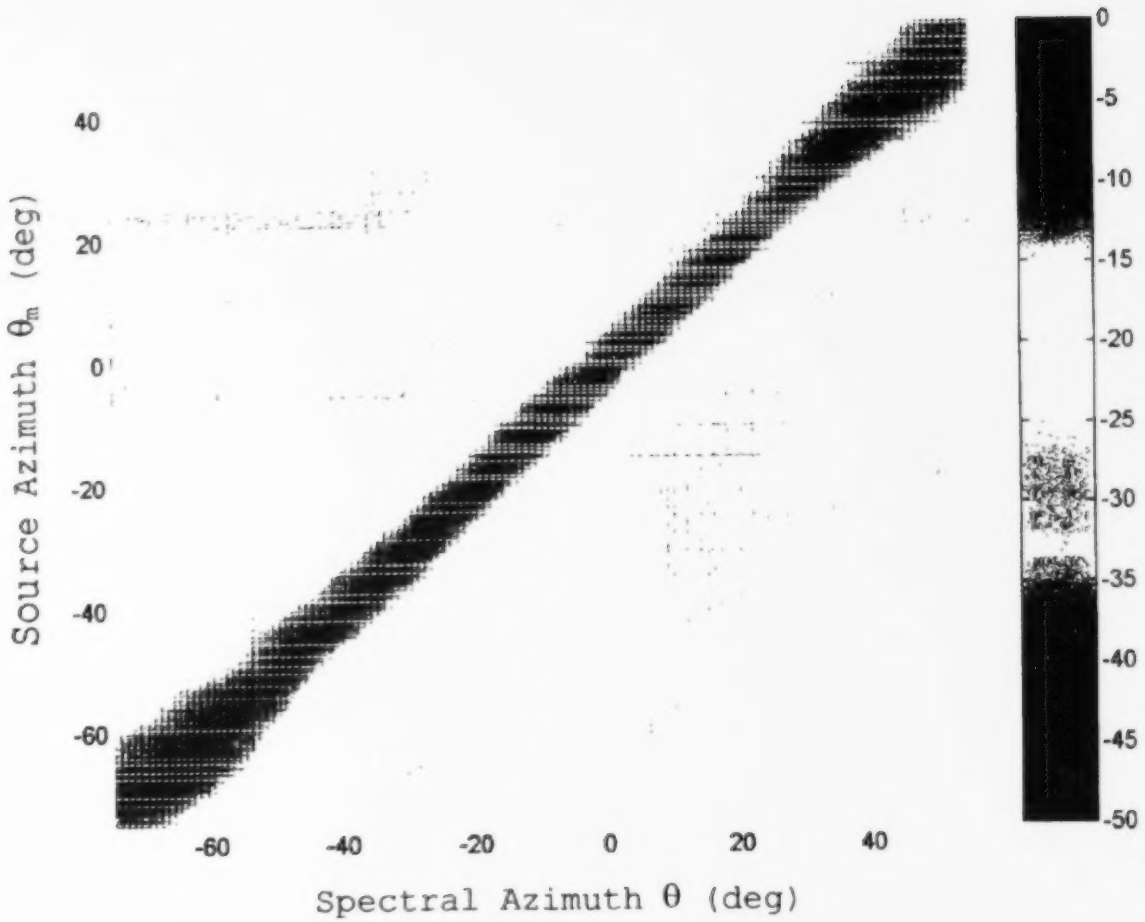

Figures 8b: Directional spectra of array snapshots in preprocessed calibration data file Phase-only C_P was used to calibrate the snapshots.

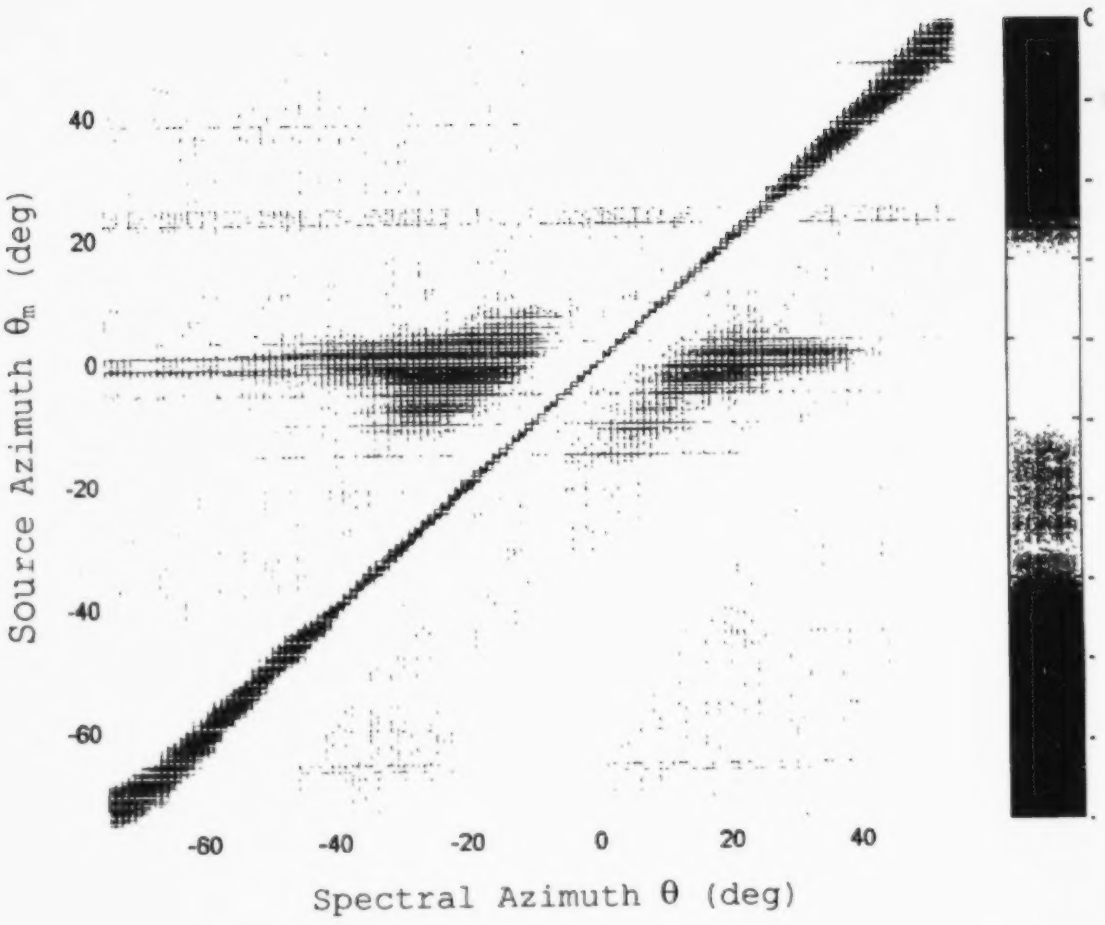

Figure 8c: Directional spectra of array snapshots in preprocessed calibration data file. Gain-and-phase matrix C_{GP} was used to calibrate the snapshots.

P516914.PDF [Page: 54 of 96]

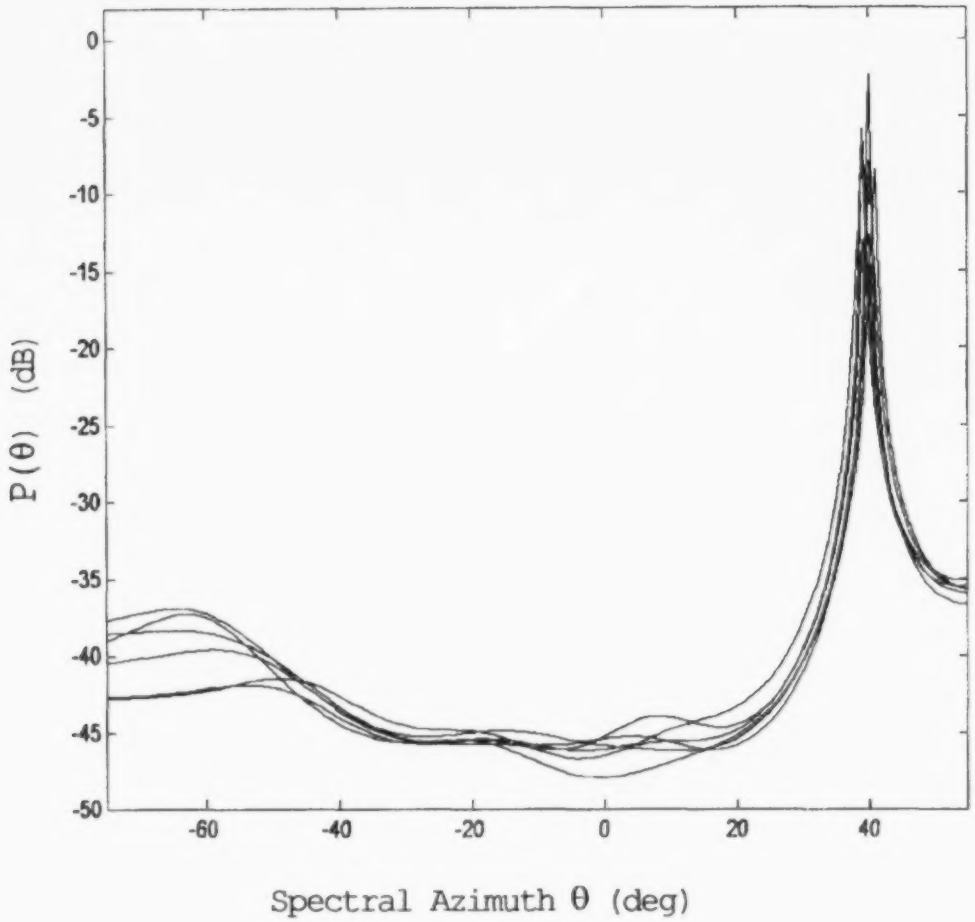

Figure 9a: Directional spectra of six array snapshots with source azimuth θ_m=40°. Matrix **C** was used to calibrate the snapshots.

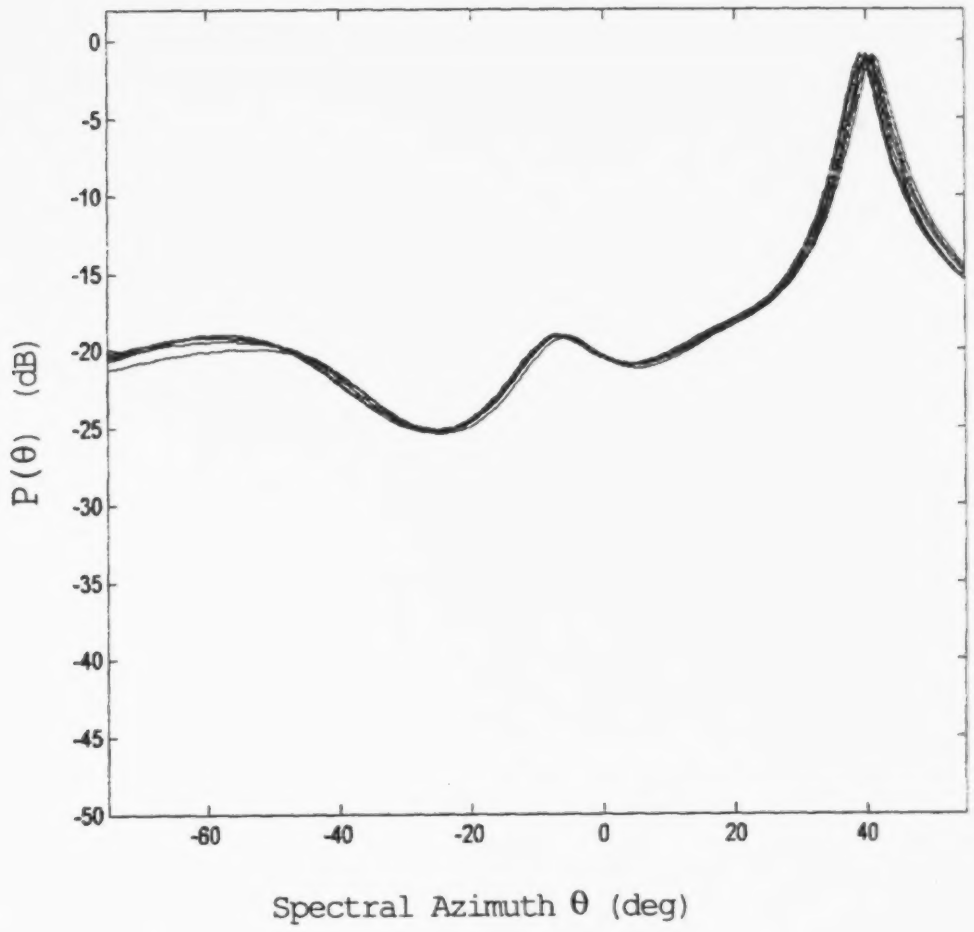

Figure 9b: Directional spectra of six array snapshots with source azimuth θ_m=40°. Phase-only matrix C_P was used to calibrate the snapshots.

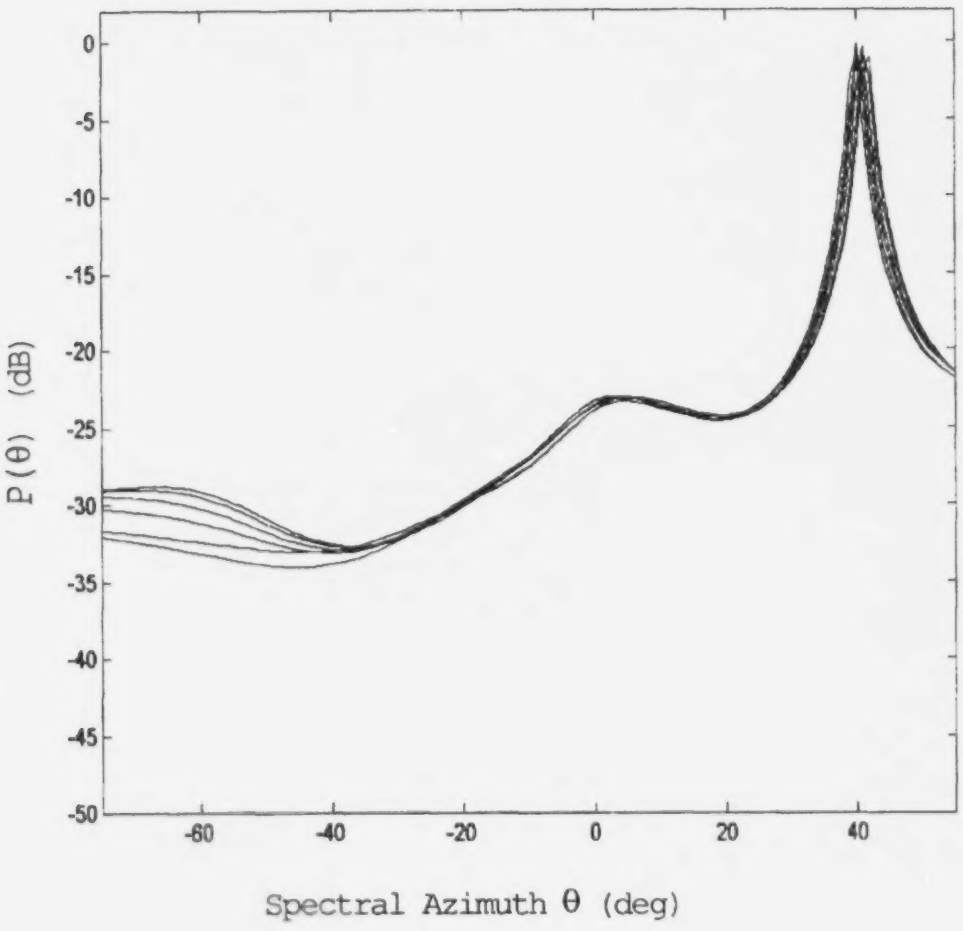

Figure 9c: Directional spectra of six array snapshots with source azimuth θ_m=40°. Gain-and-phase matrix C_{GP} was used to calibrate the snapshots.

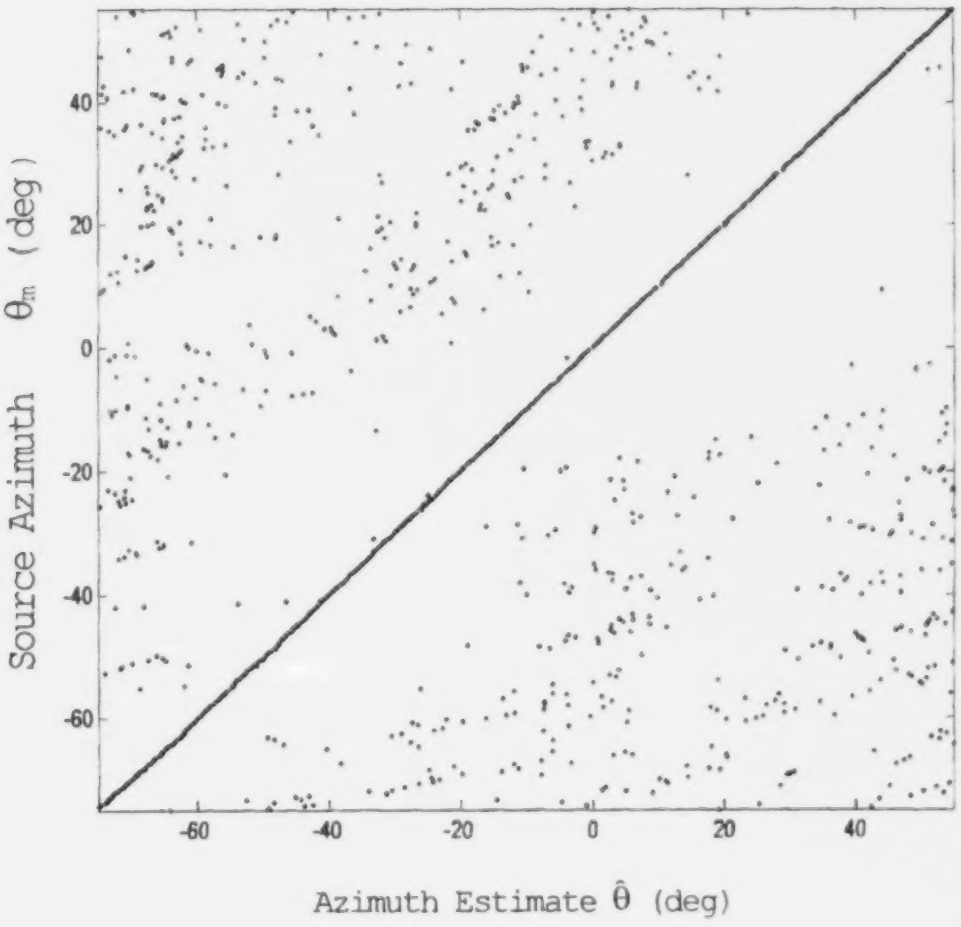

Figure 10a: Candidate direction estimates calculated with the preprocessed array snapshots. Matrix C was used to calibrate the snapshots.

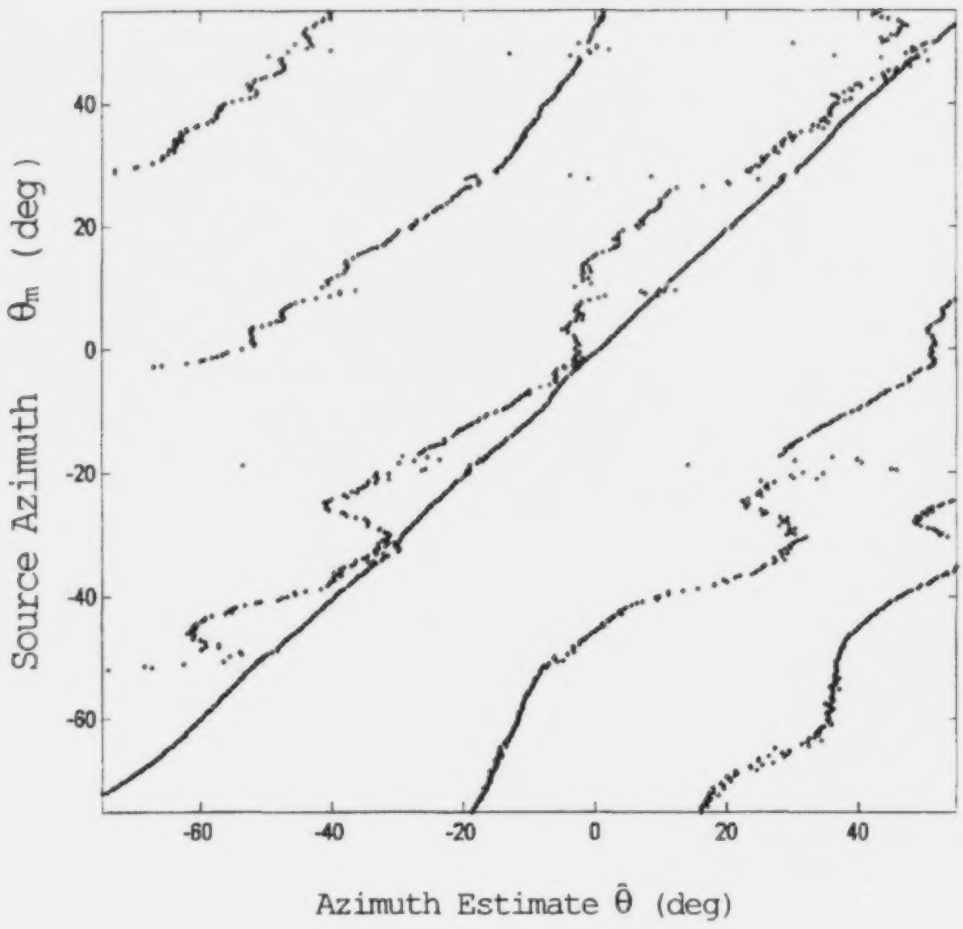

Figure 10b: Candidate direction estimates calculated with the preprocessed array snapshots. Phase-only matrix C_P was used to calibrate the snapshots.

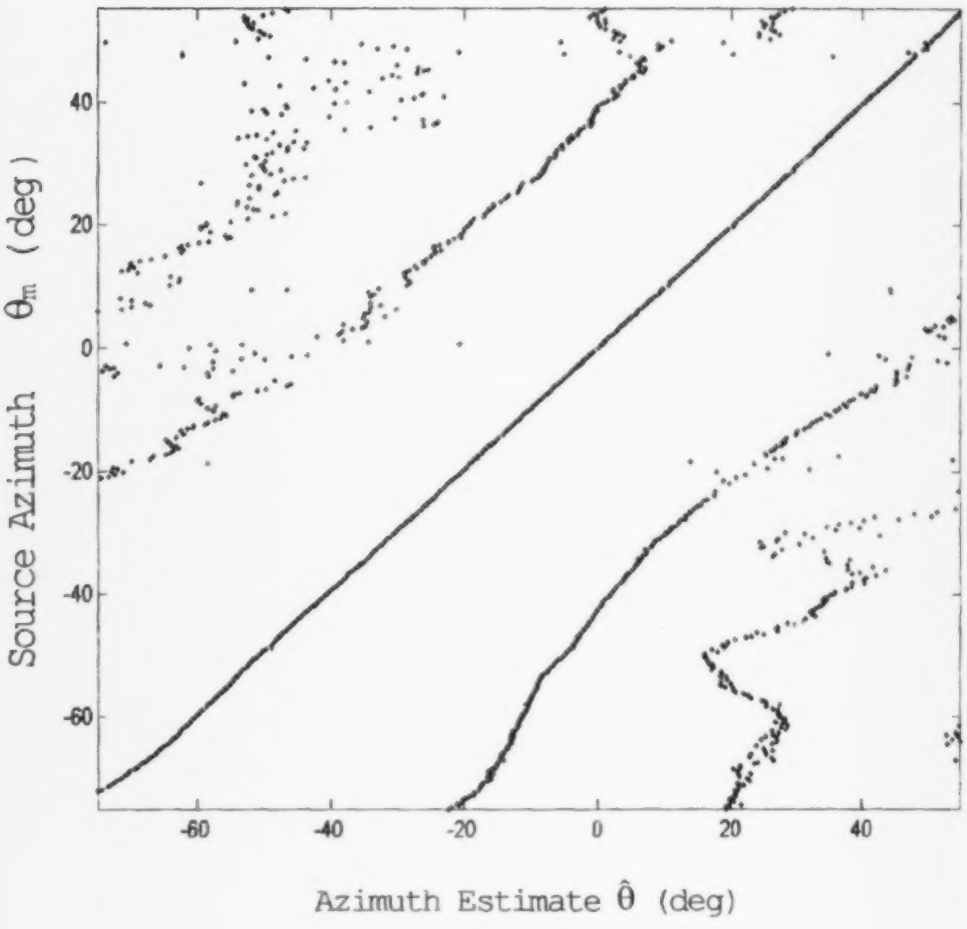

Figure 10c: Candidate direction estimates calculated with the preprocessed array snapshots. Gain-and-phase matrix C_{GP} was used to calibrate the snapshots.

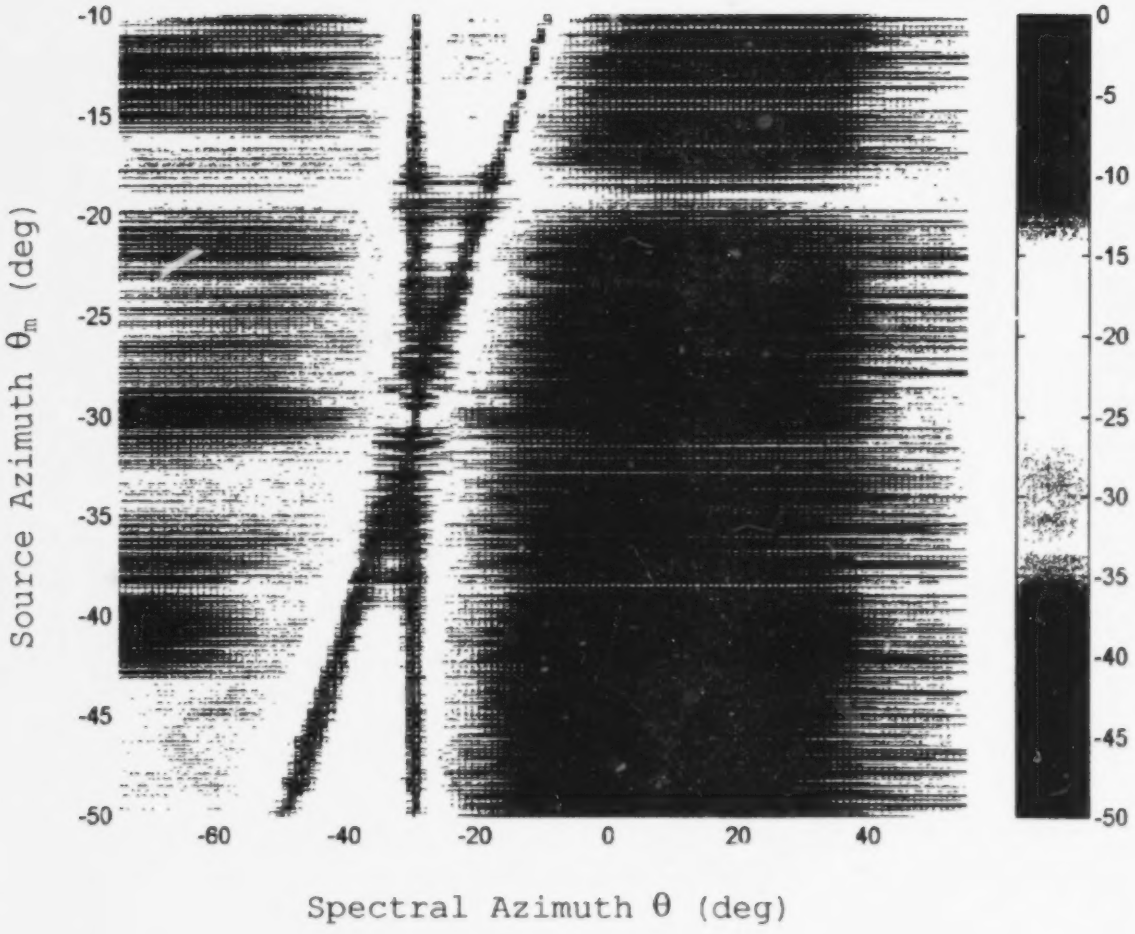

Figure 11a: Directional spectra of two equal-strength intersecting targets. Matrix **C** was used to calibrate the snapshots.

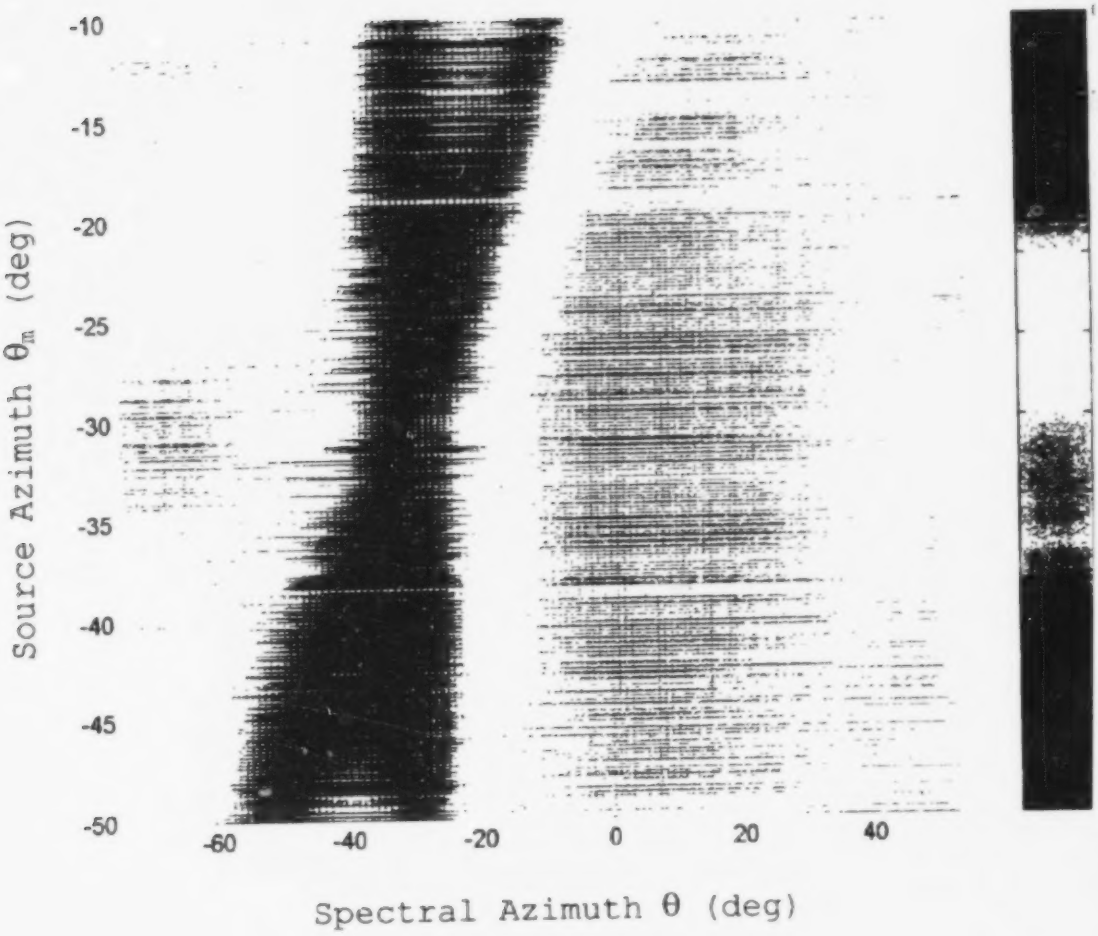

Figure 11b: Directional spectra of two equal-strength intersecting targets. Phase-only matrix C_P was used to calibrate the snapshots.

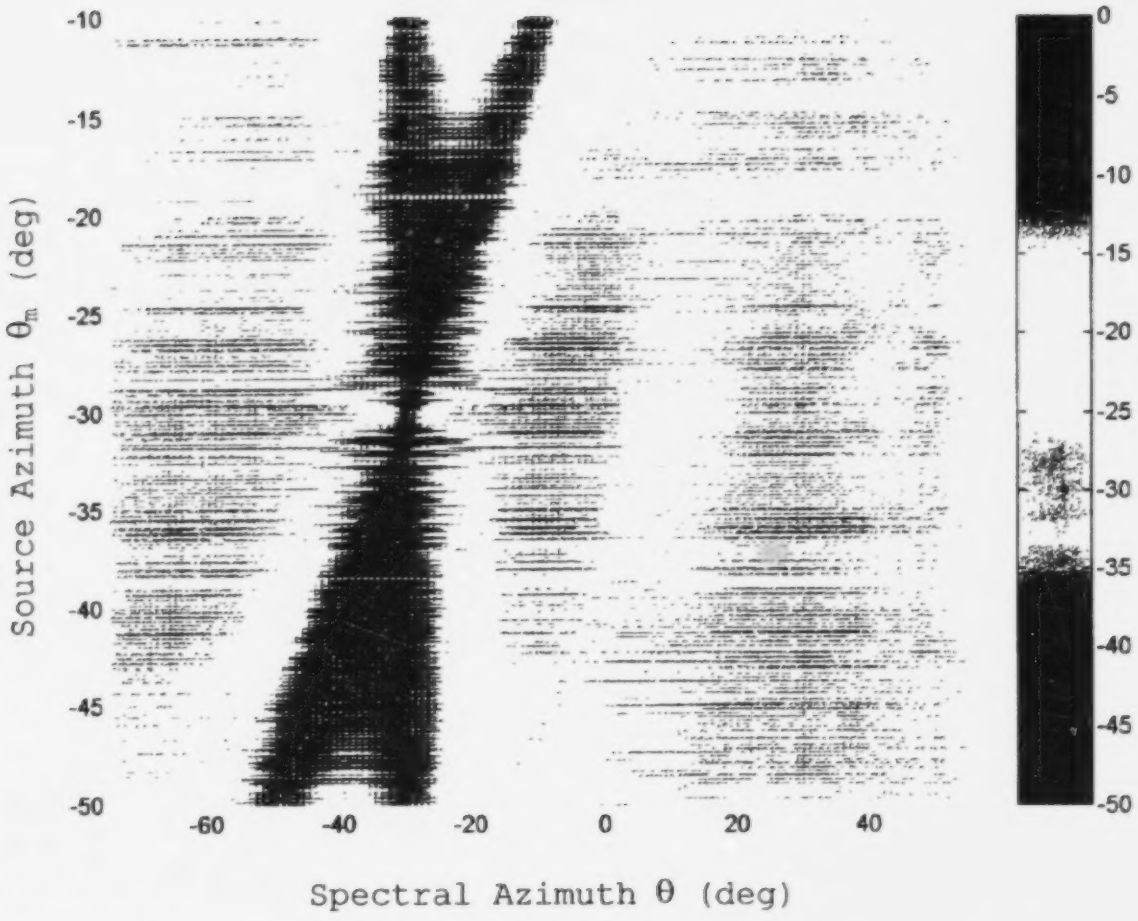

Figure 11c: Directional spectra of two equal-strength intersecting targets. Gain-and-phase matrix C_{GP} was used to calibrate the snapshots.

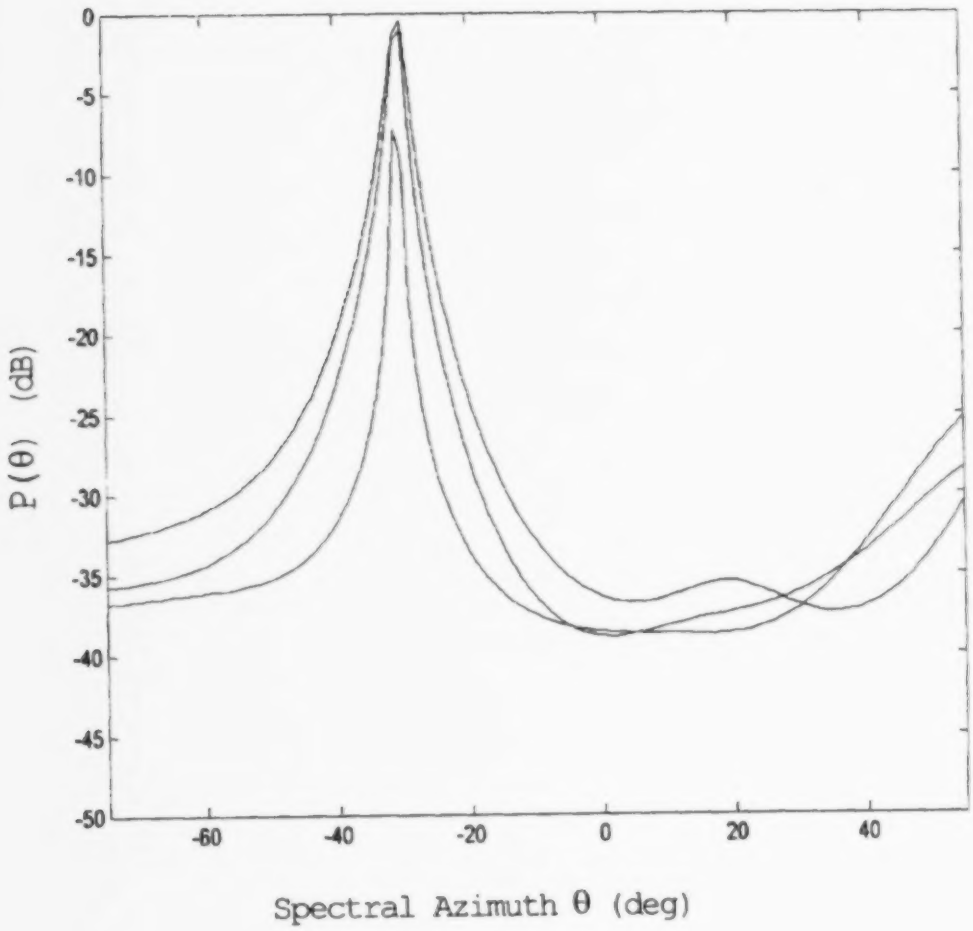

Figure 12a: Some directional spectra of synthetic snapshots with azimuth θ_m=-30°. Matrix C was used to calibrate the snapshots.

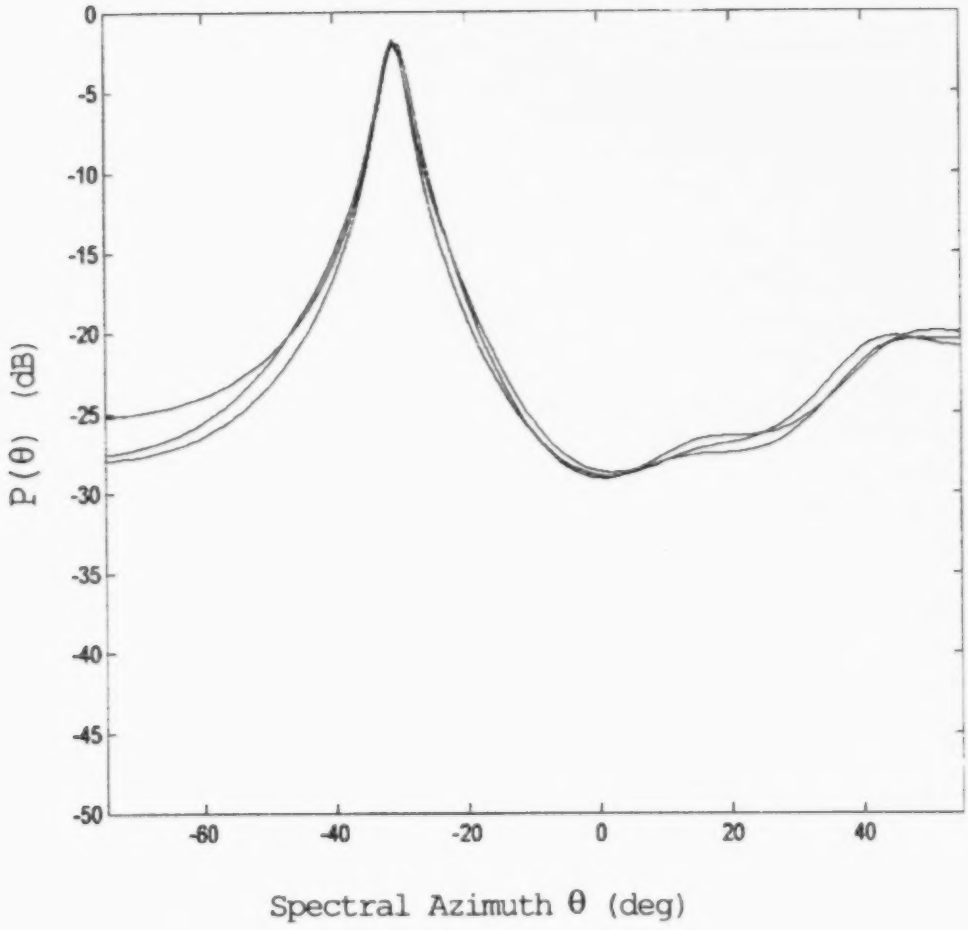

Figure 12b: Some directional spectra of synthetic snapshots with azimuth θ_m=-30°. Phase-only matrix C_P was used to calibrate the snapshots.

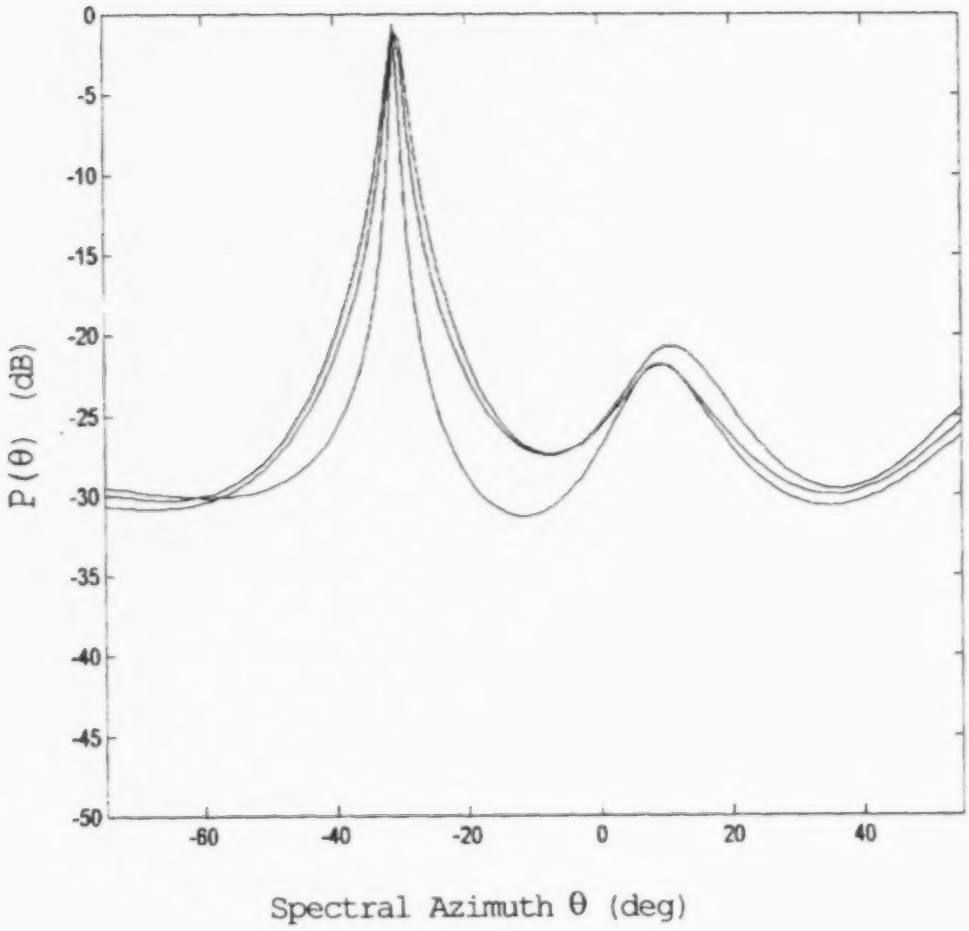

Figure 12c: Some directional spectra of synthetic snapshots with azimuth θ_m=-30°. Gain-and-phase matrix C_{GP} was used to calibrate the snapshots.

P516914.PDF [Page: 66 of 96]

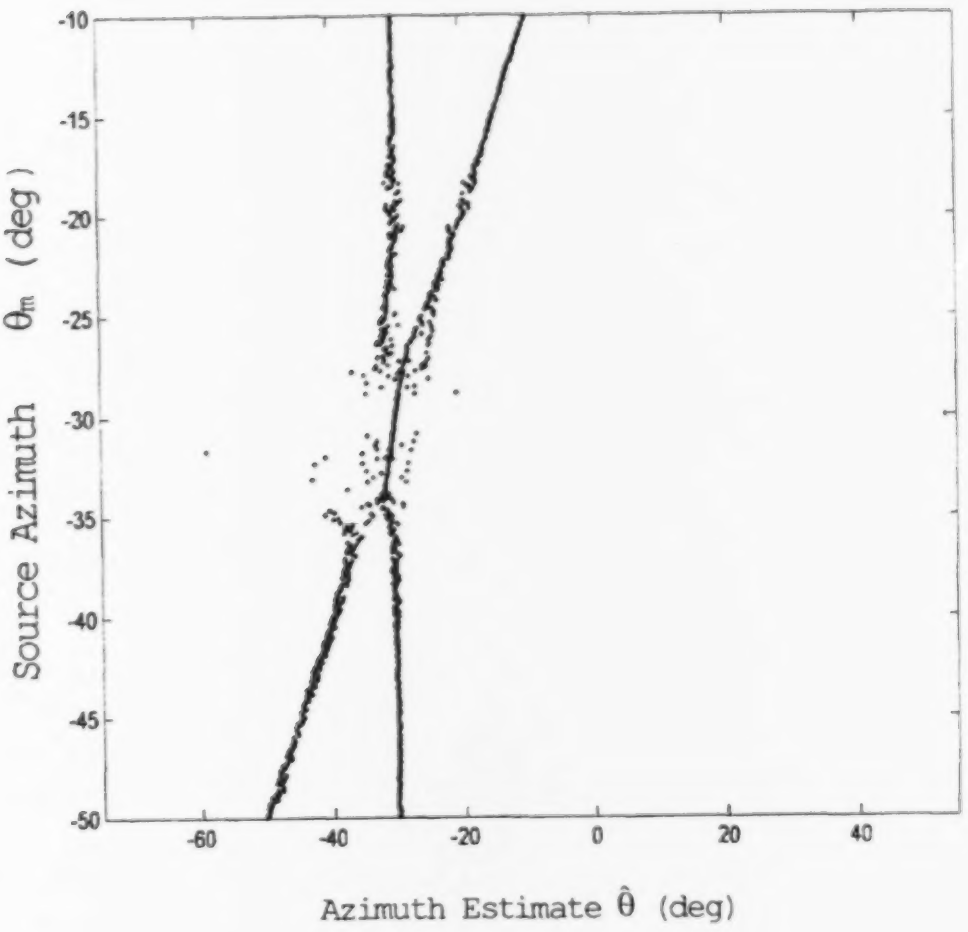

Figure 13a: Candidate direction estimates calculated with the synthetic snapshots used to produce Figure 11a. Matrix **C** was used to calibrate the snapshots.

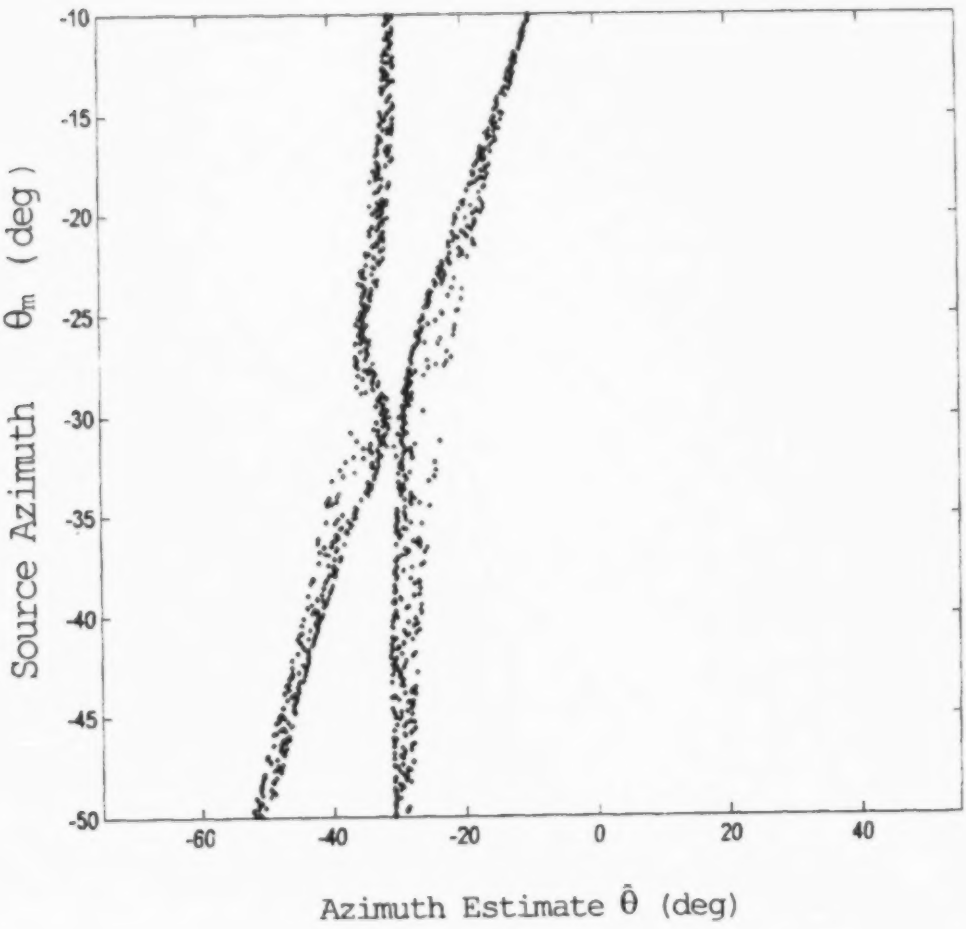

Figure 13b: Candidate direction estimates calculated with the synthetic snapshots used to produce Figure 11b. Phase-only matrix C_P was used to calibrate the snapshots.

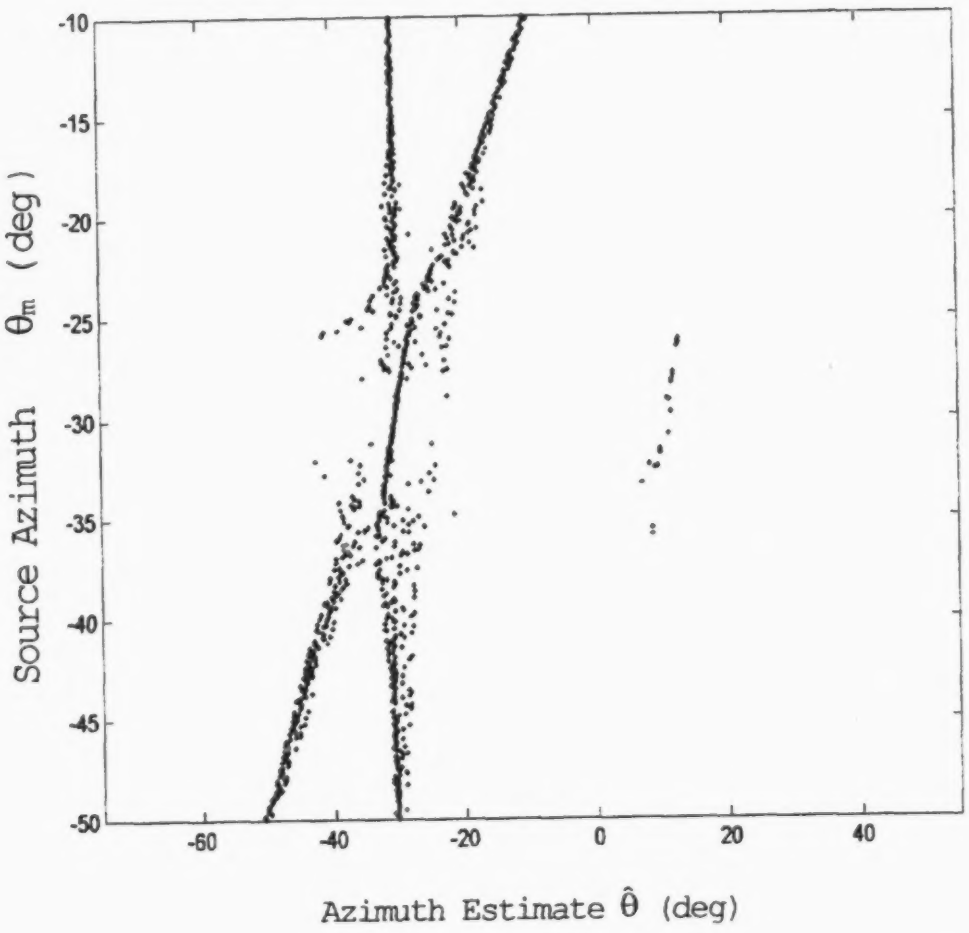

Figure 13c: Candidate direction estimates calculated with the synthetic snapshots used to produce Figure 11c. Gain-and-phase matrix C_{GP} was used to calibrate the snapshots.

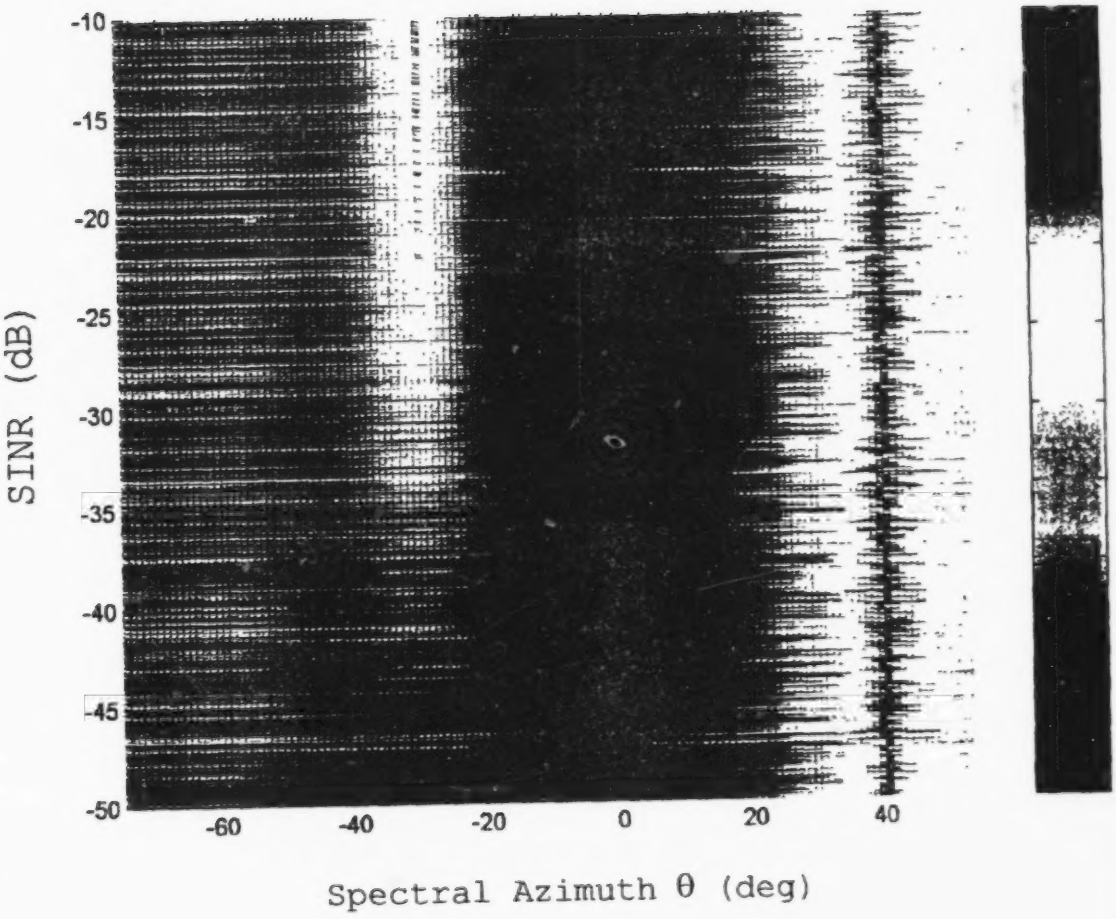

Figure 14a: Directional spectra of a target in strong interference. Matrix C was used to calibrate the snapshots.

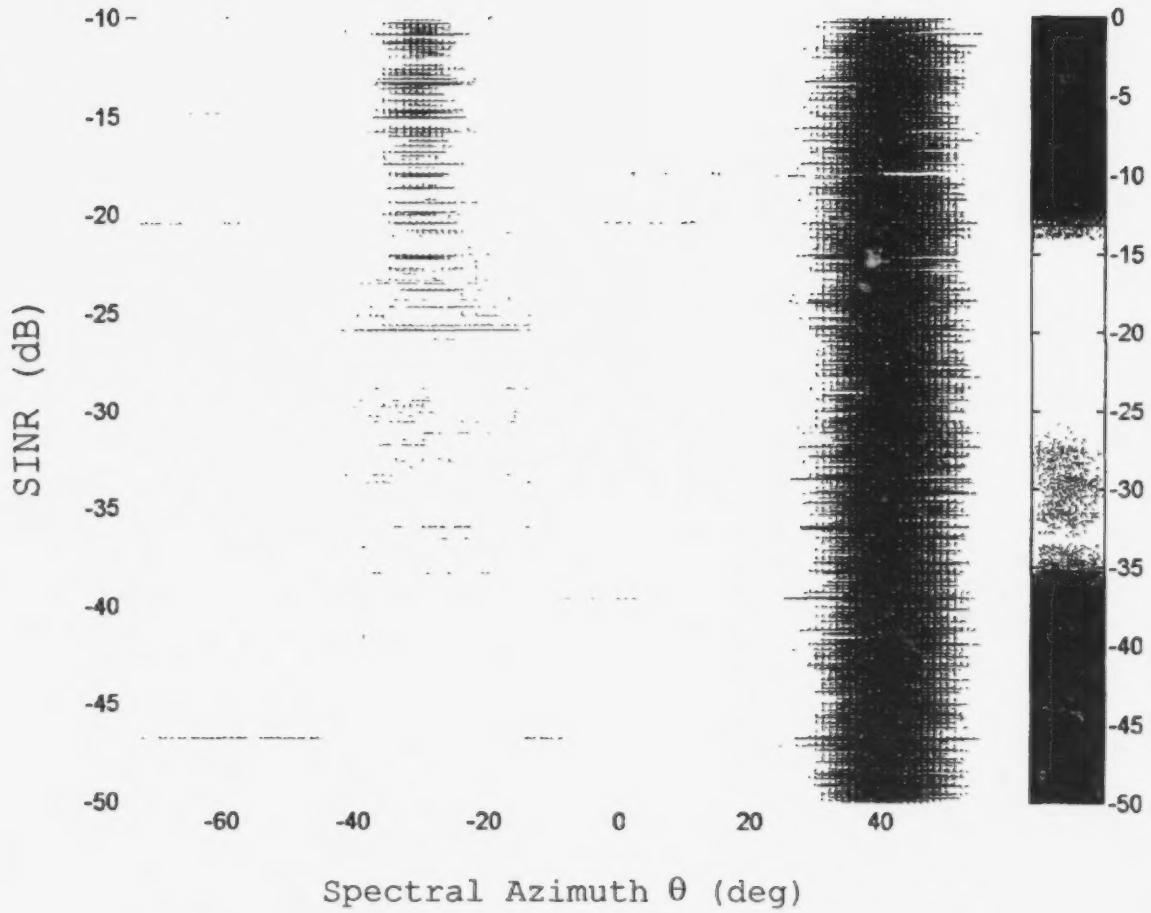

Figure 14b: Directional spectra of a target in strong interference. Phase-only matrix C_P was used to calibrate the snapshots.

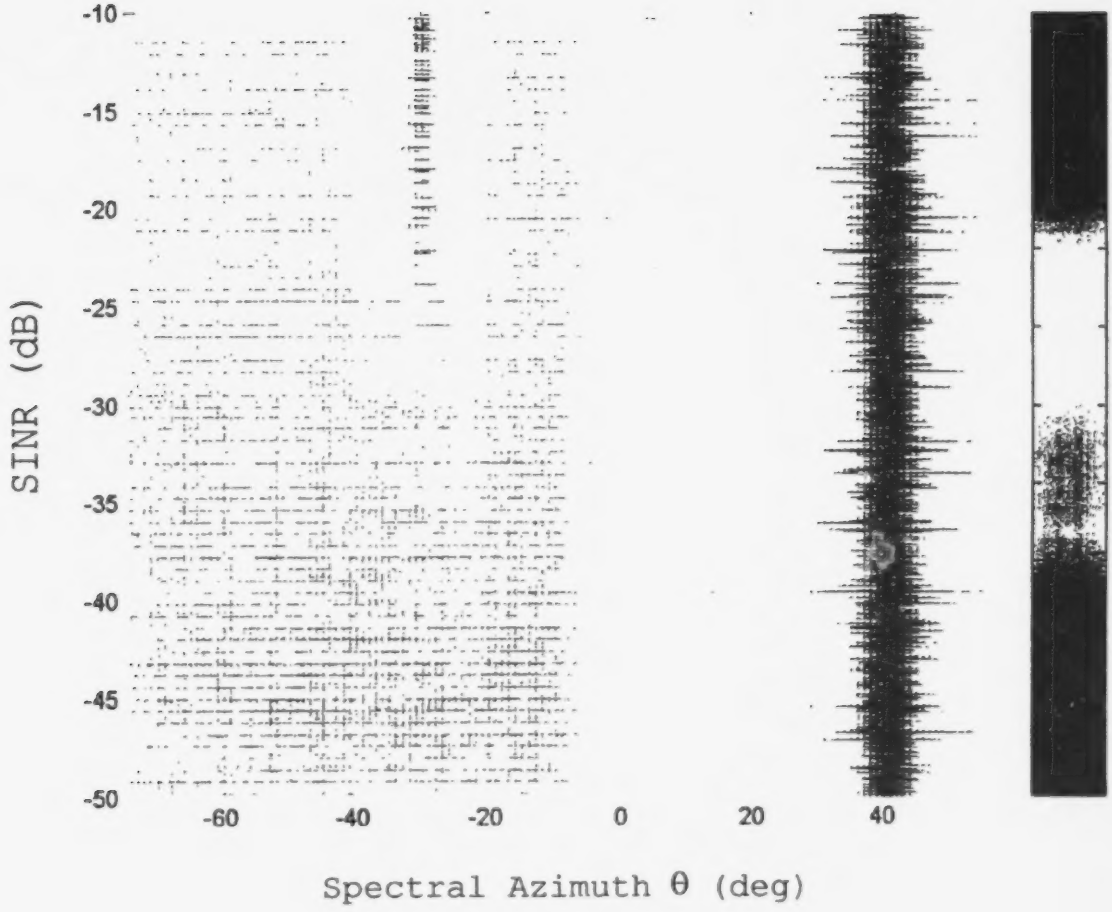

Figure 14c: Directional spectra of a target in strong interference. Gain-and-phase matrix C_{GP} was used to calibrate the snapshots.

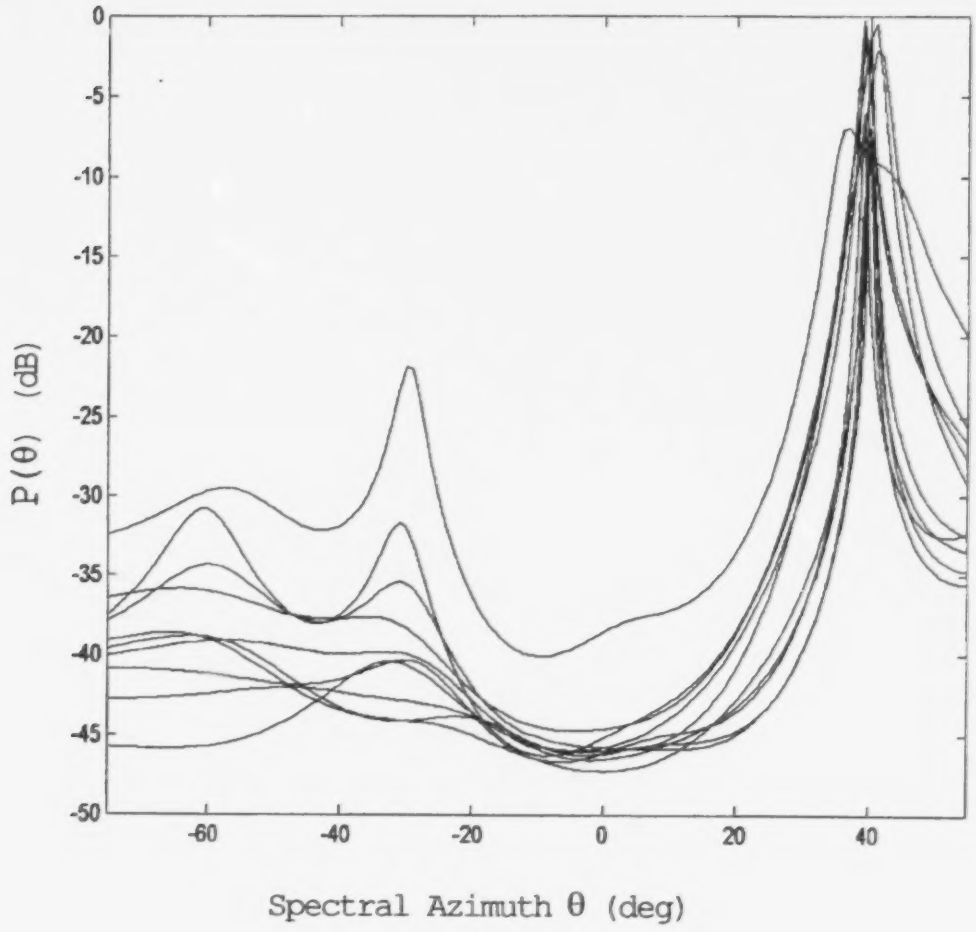

Figure 15a: Some directional spectra of synthetic snapshots with SINR=-40 dB. Matrix **C** was used to calibrate the snapshots.

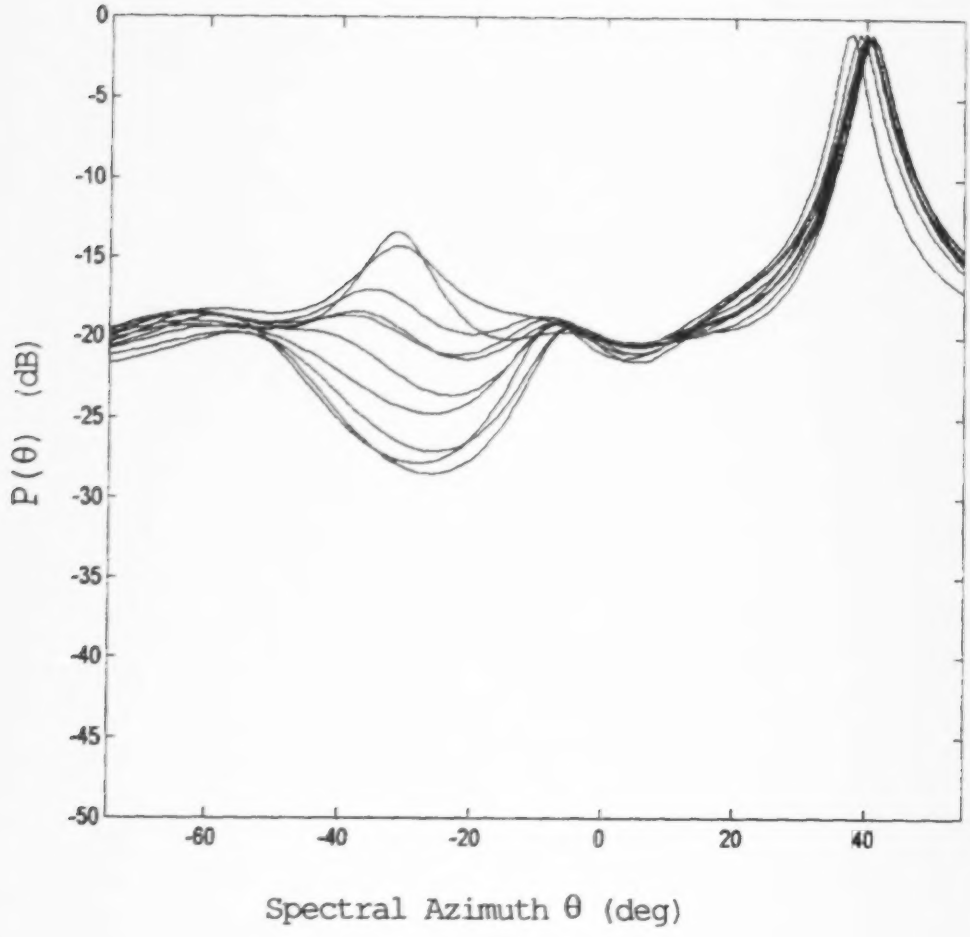

Figure 15b: Some directional spectra of synthetic snapshots with SINR=-23 dB. Phase-only matrix C_P was used to calibrate the snapshots.

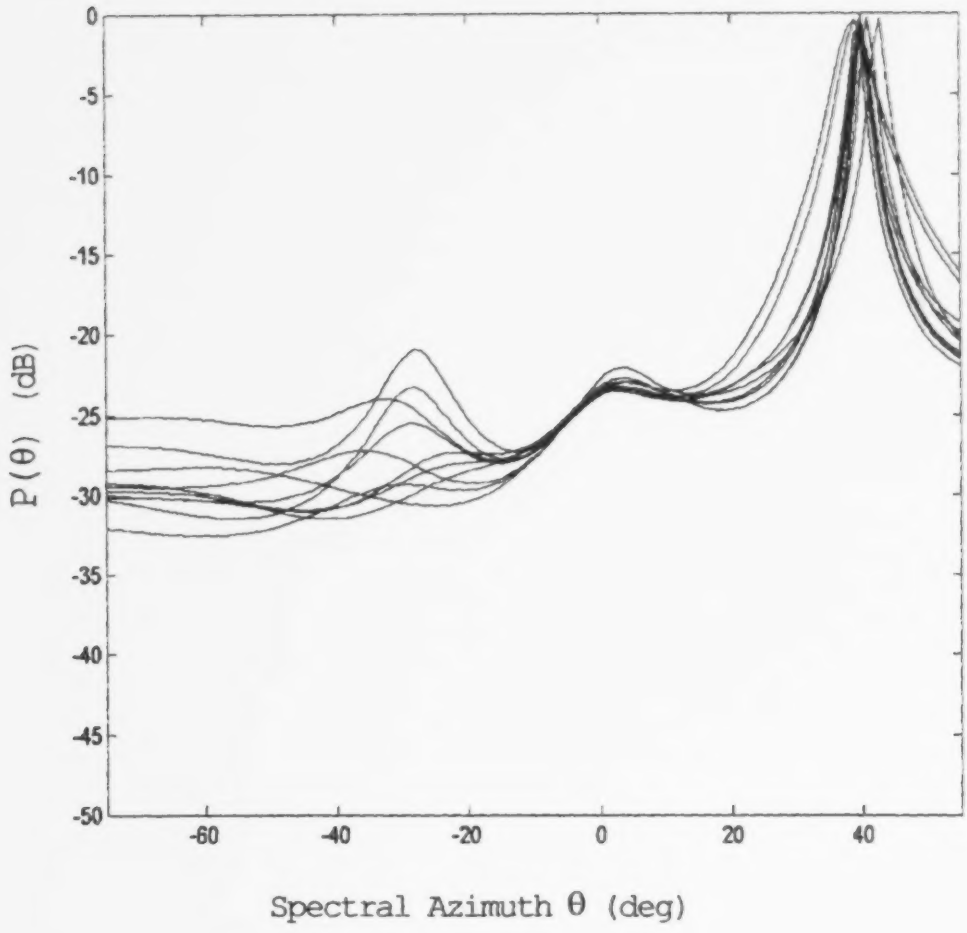

Figure 15c: Some directional spectra of synthetic snapshots with SINR=-30 dB. Gain-and-phase matrix C_{GP} was used to calibrate the snapshots.

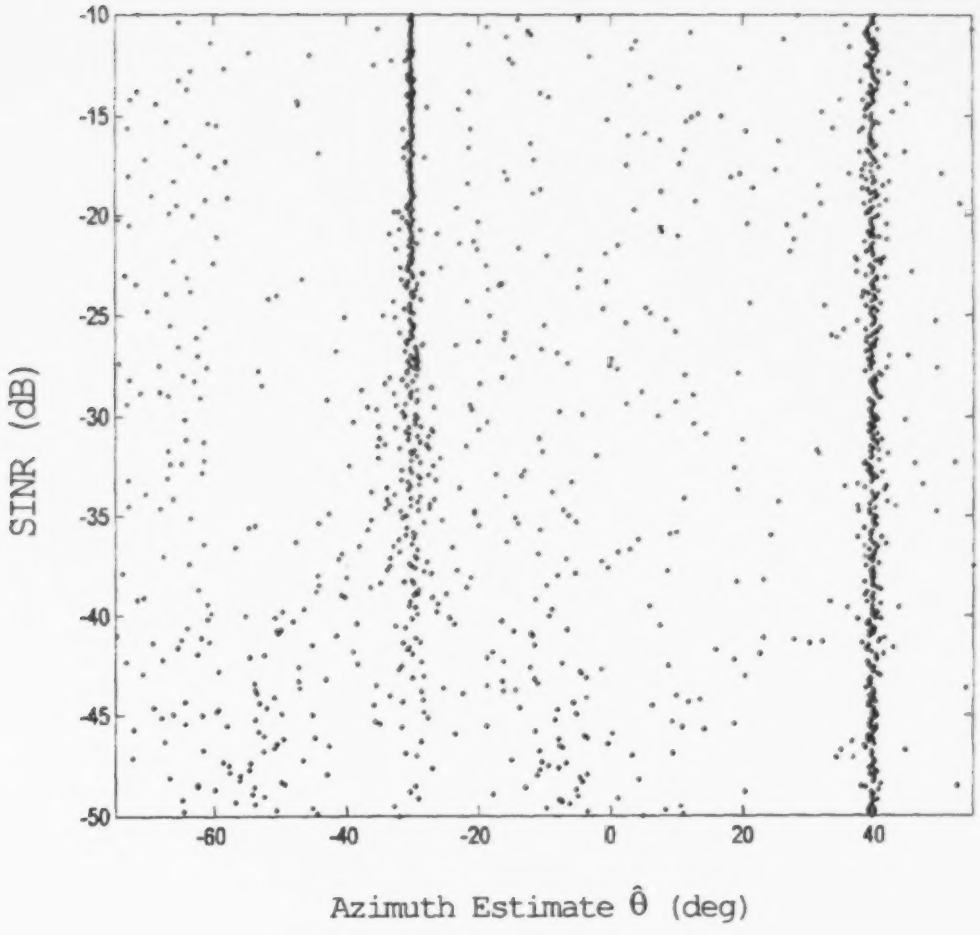

Figure 16a. Candidate direction estimates calculated with the synthetic snapshots used to produce Figure 14a. Matrix C was used to calibrate the snapshots.

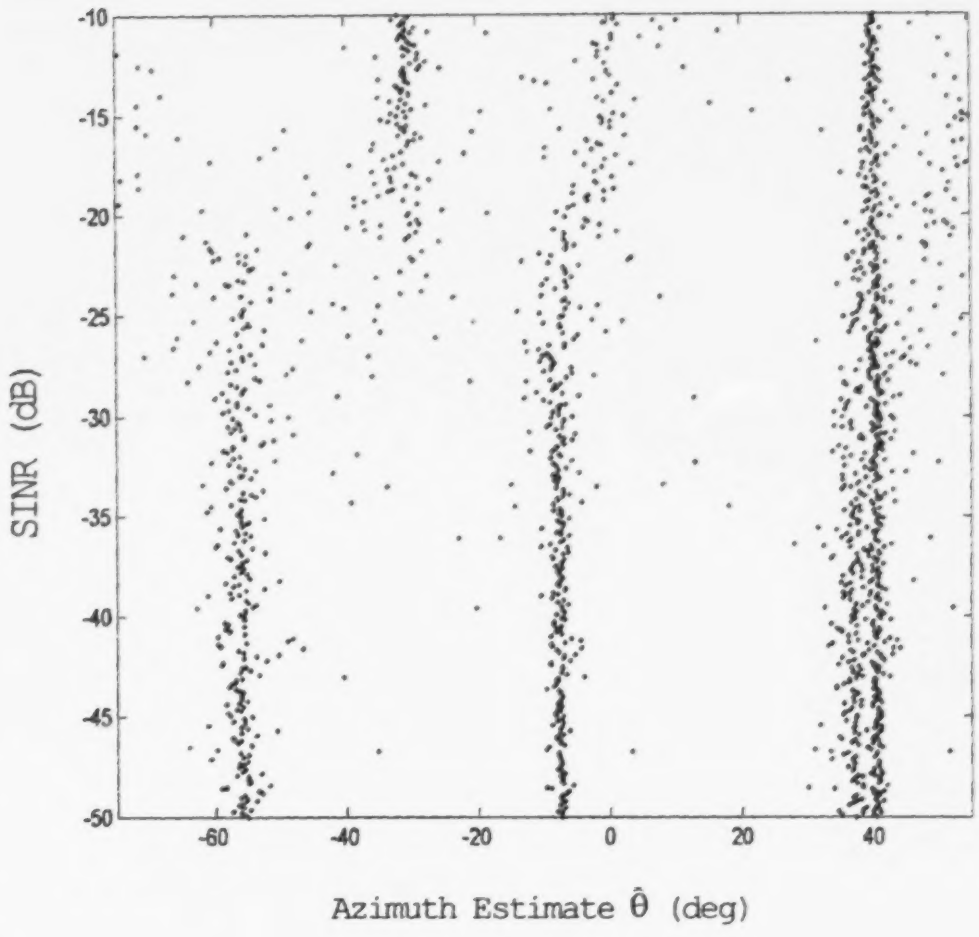

Figure 16b. Candidate direction estimates calculated with the synthetic snapshots used to produce Figure 14b. Phase-only matrix C_P was used to calibrate the snapshots.

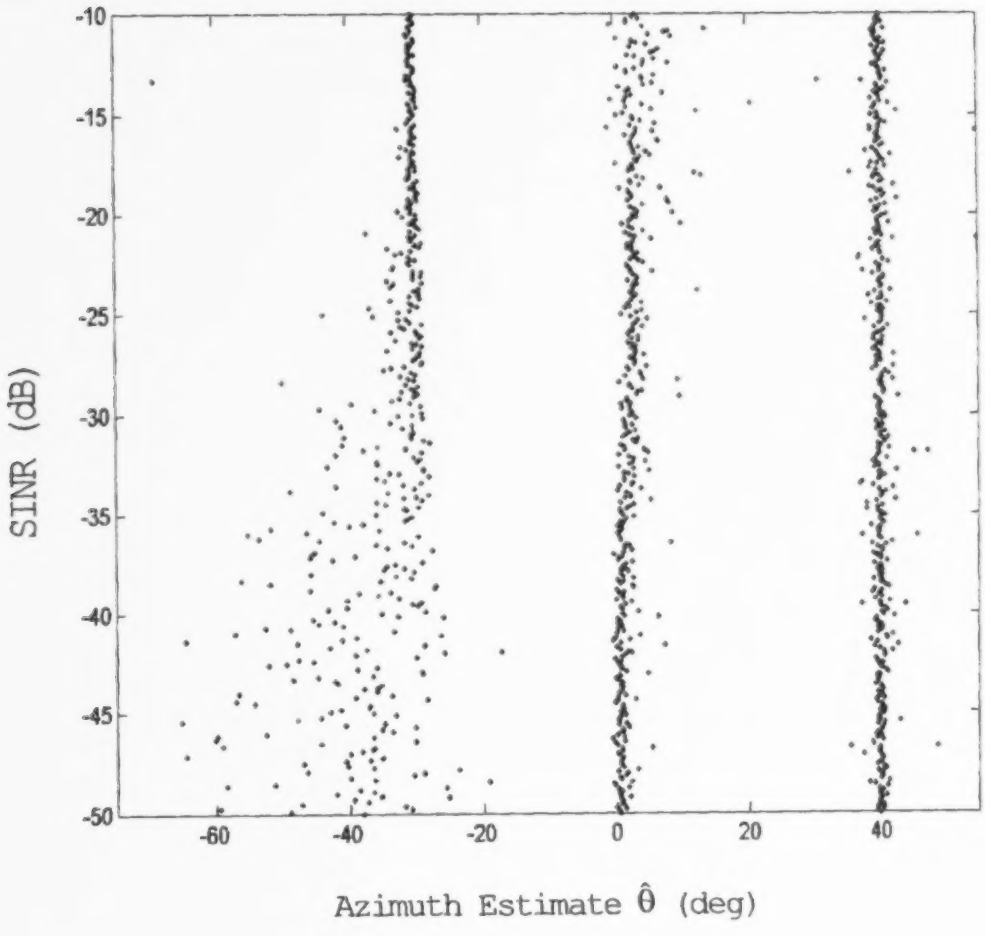

Figure 16c: Candidate direction estimates calculated with the synthetic snapshots used to produce Figure 14c. Gain-and-phase matrix $\mathbf{C}_{GP}$ was used to calibrate the snapshots

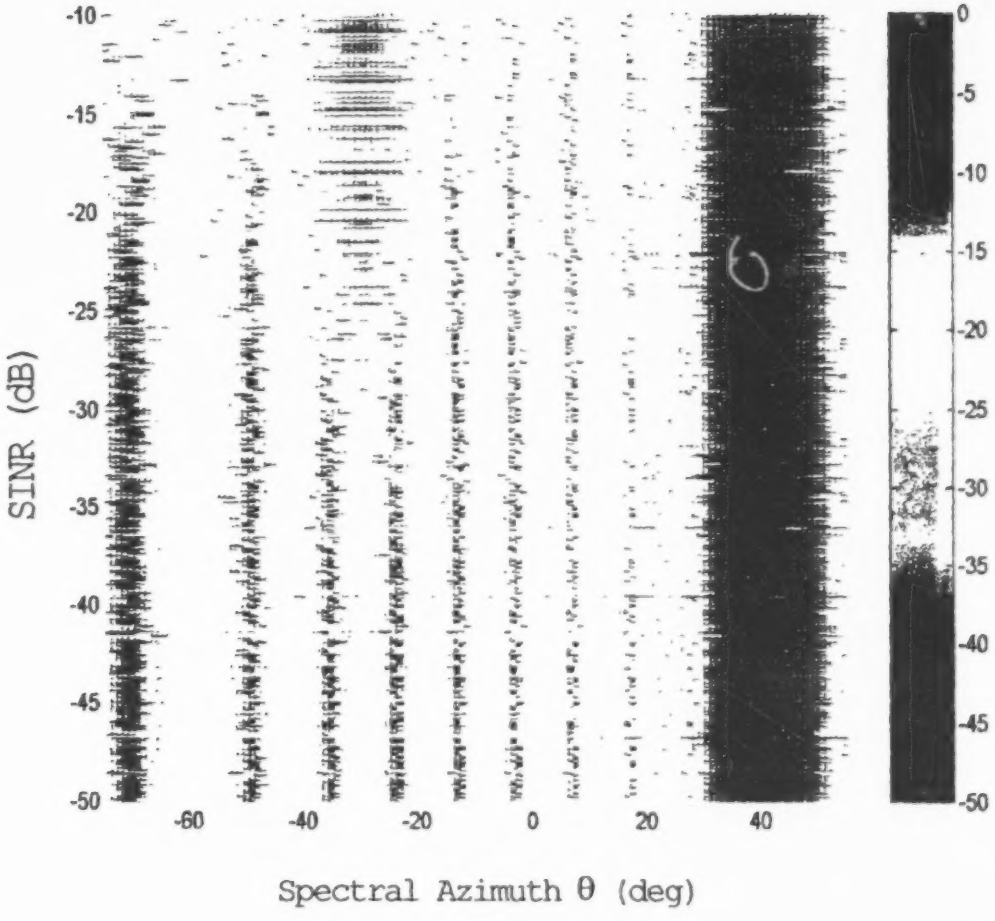

Figure 17a: DFT directional spectra of array snapshots used to calculate the Capon spectra in Figure 14a. The snapshots have a target in strong interference. Matrix **C** was used to calibrate the snapshots

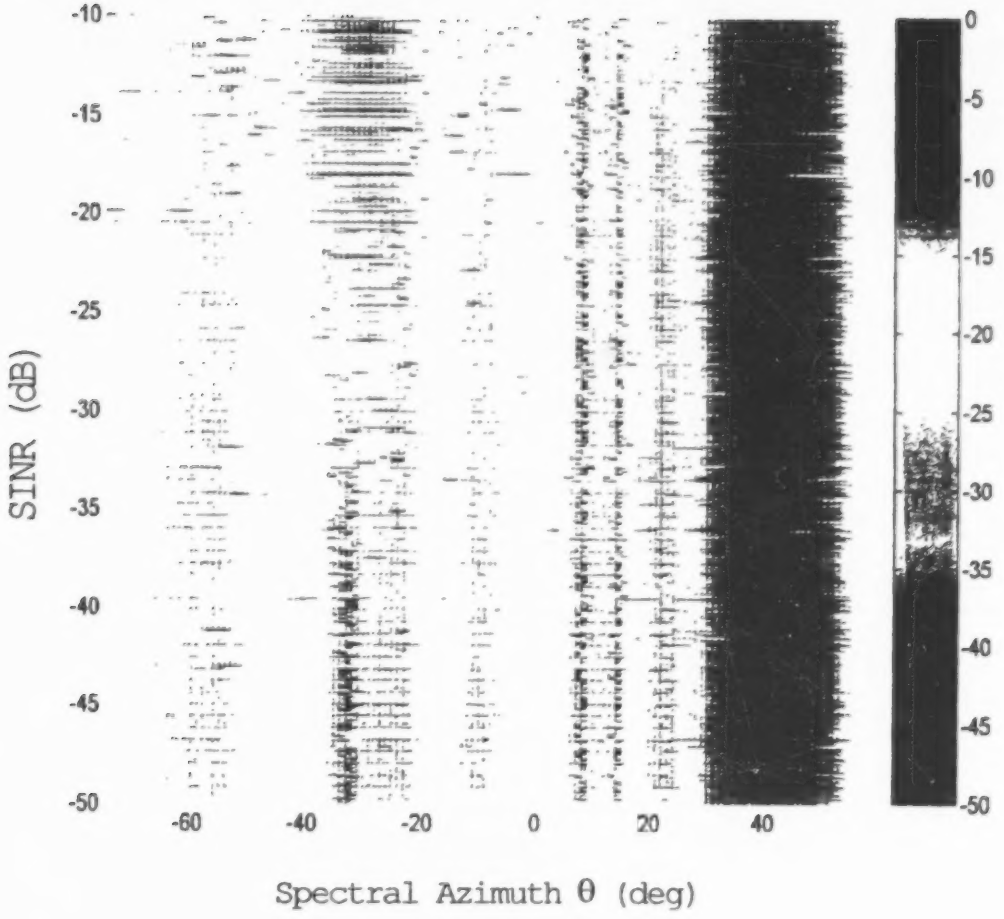

Figure 17b. DFT directional spectra of array snapshots used to calculate the Capon spectra in Figure 14b. The snapshots have a target in strong interference. Phase-only matrix C_P was used to calibrate the snapshots

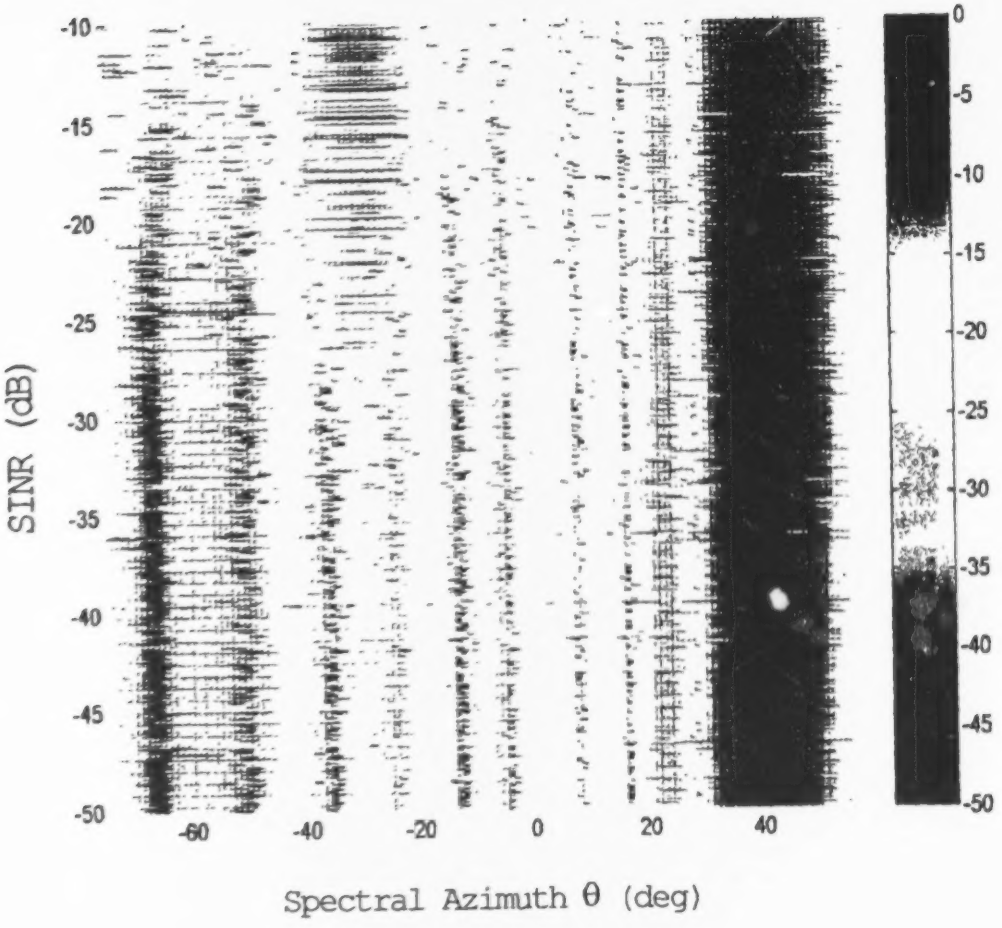

Figure 17c: DFT directional spectra of array snapshots used to calculate the Capon spectra in Figure 14c. The snapshots have a target in strong interference. Gain-and-phase matrix C_{GP} was used to calibrate the snapshots.

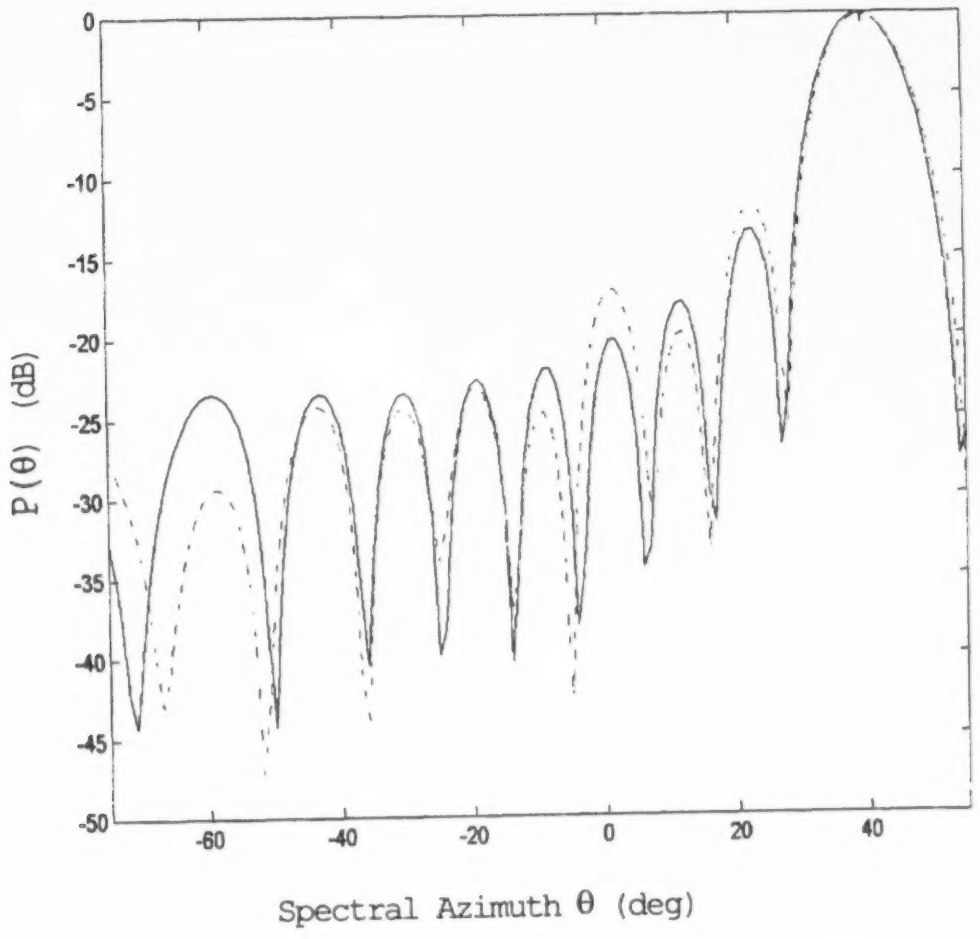

Figure 18: DFT directional spectra calculated with a SINR=-50 dB snapshot and calibration matnces C (black), C_P (red) and C_{GP} (blue).

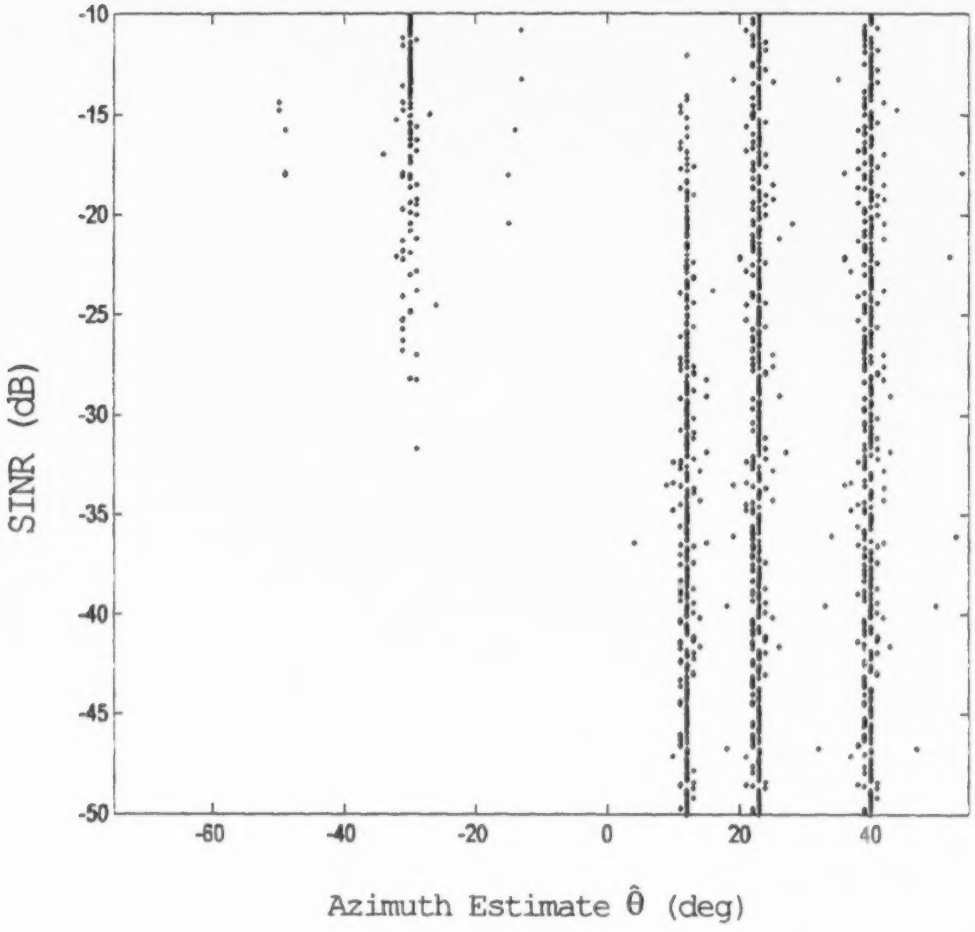

Figure 19a: DFT candidate direction estimates calculated with matnx C and the synthetic snapshots.

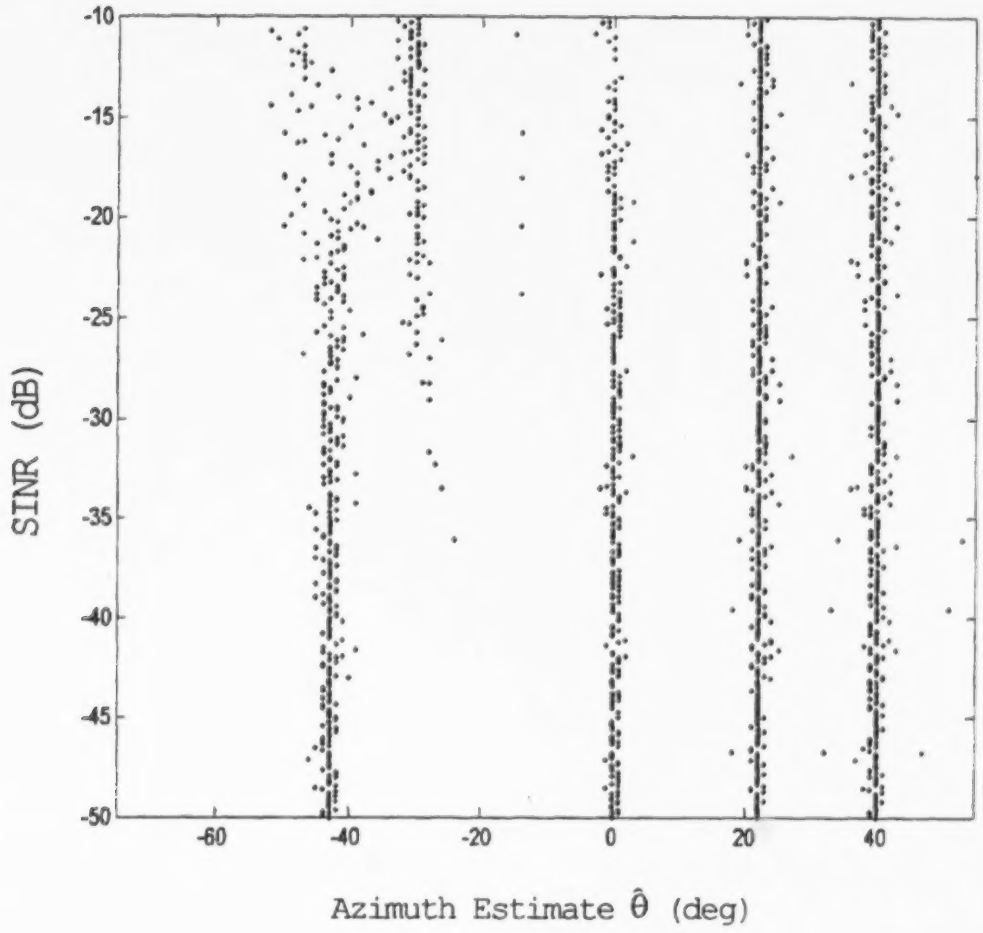

Figure 19b: DFT candidate direction estimates calculated with phase-only matrix C_P and the synthetic snapshots.

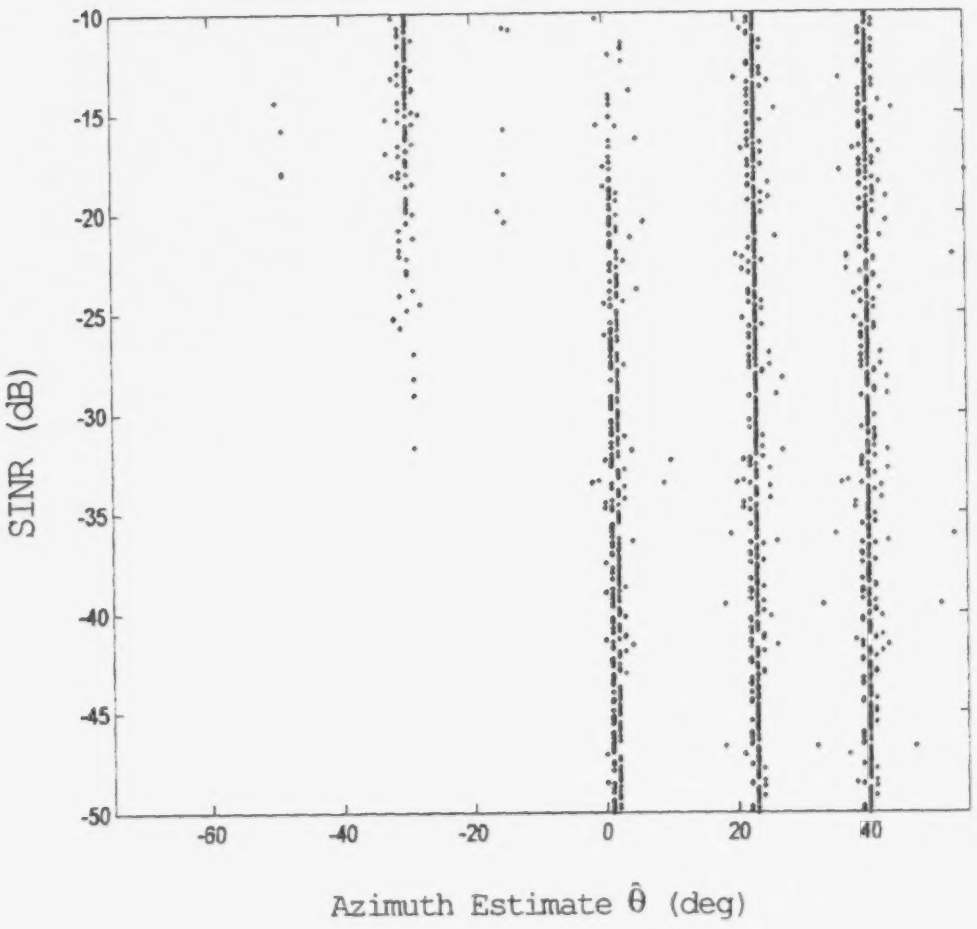

Figure 19c: DFT candidate direction estimates calculated with gain-and-phase matrix C_{GP} and the synthetic snapshots.

5. Conclusion

A description and a performance evaluation of the matrix calibration method developed for the receive antenna array of the HFSWR at Cape Race, Newfoundland, have been presented. The performance evaluation compared the matrix method with two other methods: (a) the single-set phase-only calibration method being used and (b) an assumed single-set gain-and-phase method that equalizes the complex element output amplitudes of signals in the boresight direction. Some notable observations on targets within 55° of the boresight direction are listed below.

(a) The leakage of signal power outside the source direction were 0.04% and 1.29% in data sections with high and low signal-to-interference-plus-noise ratios (SINRs), respectively, in calculations with the matrix calibration method. They were between 5.20 and 11.7% in the single-set phase-only method, and between 0.21 and 5.73% in the single-set gain-and-phase method.

(b) The errors in source direction estimates were usually the smallest in the matrix method and the largest in the phase-only method.

(c) The errors in source direction estimates had a component linearly dependent on the source azimuth in the phase-only and gain-and-phase methods.

(d) The signal peaks in the directional spectra of the array snapshots were the narrowest in calculations with the matrix method. They were significantly broader in the phase-only method. Those in the gain-and-phase method were just as narrow as the peaks in the matrix method for signals in the boresight direction. They increased to about half the widths of the phase-only method as the source moved towards the ±50° directions.

(e) The power levels of false peaks were less than -40 dB of the true signal in the matrix method. They were above -30 dB and frequently over -20 dB in the phase-only method. Those in the gain-and-phase method are usually between -30 and -20 dB.

(f) The false peaks did not form false target tracks in the matrix method. They frequently formed false tracks in the phase-only and gain-and phase methods.

(h) Line splitting (two direction estimates separated by less than one beamwidth in high-resolution direction-finding, one signal source actually present) was very common in calculations with the phase-only method.

(i) The SINR threshold in detecting targets outside the region of extremely strong interference was the lowest in the matrix method. It was approximately 17 dB higher in the phase-only method and 5 to 8 dB higher in the gain-and-phase method.

Based on the approximate 17 dB difference in SINR thresholds for target detection, the matrix calibration method could increase the present maximum nighttime target detection range of the HFSWR by more than 50%.

6. References

1. J. Capon, "High-resolution frequency-wavenumber spectrum analysis," Proceedings of the IEEE, vol 57, pp. 1408-1418, August 1969.

2. R.T. Lacoss, "Data adaptive spectral analysis methods", Geophysics, vol. 36, pp. 661-675, August 1971.

3. R.T. Lacoss, "Autoregressive and maximum likelihood spectral analysis methods", Proceedings of the 1976 NATO Conference on Signal Processing.

4. A.H. Nuttal, "Spectral analysis of a univariate process with bad data points, via maximum entropy and linear predictive techniques," Naval Underwater Systems Centre, Technical Report TR-5303, New London, CT, March 1976.

5. T.J. Ulrych and R.W. Clayton, "Time series modelling and maximum entropy," Phys. Earth Planetary Interior, vol. 12, pp. 188-200, August 1976

6. C.A. Baird, "Recursive processing for adaptive arrays," Proceedings of the Adaptive Antenna Systems Workshop, Naval Research Laboratory, March 1974.

7. I.S. Reed, J.D. Mullett, and L.E. Brennan, "Rapid convergence rage in adaptive arrays," IEEE Transactions on Aerospace and Electronic Systems, AES-10, no. 6, pp. 853-863, November 1974.

8. S.P. Applebaum, "Adaptive arrays," IEEE Transactions on Antennas and Propagation, AP-24, no.5, pp. 585-598, September 1976.

9. R.T. Compton, Jr., "The effect of random steering vector errors in the Applebaum adaptive array," IEEE Transactions on Aerospace and Electronic systems, AES-18, no. 5, pp. 392-400, September 1982.

10. B. Friedlander, "A sensitivity analysis of the MUSIC algorithm," IEEE Transactions on Acoustics, Speech, and Signal Processing, vol. 38, pp. 1740-1751, October 1990.

11. B. Friedlander, "Sensitivity analysis of the maximum likelihood direction-finding algorithm," IEEE Transactions on Aerospace and Electronic System, vol. 26, pp. 953-968, November 1990.

12. F. Li and R.J. Vaccaro, "Sensitivity analysis of DOA estimation algorithms to sensor errors," IEEE Transactions on Aerospace and Electronic systems, vol. 28, pp. 708-717, July 1992.

13. A. Swindlehurst and T. Kailath, "A performance analysis of subspace-based methods in the presence of model errors - Part I: The MUSIC algorithm," IEEE Transactions on Signal Processing, vol. 40, pp. 1758-1774, July 1992.

14. A. Swindlehurst and T. Kailath, "A performance analysis of subspace-based methods in the presence of model errors - Part II: Multidimensional algorithms," IEEE Transactions on Signal Processing, vol. 41, pp. 1277-1308, September 1993.

15. Xinping Huang and Eric K.L. Hung, "Analysis of the calibration data measured with a high-frequency antenna array", DREO Report No. 1289, August 1996.

16. Eric K.L. Hung and Zhijiang Hu, "Analysis of the HF data measured at Leitrim, using a matrix calibration method developed at DREO", DREO Report No. 1319, November 1997.

17. Eric K.L. Hung, Barry J. Dawe and Desmond Power, "Calibration of the receive antenna array in a prototype high frequency surface wave radar". RADAR'99 (International Conference on Radar Systems), Brest, France, May 17-19, 1999.

18. Eric K.L. Hung, "(Evaluation of a) matrix-construction calibration method for receive antenna arrays," IEEE Transactions on Aerospace and Electronic Systems, vol. 36, no. 3, pp. 819-828, July 2000.

Appendix A. Calculation of signal powers and direction estimates

The least squares autoregressive method [4,5] was combined with a root-finding method to calculate signal direction estimates with an array snapshot. The signal power associated with each direction estimate was then obtained with a least squares fit to the snapshot. In the procedure below, **y** is the array snapshot, $\{y_1,y_2,...,y_N\}$ are the components of **y**, N is the number of array elements, K is the order of linear prediction filter in the autoregressive method and is the largest integer not exceeding N/3, $\{g_1,g_2,...,g_K\}$ are the filter coefficients, $\{z_1,z_2,...,z_K\}$ are the poles of the autoregressive filter, $\{\theta_1,\theta_2,...,\theta_K\}$ are signal direction estimates calculated with the poles, $\{\alpha_1,\alpha_2,...,\alpha_K\}$ are complex signal amplitude estimates, and $\{p_1,p_2,...,p_K\}$ are signal power estimates. There are six steps in the procedure. In Step 1, the parameter values are N=16 and K=5. In Step 4, α is a vector with K components and is the least square solution of the equation

$$\mathbf{y} = \mathbf{A}\alpha + \varepsilon\,, \tag{A.1}$$

where ε is an error vector. In Step 5, directions with $|\sin\theta_k|>1.0$ are non-physical and are ignored.

Step 1.

Solve the following equation for the coefficients $\{g_1,g_2,...,g_K\}$,

$$\begin{bmatrix} y_K & y_{K-1} & \cdots & y_1 \\ y_{K+1} & y_K & \cdots & y_2 \\ & & \cdots & \\ & & \cdots & \\ y_{N-1} & y_{N-2} & \cdots & y_{N-K} \\ \hline y^*_2 & y^*_3 & \cdots & y^*_{K+1} \\ & & \cdots & \\ & & \cdots & \\ y^*_{N-K+1} & y^*_{N-K+2} & \cdots & y^*_N \end{bmatrix} \begin{bmatrix} g_1 \\ g_2 \\ \cdot \\ \cdot \\ \cdot \\ \cdot \\ g_K \end{bmatrix} = \begin{bmatrix} y_{K+1} \\ y_{K+2} \\ \cdot \\ \cdot \\ y_N \\ \cdot \\ y^*_1 \\ \cdot \\ \cdot \\ y^*_{N-K} \end{bmatrix} \tag{A.2}$$

Step 2.

Find the roots of the polynomial

$$F(z) = z^K - g_1 z^{K-1} - g_2 z^{K-2} - ... - g_K\,. \tag{A.3}$$

Denote them by $\{z_1,z_2,...,z_K\}$.

Step 3.

Construct a matrix of array steering vectors as

$$\mathbf{A} = (\mathbf{a}_1, \mathbf{a}_2, \ldots, \mathbf{a}_K) , \tag{A.4}$$

where $\mathbf{a}_k$ is an array steering vector given by

$$\mathbf{a}_k = (1, \tilde{z}_k^1, \tilde{z}_k^2, \ldots, \tilde{z}_k^{K-1})^T , \tag{A.5}$$

and $\tilde{z}_k = z_k / |z_k|$.

Step 4.

Calculate α, where $\alpha = (\alpha_1, \alpha_2, \ldots, \alpha_K)^T$, as

$$\alpha = \mathbf{A}^{\#}\mathbf{y} . \tag{A.6}$$

Here, $\mathbf{A}^{\#}$ is the Moore-Penrose pseudo-inverse of **A**. Use the singular value decomposition method to calculate $\mathbf{A}^{\#}$. Equate a singular value to zero if it is less then δ times the largest singular value.

Step 5.

For each k, calculate $\sin\theta_k$ with z_k and the relation

$$2\pi d \sin\theta_k = \mathrm{ang}(z_k) , \tag{A.7}$$

where d is the element spacing in wavelengths and $\mathrm{ang}(z_k)$ is the phase of z_k.

If $|\sin\theta_k| \leq 1.0$,
Calculate signal direction estimate θ_k with Eq. (A.7), and
Calculate the corresponding signal power estimate with the relation

$$p_k = |\alpha_k|^2 . \tag{A.8}$$

Step 6.

Arrange the direction estimates in the order of decreasing signal power estimates.

The value δ=0.0001 was used in this report. This value appeared to provide a good discrimination between signal and noise subspaces.

Appendix B. Calculation of Capon directional spectra

The Capon minimum variance method [1-3] is combined with a subarray method for uniform linear arrays to calculate the directional spectrum of an array snapshot. Two examples are then given to clarify the procedure and the definition

$$P(\theta) = \frac{\text{Power arriving at array elements from spectral direction } \theta}{\text{Total power at array elements}} . \qquad \text{(B.1)}$$

In the procedure below, $\mathbf{y}$ is the array snapshot, $\{y_1,y_2,...,y_N\}$ are the components of $\mathbf{y}$, N is the number of elements in the full array, J is the number of elements in the subarrays, K is the number of subarrays, $\{\mathbf{z}_1,\mathbf{z}_2,...,\mathbf{z}_K\}$ are the subarray snapshots, $\{\tilde{\mathbf{z}}_1,\tilde{\mathbf{z}}_2,...,\tilde{\mathbf{z}}_K\}$ are reversed-conjugated subarray snapshots, ε is a noise parameter, σ^2 is injected isotropic noise power at the array elements, $\mathbf{I}_J$ is a J×J identity matrix, $\mathbf{a}$ is the full array steering vector, $\{a_1,a_2,...,a_N\}$ are the components of $\mathbf{a}$, and $\mathbf{b}$ is the subarray steering vector constructed with the first J components of $\mathbf{a}$, i.e.,

$$\mathbf{b} = (a_1,a_2,...,a_J)^T . \qquad \text{(B.2)}$$

The parameter values are N=16, J=8, K=N+1-J=9, ε=0.00001.

Step 1.

Construct K subarray snapshots as

$$\mathbf{z}_k = (y_k,y_{k+1},...,y_{k-1+J})^T , \qquad k=1,2,...,K . \qquad \text{(B.3)}$$

Step 2.

Construct the reversed-conjugated snapshots as

$$\tilde{\mathbf{z}}_k = (y^*_{k-1+J},...,y^*_{k+1},y^*_k)^T , \qquad k=1,2,...,K . \qquad \text{(B.4)}$$

Step 3.

Construct a covariance matrix $\mathbf{R}$ as

$$\mathbf{R} = (2K)^{-1} \sum_{k=1}^{2K} (\mathbf{z}_k\mathbf{z}_k^H + \tilde{\mathbf{z}}_k\tilde{\mathbf{z}}_k^H) . \qquad \text{(B.5)}$$

Step 4.

Calculate σ^2 as

$$\sigma^2 = \varepsilon \mathrm{Tr}(\mathbf{R}) , \qquad \text{(B.6)}$$

where Tr(**R**) denotes the trace of **R**.

Step 5.

Construct an augmented covariance matrix $\mathbf{R}_A$ as

$$\mathbf{R}_A = \mathbf{R} + \sigma^2\mathbf{I}_J , \tag{B.7}$$

Step 6.

Specify azimuth direction θ.

Construct the array steering vector **a** for the full array with Eq. (16).

Construct the subarray steering vector **b** with (B.2).

Step 7.

Calculate the signal power from direction θ as

$$P(\theta) = \frac{1}{\mathbf{b}^H\mathbf{R}_A^{-1}\mathbf{b}} \times \frac{1}{J^{-1}\mathrm{Tr}(\mathbf{R}_A)} . \tag{B.8}$$

The product $J^{-1}\mathrm{Tr}(\mathbf{R}_A)$ is the total power at the array elements after the addition of the isotropic noise term $\sigma^2\mathbf{I}_J$ to **R**.

Example 1. One signal, no noise, no interference

The signal has direction θ_1, amplitude α_1, array steering vector $\mathbf{a}_1$, and subarray steering vector $\mathbf{b}_1$. The snapshot of the full array is given by

$$\mathbf{y} = \alpha_1\mathbf{a}_1 , \tag{B.9}$$

and subarray snapshot $\mathbf{z}_1$, for example, is given by

$$\mathbf{z}_1 = \alpha_1\mathbf{b}_1 . \tag{B.10}$$

One can now verify that

$$\mathbf{R} = |\alpha_1|^2\mathbf{b}_1\mathbf{b}_1^H , \tag{B.11}$$

$$\sigma^2 = \varepsilon J|\alpha_1|^2 , \tag{B.12}$$

$$\mathbf{R}_A = |\alpha_1|^2(\mathbf{b}_1\mathbf{b}_1^H + \varepsilon J\mathbf{I}_3) , \tag{B.13}$$

$$\mathrm{Tr}(\mathbf{R}_A) = J|\alpha_1|^2(1 + \varepsilon J) . \tag{B.14}$$

Using the matrix inversion lemma and noting that $\mathbf{b}_1^H\mathbf{b}_1=J$,

$$\mathbf{R}_A^{-1} = \frac{(1+\varepsilon)J^{-1}\mathbf{I}_J - J^{-2}\mathbf{b}_1\mathbf{b}_1^H}{\varepsilon(1+\varepsilon)|\alpha_1|^2} , \tag{B.15}$$

and

$$P(\theta_1) = \frac{\varepsilon(1+\varepsilon)|\alpha_1|^2}{(1+\varepsilon)-J^{-2}|\mathbf{b}_1^H\mathbf{b}_1|^2} \times \frac{1}{(1+\varepsilon J)|\alpha_1|^2} . \tag{B.16}$$

In the signal direction, where $\theta=\theta_1$ and $\mathbf{b}=\mathbf{b}_1$, this equation gives

$$P(\theta_1) = \frac{|\alpha_1|^2+\varepsilon|\alpha_1|^2}{|\alpha_1|^2+\varepsilon J|\alpha_1|^2} . \tag{B.17}$$

The numerator on the right hand side is the sum of the signal power and the isotropic noise power from the signal direction. The denominator is the sum of signal power and the sum of isotropic noise power over all directions.

In directions such that $\mathbf{b}_1^H\mathbf{b}_1=0$, the signal is absent and Eq. (B.16) gives

$$P(\theta) = \frac{\varepsilon|\alpha_1|^2}{|\alpha_1|^2+\varepsilon J|\alpha_1|^2} . \tag{B.18}$$

Here, the numerator is the noise power from direction θ. In the limit $\varepsilon=0$, the right hand sides of Eqs. (B.17) and (B.18) become 1.0 and 0.0, respectively.

Example 2. Multiple signal sources

There are J signal sources with directions $\{\theta_1,\theta_2,...,\theta_J\}$, amplitudes $\{\alpha_1,\alpha_2,...,\alpha_J\}$, array steering vectors $\{\mathbf{a}_1,\mathbf{a}_2,...,\mathbf{a}_J\}$, and subarray steering vectors $\{\mathbf{b}_1,\mathbf{b}_2,...,\mathbf{b}_J\}$. To simplify the discussions, two assumptions are made. First, the source directions are mutually orthogonal, so that

$$\mathbf{b}_p^H\mathbf{b}_q = J\delta_{pq} , \tag{B.19}$$

where δ_{pq} is the Kronecker delta function, i.e., $\delta_{pq}=1$ if $p=q$ and $\delta_{pq}=0$ if $p\neq q$. Second, K is so large that $\mathbf{R}$ can replaced by the expected value.

In this example,

$$\mathbf{y} = \alpha_1\mathbf{a}_1 + \alpha_2\mathbf{a}_2 + ... + \alpha_J\mathbf{a}_J , \tag{B.20}$$

and $\mathbf{z}_1$, for example, is given by

$$\mathbf{z}_1 = \alpha_1\mathbf{b}_1 + \alpha_2\mathbf{b}_2 + ... + \alpha_J\mathbf{b}_J \,. \tag{B.21}$$

Equating $\mathbf{R}$ to the expected value gives

$$\mathbf{R} = |\alpha_1|^2\mathbf{b}_1\mathbf{b}_1^H + |\alpha_2|^2\mathbf{b}_2\mathbf{b}_2^H + ... + |\alpha_J|^2\mathbf{b}_J\mathbf{b}_J^H \,, \tag{B.22}$$

$$\sigma^2\mathbf{I}_J = \varepsilon J P_S \mathbf{I}_J$$

$$= \varepsilon P_S(\mathbf{b}_1\mathbf{b}_1^H + \mathbf{b}_2\mathbf{b}_2^H + ... + \mathbf{b}_J\mathbf{b}_J^H) \,. \tag{B.23}$$

where

$$P_S = |\alpha_1|^2 + |\alpha_2|^2 + ... + |\alpha_J|^2 \tag{B.24}$$

is the sum of the signal powers at individual array elements. Eq. (24) uses the property that

$$(\mathbf{b}_1,\mathbf{b}_2,..,\mathbf{b}_J)^H(\mathbf{b}_1,\mathbf{b}_2,..,\mathbf{b}_J) = J\mathbf{I}_J \,. \tag{B.25}$$

This leads to

$$J\mathbf{I}_J = (\mathbf{b}_1,\mathbf{b}_2,..,\mathbf{b}_J)(\mathbf{b}_1,\mathbf{b}_2,..,\mathbf{b}_J)^H$$

$$= \mathbf{b}_1\mathbf{b}_1^H + \mathbf{b}_2\mathbf{b}_2^H + ... + \mathbf{b}_J\mathbf{b}_J^H \,. \tag{B.26}$$

Substitutions of Eq. (B.22) and (B.23) into (B.7) and using Eq. (B.19),

$$\mathbf{R}_A = (|\alpha_1|^2+\varepsilon P_S)\mathbf{b}_1\mathbf{b}_1^H + (|\alpha_2|^2+\varepsilon P_S)\mathbf{b}_2\mathbf{b}_2^H + ... + (|\alpha_J|^2+\varepsilon P_S)\mathbf{b}_J\mathbf{b}_J^H \,, \tag{B.27}$$

$$\mathbf{R}_A^{-1} = (|\alpha_1|^2+\varepsilon P_S)^{-1}J^{-2}\mathbf{b}_1\mathbf{b}_1^H + (|\alpha_2|^2+\varepsilon P_S)^{-1}J^{-2}\mathbf{b}_2\mathbf{b}_2^H + ... + (|\alpha_J|^2+\varepsilon P_S)^{-1}J^{-2}\mathbf{b}_J\mathbf{b}_J^H \,, \tag{B.28}$$

$$Tr(\mathbf{R}_A) = (1+\varepsilon J)JP_S \,, \tag{B.29}$$

and

$$P(\theta_j) = \frac{|\alpha_j|^2+\varepsilon P_S}{P_S+\varepsilon J P_S} \,. \tag{B.30}$$

The numerator on the right hand side is the power at an array element due to the signal source at direction θ_j plus the injected isotropic noise power from this direction. The denominator is the sum of signal powers from all sources plus the sum of injected noise powers over all directions. In the limit ε=0, Eq. (B.29) gives $P(\theta_j)=|\alpha_j|^2/P_S$.

UNCLASSIFIED
SECURITY CLASSIFICATION OF FORM
(highest classification of Title, Abstract, Keywords)

DOCUMENT CONTROL DATA

(Security classification of title, body of abstract and indexing annotation must be entered when the overall document is classified)

1 ORIGINATOR (the name and address of the organization preparing the document Organizations for whom the document was prepared, e g Establishment sponsoring a contractor's report, or tasking agency, are entered in section 8)

Defence Research Establishment Ottawa
Department of National Defence
Ottawa, Ontario, Canada K1A 0Z4

2 SECURITY CLASSIFICATION (overall security classification of the document, including special warning terms if applicable)

UNCLASSIFIED

3 TITLE (the complete document title as indicated on the title page Its classification should be indicated by the appropriate abbreviation (S,C or U) in parentheses after the title)

A calibration procedure for an HFSWR receive array (U)

4 AUTHORS (Last name, first name, middle initial)

Hung, Eric K.L.

5 DATE OF PUBLICATION (month and year of publication of document)

DECEMBER 2001

6a NO OF PAGES (total containing information Include Annexes, Appendices, etc)

73

6b NO OF REFS (total cited i document)

18

7 DESCRIPTIVE NOTES (the category of the document, e g technical report, technical note or memorandum If appropriate, enter the type of report, e g interim, progress, summary, annual or final Give the inclusive dates when a specific reporting period is covered)

Technical report

8 SPONSORING ACTIVITY (the name of the department project office or laboratory sponsoring the research and development Include the address)

Defence Research Establishment Ottawa
Department of National Defence
Ottawa, Ontario, Canada K1A 0K2

9a PROJECT OR GRANT NO (if appropriate, the applicable research and development project or grant number under which the document was written Please specify whether project or grant)

05AB11

9b CONTRACT NO (if appropriate, the applicable number under which the document was written)

10a ORIGINATOR'S DOCUMENT NUMBER (the official document number by which the document is identified by the originating activity This number must be unique to this document)

DREO TR 2001-103

10b OTHER DOCUMENT NOS (Any other numbers which may be assigned this document either by the originator or by the sponsor)

11 DOCUMENT AVAILABILITY (any limitations on further dissemination of the document, other than those imposed by security classification)

(X) Unlimited distribution
( ) Distribution limited to defence departments and defence contractors, further distribution only as approved
( ) Distribution limited to defence departments and Canadian defence contractors, further distribution only as approved
( ) Distribution limited to government departments and agencies, further distribution only as approved
( ) Distribution limited to defence departments, further distribution only as approved
( ) Other (please specify)

12 DOCUMENT ANNOUNCEMENT (any limitation to the bibliographic announcement of this document This will normally correspond to the Document Availability (11) However, where further distribution (beyond the audience specified in 11) is possible, a wider announcement audience may be selected)

13 ABSTRACT (a brief and factual summary of the document It may also appear elsewhere in the body of the document itself It is highly desirable that the abstract of classified documents be unclassified Each paragraph of the abstract shall begin with an indication of the security classification of the information in the paragraph (unless the document itself is unclassified) represented as (S), (C), or (U) It is not necessary to include here abstracts in both official languages unless the text is bilingual)

This report contains a description and performance evaluation of the matrix calibration method developed by the author in 1995 for the receive antenna array in the high frequency surface wave radar (HFSWR) at Cape Race, Newfoundland. The evaluation compares this method with two other methods: (a) the phase-only calibration method being used and (b) an assumed gain-and-phase method that equalizes the complex element output amplitudes of signals in the boresight direction.

The results showed that the matrix calibration method had the most accurate direction estimates, the narrowest spectral peaks, the best resolution of closely space targets, and the lowest signal-to-interference-plus-noise ratio (SINR) threshold for target detection. The phase-only and gain-and-phase methods had false target tracks and direction-dependent biases in direction estimates. The phase-only method also had a line splitting problem

Based on the difference in SINR thresholds for target detection, the matrix calibration method could increase the present maximum nighttime target detection range of the HFSWR by more than 50% in situations where the interference is highly directional and extremely strong.

14 KEYWORDS, DESCRIPTORS or IDENTIFIERS (technically meaningful terms or short phrases that characterize a document and could be helpful in cataloguing the document They should be selected so that no security classification is required Identifiers such as equipment model designation, trade name, military project code name, geographic location may also be included If possible keywords should be selected from a published thesaurus e g Thesaurus of Engineering and Scientific Terms (TEST) and that thesaurus-identified If it is not possible to select indexi terms which are Unclassified, the classification of each should be indicated as with the title.)

Calibration procedure
Receive antenna array
High frequency surface wave radar

Defence R&D Canada
is the national authority for providing
Science and Technology (S&T) leadership
in the advancement and maintenance
of Canada's defence capabilities.

R et D pour la défense Canada
est responsable, au niveau national, pour
les sciences et la technologie (S et T)
au service de l'avancement et du maintien des
capacités de défense du Canada.

#516914

CA020204

DEFENCE R&D DÉFENSE

www.drdc-rddc.dnd.ca